UNIVERSIDADE FEDERAL DE SÃO CARLOS
CENTRO DE CIÊNCIAS EXATAS E DE TECNOLOGIA
DEPARTAMENTO DE QUÍMICA
PROGRAMA DE PÓS-GRADUAÇÃO EM QUÍMICA

0D and 2D nanomaterials based on Graphene Quantum Dots and MXenes: synthesis, characterization and application in sensors and supercapacitors

Murilo Henrique Moreira Facure*

Thesis presented as a part of the requirements to obtain a Ph.D. DEGREE in SCIENCES, concentration area: PHYSICAL CHEMISTRY.

Advisor: Dr. Daniel Souza Corrêa

São Carlos, SP

2023

UNIVERSIDADE FEDERAL DE SÃO CARLOS

Centro de Ciências Exatas e de Tecnologia
Programa de Pós-Graduação em Química

Folha de Aprovação

Defesa de Tese de Doutorado do candidato Murilo Henrique Moreira Facure, realizada em 20/10/2023.

Comissão Julgadora:

Prof. Dr. Daniel Souza Correa (EMBRAPA)

Prof. Dr. Ivo Freitas Teixeira (UFSCar)

Profa. Dra. Cecilia de Carvalho Castro e Silva (Mackenzie)

Prof. Dr. Flavio Makoto Shimizu (LNNano)

Profa. Dra. Adriana Pavinatto (UB)

O Relatório de Defesa assinado pelos membros da Comissão Julgadora encontra-se arquivado junto ao Programa de Pós-Graduação em Química.

AGRADECIMENTOS

Ao Dr. Daniel S. Corrêa pela valiosa orientação, apoio, dedicação e confiança.

Ao Dr. Yury Gogotsi pela oportunidade concedida e a supervisão durante estágio de pesquisa no exterior.

Aos parceiros nos trabalhos desenvolvidos durante esse período, especialmente à Luiza A. Mercante pela parceria de sempre.

Aos membros da banca pela disposição e colaboração.

À Embrapa Instrumentação pela estrutura disponibilizada e a todo o pessoal de suporte à pesquisa pelo incansável e indispensável auxílio.

À Drexel University pelo provimento de toda estrutura e pessoal necessários para a realização do estágio de pesquisa no exterior.

Aos colegas de grupo da Embrapa e da Drexel pelas contribuições na realização destes trabalhos e pela construtiva convivência.

À FAPESP (Processos Nº 2017/10582-8 e 2021/11683-8) pela Bolsa de Doutorado e pela Bolsa Estágio de Pesquisa no Exterior concedidas e às demais agências de fomento (CNPq e CAPES) pelo suporte financeiro e pelo provimento de adequadas condições para a realização deste trabalho.

O presente trabalho foi realizado com apoio da Coordenação de Aperfeiçoamento de Pessoal de Nível Superior - Brasil (CAPES) - Código de Financiamento 001.

Ao Programa de Pós-Graduação em Química da Universidade Federal de São Carlos (PPGQ-UFSCar). Aos professores do departamento pelo conhecimento compartilhado nas disciplinas e às secretárias pelo suporte durante todo o processo.

Ao Laboratório de Caracterização Estrutural (LCE) do Departamento de Engenharia de Materiais da UFSCar e ao Laboratório Nacional de Nanotecnologia (LNNA) do Centro Nacional de Pesquisa em Energia e Materiais (CNPEM), onde foram obtidas imagens enriquecedoras para este trabalho.

Aos amigos de São Carlos, Uberaba e Filadélfia. Aos irmãos de sangue e aos de coração. Aos eternos amores pelo amor infinito. À Fernanda pelo amor, companheirismo, incentivo e dedicação incondicionais.

AUTHOR'S PUBLICATIONS

A. PATENTS

i. R.S. Andre; L.A. Mercante; **M.H.M. Facure**; L.H.C. Mattoso; D.S. Correa "Processo De Obtenção De Nanopapel Inorgânico, Nanopapel Inorgânico E Uso Do Mesmo" Patente depositada em 2020. Número de registro: BR 10 2020 006325 1 (2020)

B. BOOK CHAPTERS

i. Forms of graphene I—graphene oxide and reduced graphene oxide
M.H.M. Facure, R. Schneider, A.D. Alvarenga, L.A. Mercante, D.S. Correa
In: Recent Advances in Graphene and Graphene-Based Technologies. IOP Publishing Ltd (2023)

ii. Electrical Impedance-Based Electronic Tongues
M.H.M. Facure, M.L. Braunger, L.A. Mercante, L.G. Paterno, A. Riul Jr, D.S. Correa
In: Encyclopedia of Sensors and Biosensors (Volume 3). Elsevier (2023)

iii. Sensing Materials: Nanofibers Produced by Electrospinning and Solution Blow Spinning
R.S. Andre, **M.H.M. Facure**, R. Schneider, F.L. Migliorini, D.M. dos Santos, L.A. Mercante, D.S. Correa
In: Encyclopedia of Sensors and Biosensors (Volume 3). Elsevier (2023)

iv. Nanocompósitos Poliméricos
D.M. dos Santos, F.L. Migliorini, K.B.R. Teodoro, **M.H.M. Facure**, D.S. Correa
In: Nanotecnologia Aplicada a Polímeros. Blucher, 2022.

v. Fundamentals and applications of impedimetric electronic tongues
M.H.M. Facure, R.S. Andre, L.A. Mercante, L. Fugikawa-Santos, O.N. Oliveira Jr, D.S. Correa
In: Electronic Tongues: Fundamentals and recent advances. IOP Publishing (2021)

vi. Novel Chemical Sensors Based on Green Composite Materials for Environmental Analysis
K.B.R. Teodoro; F.L. Migliorini; **M.H.M. Facure**; R.C. Sanfelice; D. Martins; D.S. Correa
In: Nanosensors for Environment, Food and Agriculture Vol. 1. Springer (2021)

vii. Electrospun composite nanofibers as sensors for food analysis
R.S. Andre; L.A. Mercante; **M.H.M. Facure**; A. Pavinatto; D.S. Correa
In: Electrospun Polymers and Composites: Ultrafine Materials, High Performance Fibers and Wearables. Elsevier (2020)

viii. Composite nanofibers for removing water pollutants: fabrication techniques
D.S. Correa; L.A. Mercante; R. Schneider; **M.H.M. Facure**; D.A. Locilento
In: Handbook of Ecomaterials. Springer (2019)

C. SCIENTIFIC ARTICLES

i. Pillaring effect of nanodiamonds and expanded voltage window of $Ti_3C_2T_x$ supercapacitors in $AlCl_3$ electrolyte
M.H.M. Facure, K. Matthews, R. Wang, R.W. Lord, D.S. Correa, Y. Gogotsi
Energy Storage Materials 61 (2023) 102919

ii. Multifunctional and sustainable soot-modified nanofibrous membrane for adsorption, sensing and hydrogen peroxide electrogeneration
A.D Alvarenga, **M.H.M. Facure**, I. Sánchez-Montes, G.O.S. Oliveira, M.R.V. Lanza, L.A. Mercante, D.S. Correa
Journal of Cleaner Production 422 (2023) 138697

iii. Recent progress in conductive electrospun materials for flexible electronics: Energy, sensing, and electromagnetic shielding applications
L.A. Mercante, R.S. Andre, **M.H.M. Facure**, D.S. Correa, L.H.C. Mattoso
Chemical Engineering Journal 465 (2023) 142847

iv. Self-Standing Thin Films of Cellulose Nanocrystals and Graphene Quantum Dots for Detection of Trace Iron (III)
K.B.R. Teodoro, **M.H.M. Facure**, R. Schneider, A.D. Alvarenga, R.S. Andre, D.S. Correa
ACS Appl. Nano Mater. 2023, 6, 13, 11561–11571

v. Electrochemical and optical dual-mode detection of phenolic compounds using MnO_2/GQD nanozyme
M.H.M. Facure, R.S. Andre, R.M. Cardoso, L.A. Mercante, D.S. Correa
Electrochimica Acta 441 (2023) 141777

vi. Lamivudine and Zidovudine-Loaded Nanostructures: Green Chemistry Preparation for Pediatric Oral Administration
Guedes, M.D.V.; Marques, M.S.; Berlitz, S.J.; **Facure, M.H.M.**; Correa, D.S.; Steffens, C.; Contri, R.V.; Külkamp-Guerreiro, I.C.
Nanomaterials 2023, 13(4), 770

vii. Fabrication of interdigitated electrodes of graphene oxide/silica by femtosecond laser-induced forward transfer for sensing applications
K.T. Paula, S.N.C. Santos, **M.H.M. Facure**, F.L. Araujo, M.B. Andrade, D.S. Correa, C.R. Mendonça
Journal of Applied Physics 133, 053103 (2023)

viii. Colorimetric Detection of Antioxidants in Food Samples Using MnO_2/Graphene Quantum Dot Composites with Oxidase-like Activity
M.H.M. Facure, R.S. Andre, L.A. Mercante, D.S. Correa
ACS Appl. Nano Mater. 2022, 5, 10, 15211–15219

ix. Polyacrylonitrile/Reduced Graphene Oxide Free-Standing Nanofibrous Membranes for Detecting Endocrine Disruptors
M.H.M. Facure, L.A. Mercante, D.S. Correa
ACS Appl. Nano Mater. 2022, 5, 6376−6384

x.   Recent Progress in Amine Gas Sensors for Food Quality Monitoring: Novel Architectures for Sensing Materials and Systems
R.S. Andre, L.A. Mercante, **M.H. M. Facure**, R.C. Sanfelice, L. Fugikawa-Santos, T.M. Swager, D.S. Correa
ACS Sens. 2022, 7, 8, 2104–2131

xi.   Advances in 3D printed sensors for food analysis
D.M. dos Santos, R.M. Cardoso, F.L. Migliorini, **M.H.M. Facure**, L.A. Mercante, L.H.C. Mattoso, D.S. Correa
Trends in Analytical Chemistry 154 (2022) 11667

xii.   Current progress in plant pathogen detection enabled by nanomaterials-based (bio)sensors
R.M. Cardoso, T.S. Pereira, **M.H.M. Facure**, D.M. dos Santos, L.A. Mercante, L.H.C. Mattoso, D.S. Correa
Sensors and Actuators Reports 4 (2022) 10006

xiii.   Rational hydrothermal synthesis of graphene quantum dots with optimized luminescent properties for sensing applications
M.H.M. Facure, R. Schneider, L.A. Mercante, D.S. Correa
Materials Today Chemistry 23 (2022) 100755

xiv.   Nanostructured scaffolds containing graphene oxide for nanomedicine applications
T.M. Uehara, F.L. Migliorini, **M.H.M. Facure**, N.B.P. Filho, P.B. Miranda, V. Zucolotto, D.S. Correa
Polym Adv Technol. 2022; 33:591–600

xv.   Electronic nose based on hybrid free-standing nanofibrous mats for meat spoilage monitoring
R.S. Andre, **M.H.M. Facure**, L.A. Mercante, D.S. Correa
Sensors and Actuators: B. Chemical 353 (2022) 131114

xvi.   Femtosecond laser micromachining optical waveguides on transparent silica xerogels
S.N.C. Santos, K.T. Paula, F.A. Couto, **M.H.M. Facure**, D.S. Correa, C.R. Mendonca
Optical Materials 132 (2022) 11281

xvii.   Graphene Quantum Dots-Based Nanocomposites Applied in Electrochemical Sensors: A Recent Survey
M.H.M. Facure, R. Schneider, J.B.S. Lima, L.A. Mercante, D.S. Correa
Electrochem 2021, 2(3), 490-519

xviii. Design of a bioelectronic tongue for glucose monitoring using zinc oxide nanofibers and graphene derivatives
L.A. Mercante, R.S. Andre, **M.H.M. Facure**, L. Fugikawa-Santos, D.S. Correa
Sensors and Actuators Reports 3 2021, 100050

xix.   Nanocomposite-Based Chemiresistive Electronic Nose and Application in Coffee Analysis
R.S. Andre, K. Campaner, **M.H.M. Facure**, L.A. Mercante, S. Bogusz, D.S. Correa

ACS Food Sci. Technol. 2021, 1, 8, 1464–1471

xx. Tailoring the Surface Properties of Micro/Nanofibers Using 0D, 1D, 2D, and 3D Nanostructures: A Review on Post-Modification Methods
R. Schneider, **M.H.M. Facure**, P.A.M. Chagas, R.S. Andre, D.M. dos Santos, D.S. Correa
Adv. Mater. Interfaces 2021, 8, 2100430

xxi. A Review on the Role and Performance of Cellulose Nanomaterials in Sensors
K.B.R. Teodoro, R.C. Sanfelice, F.L. Migliorini, A. Pavinatto, **M.H.M. Facure**, D.S. Correa
ACS Sens. 2021, 6, 7, 2473–2496

xxii. Recent trends in nanozymes design: from materials and structures to environmental applications
C.A.S Ballesteros, L.A. Mercante, A. Alvarenga, **M.H.M. Facure**, R. Schneider, D.S. Correa
Mater. Chem. Front., 2021, 5, 7419–7451

xxiii. Two-dimensional MoS_2-based impedimetric electronic tongue for the discrimination of endocrine disrupting chemicals using machine learning
W.A. Christinelli, F.M. Shimizu, **M.H.M. Facure**, R.Cerri, O.N. Oliveira Jr, D.S. Correa, L.H.C. Mattoso
Sensors and Actuators: B. Chemical 336 (2021) 129696

xxiv. Dye Adsorption Capacity of MoS2 Nanoflakes Immobilized on Poly(lactic acid) Fibrous Membranes
R. Schneider, **M.H.M Facure**, A.D. Alvarenga, P.A.M. Chagas, D.M. dos Santos, D.S. Correa
ACS Appl. Nano Mater. 2021, 4, 5, 4881–4894

xxv. A Principal Curves-Based Method for Electronic Tongue Data Analysis
L.P.O. Sousa, K.L Fukushima, V.P. Scagion, **M.H.M. Facure**, D.S. Correa, J.E. Oliveira, D.D. Ferreira
IEEE Sensors Journal, 21, 4957 – 4965 (2021)

xxvi. A review on graphene quantum dots and their nanocomposites: from laboratory synthesis towards agricultural and environmental applications
M.H.M. Facure, R. Schneider, L.A. Mercante, D.S. Correa
Environ. Sci.: Nano, 2020,7, 3710-3734

xxvii. Impedimetric electronic tongue based on molybdenum disulfide and graphene oxide for monitoring antibiotics in liquid media
M.H.M. Facure; R. Schneider; D.M. dos Santos; D.S. Correa
Talanta 217 (2020) 1210392

xxviii. Nanochitin-based composite films as a disposable ethanol sensor
R.S. Andre, D.M. dos Santos, L.A. Mercante, **M.H.M. Facure**, S.P. Campana-Filho, L.H.C. Mattoso, D.S. Correa
Journal of Environmental Chemical Engineering, 8 (2020) 1041632

xxix. Development of an electronic tongue based on a nanocomposite for discriminating flavor enhancers and commercial salts
K.L. Fukushima, V.P. Scagion, **M.H.M. Facure**, A.C.M. Pinheiro, D.S. Correa, C.A. Nunes, J.E. Oliveira
IEEE Sensors Journal, 21, 1250 0 1256 (2021)

xxx. Laser patterning and induced reduction of graphene oxide functionalized silk fibroin
K.T. Paula; M.V Santos; **M.H.M. Facure**; M. B. Andrade; F.L. Araújo; D.S. Correa; S.J.L. Ribeiro; C.R. Mendonça
Optical Materials, 99, 109540 (2020)

xxxi. Electrochemical sensor based on polyamide 6/polypyrrole electrospun nanofibers coated with reduced graphene oxide for malathion pesticide detection
F.L. Migliorini; R.C. Sanfelice; L.A. Mercante; **M.H.M. Facure**; D.S. Correa
Materials Research Express, 7 (2019)

xxxii. Enhanced and selective ammonia detection using In2O3/reduced graphene oxide hybrid nanofibers
R.S. Andre; L.A. Mercante; **M.H.M. Facure**; L.H.C. Mattoso; D.S. Correa
Applied Surface Science, 473, 133-140 (2019)

xxxiii. Conductive electrospun nanofibers containing cellulose nanowhiskers and reduced graphene oxide for the electrochemical detection of mercury(II)
K.B.R.Teodoro; F.L. Migliorini; **M.H.M. Facure**; D.S. Correa
Carbohydrate Polymers, 207, 747-754 (2019)

xxxiv. Ultrasensitive biosensor based on polyvinylpyrrolidone/chitosan/reduced graphene oxide electrospun nanofibers for 17α – Ethinylestradiol electrochemical detection
A. Pavinatto; L.A. Mercante; **M.H.M. Facure**; R.B. Pena; R.C. Sanfelice; L.H.C. Mattoso; D.S. Correa
Applied Surface Science, 458, 431-437 (2018)

xxxv. Femtonsecond laser micromachining of polylactic acid/graphene composites for designing interdigitated microelectrodes for sensor applications
K.T. Paula; G. Gaál; G.F.B. Almeida; M. B. Andrade; **M.H.M. Facure**; D.S. Correa; A. Riul; V. Rodrigues; C.R. Mendonça
Laser Technology, 101, 74-79 (2018)

xxxvi. Detection of trace levels of organophosphate pesticides using an electronic tongue based on graphene hybrid nanocomposites
M.H.M. Facure; L.A. Mercante; L.H.C. Mattoso; D.S. Correa
Talanta 167 (2017) 59–6660

xxxvii. One-pot preparation of PEDOT:PSS-reduced graphene decorated with Au nanoparticles for enzymatic electrochemical sensing of H_2O_2
L.A. Mercante; **M.H.M. Facure**; R.C. Sanfelice; F.L. Migliorini; L.H.C. Mattoso; D.S. Correa
Applied Surface Science, 407, 162-170 (2017)

xxxviii. Solution blow spun PMMA nanofibers wrapped with reduced graphene oxide as an efficient dye adsorbent
L.A. Mercante; **M.H.M. Facure**; D.A. Locilento; R.C. Sanfelice; F.L. Migliorini; L.H.C. Mattoso; D.S. Correa
New Journal of Chemistry, 41, 9087-9094 (2017)

LIST OF TABLES

LIST OF FIGURES

RESUMO

NANOMATERIAIS 0D E 2D BASEADOS EM PONTOS QUÂNTICOS DE GRAFENO E MXENES APLICADOS EM SENSORES E SUPERCAPACITORES. Quantum dots de grafeno (GQDs) são pequenos fragmentos de uma ou poucas camadas de grafeno com dimensões laterais menores que 100 nm. Além de possuírem algumas características similares às do grafeno, como elevada razão área superficial/volume e estabilidade química, os GQDs apresentam um *bandgap* entre suas bandas de valência e de condução eletrônica. A presença do *bandgap* dá origem a uma das propriedades mais investigadas dos GQDs: sua fotoluminescência, que possibilita a aplicação destes materiais em sensores luminescentes. Neste sentido, em um primeiro trabalho, a síntese hidrotermal de GQDs a partir do grafeno oxidado (GO) foi estudada na busca por um material com maior intensidade da fotoluminescência visando sua aplicação em sensores luminescentes. A temperatura da síntese, o pH e a concentração da solução de GO foram avaliados para otimização do rendimento quântico dos GQDs. Um valor otimizado de 8,9% foi obtido. A influência de cada parâmetro na composição e propriedades dos GQDs foi realizada a partir da caracterização físico-química dos materiais. Os materiais sintetizados foram utilizados na detecção de íons Fe^{3+} em soluções aquosas por supressão de luminescência, obtendo-se um limite de detecção de 0.136 μM. Assim como os GQDs, a descoberta de uma nova classe de materiais denominados MXenes foi inspirada na descoberta do grafeno. MXenes são materiais 2D, nos quais camadas de um metal de transição são intercaladas por camadas de carbono e/ou nitrogênio. Tais materiais têm demonstrado alta capacidade de armazenamento de energia, sendo muito utilizados em dispositivos como supercapacitores e baterias. No entanto, o acoplamento das camadas do material e a estreita janela de potencial geralmente alcançada são fatores que limitam a performance desses materiais nesses tipos de aplicações. Em outro trabalho, nanodiamantes (NDs) foram utilizados para evitar o acoplamento das camadas do MXene durante sua utilização como supercapacitor. O efeito obtido com os NDs permitiu uma maior difusão de prótons por entre as camadas do MXene $Ti_3C_2T_x$, resultando em capacitância de 235 F/g (561 F/cm^3) ao ser utilizado em eletrólito 3 M $AlCl_3$. Além disso, uma ampla janela de potencial de 1.2 V foi obtida devido à reduzida atividade da água no eletrólito.

ABSTRACT

0D AND 2D NANOMATERIALS BASED ON GRAPHENE QUANTUM DOTS AND MXENES APPLIED IN SENSORS AND SUPERCAPACITORS. Graphene Quantum Dots (GQDs) are small fragments of one or a few layers of graphene with lateral dimensions inferior to 100 nm. GQDs present some characteristics similar to those of graphene, such as a high surface area/volume ratio and chemical stability. In addition, GQDs present a bandgap between their valence and electronic conduction bands. This bandgap gives rise to one of the most investigated properties of GQDs: their photoluminescence, which enables their application as luminescent sensors. In this sense, in the first work, hydrothermal syntheses of GQDs from graphene oxide (GO) were studied aiming at obtaining a material with greater photoluminescence intensity for application in luminescent sensors. The synthesis temperature, pH of the GO solution, and GO concentration were evaluated to optimize the quantum yield of GQDs. An optimized value of 8.9% was obtained. The influence of each parameter on the composition and properties of the GQDs was carried out from the physical-chemical characterization of the materials. The synthesized materials were used in the detection of Fe^{3+} ions in aqueous solutions by luminescence quenching, obtaining a detection limit of 0.136 μM. Like GQDs, the discovery of a new class of materials known as MXenes was inspired by the discovery of graphene. MXenes are 2D materials, in which transition metal layers are interleaved with carbon and/or nitrogen layers. Such materials have demonstrated high energy storage capacity, being widely exploited in devices such as supercapacitors and batteries. However, the restacking of the MXene layers and the narrow potential window usually obtained limit the performance of these materials in such applications. In another work, nanodiamonds (NDs) were used to prevent the restacking of the MXene layers during its use as a supercapacitor electrode. The pillaring effect obtained with the NDs allowed a greater diffusion of protons between the layers of the MXene $Ti_3C_2T_x$, resulting in a capacitance of 235 F/g (561 F/cm^3) when used in 3 M $AlCl_3$ electrolyte. Furthermore, a wide potential window of 1.2 V could be used due to the reduced water activity in the electrolyte.

SUMMARY

1.   Introduction

1.1.   Graphene quantum dots

The discovery of graphene in 2004[1,2] and the confirmation of its appealing properties have led to an increasing research interest in carbon-based nanostructures.[3,4] One of the youngest members of the carbon nanomaterials family are the graphene quantum dots (GQDs), which first work was reported in 2008.[5] Since then, GQDs have been extensively investigated and applied in several fields due to their remarkable features.[6,7]

GQDs are single or few layers of graphene fragments with lateral dimensions inferior to 100 nm. In this way, they present a 0D graphene lattice in which sp^2 carbon atoms are arranged in a hexagonal honeycomb network and can present two types of edges, namely armchair and zigzag.[4,8] However, they are usually obtained containing oxygen functionalities attached to their core and edges. Although some works differentiate the pristine GQDs from those containing oxygen functionalities, calling the latter graphene oxide quantum dots (GOQDs),[9,10] the vast majority use GQDs for small graphene sheets whether they contain oxygen functionalities or not.[8,11] Usually, GQDs are reported presenting mainly hydroxyl (-OH), epoxy (C-O-C), carbonyl (-C=O), and carboxyl (-COOH) groups.[12,13] As is the case for GO, while carboxyl groups are mostly located on the edges and epoxy on the core of the GQDs, hydroxyl and carbonyl may be present in both sites.[14,15]

The interest in GQDs arises from their physical and chemical properties, most of them similar to those of graphene. However, when graphene sheets are converted into 0D GQDs, the exciton Bohr radius becomes larger than its size, changing the electron distribution and leading to quantum effects (quantum confinement and edge effects) and size-dependent properties.[6,11] In this way, unlike graphene, which does not present a bandgap between the valence and conduction bands, the size reduction of graphene sheets leads to a bandgap opening in GQDs. The presence of this bandgap is responsible for the photoluminescence (PL) exhibited by GQDs, which property makes them suitable for optical applications. Since the bandgap in GQDs is dependent on their size, edge types, and surface chemistry, the PL properties of the GQDs can be tailored by controlling such features.[11,16] In this way, the excitation and emission wavelengths and the PL intensity can be modulated according to the application intended. Furthermore, from being made of carbon, GQDs

exhibit excellent biocompatibility, low cytotoxicity, negligible environmental impact, and photostability, which makes them more eco-friendly than traditional semiconducting quantum dots and fluorescent dye molecules, favoring their use in biomedical and biological applications.[6,17,18]

Unlike other graphene-based materials, GQDs can be easily dispersed in a wide range of solvents, including water, which facilitates their combination with other materials and their use in varied applications.[6,18,19] The dispersion is facilitated by their reduced size, the oxygen functionalities that present charges and enable the formation of intramolecular bonds between GQDs and the solvent molecules, and zigzag edges that have a polar character due to the pair of free electrons.[20–22]

GQDs' properties and structure are related to the synthetic route employed to obtain the material. As is the case for other nanomaterials, GQDs can be obtained by top-down and bottom-up methods.[4,7,8] The first consists of the decomposition and/or exfoliation of carbon-based materials or cutting down graphene-based materials under controlled conditions. Graphite,[23] GO,[24,25] carbon nanotubes (CNTs),[26] and carbon fibers[27,28] have been already reported as precursor materials for GQDs top-down synthesis. Hydrothermal,[29,30] solvothermal,[31,32] electrochemical,[33,34] microwave,[35,36] and ultrasonic[37] syntheses are some top-down methods used to synthesize GQDs. As disadvantages, these methods generally involve several steps, including precursor treatment, the use of strong acids and oxidizing agents, and high temperatures.[7,38] The bottom-up methods consist of the pyrolysis or carbonization of small organic molecules or compounds with an aromatic structure.[7,39] Syntheses from the opening of fullerene[40,41] and pyrolysis of molecules such as glucose,[42,43] citric acid,[44,45] and glutamic acid[46] are examples of bottom-up methods. In general, better control of the GQDs morphology, size, and shape can be achieved with bottom-up synthesis, which requires good control of the experimental conditions.[6,16]

Hydrothermal synthesis

Among the many synthetic routes to obtain GQDs, hydrothermal synthesis using GO as the precursor material has been widely employed. Pan et al. reported in 2010 the first hydrothermal synthesis for obtaining GQDs.[25] In the procedure, GO was thermally reduced to obtain micrometer-sized rippled graphene sheets (GSs). Then, the GSs were oxidized in concentrated strong acids (H_2SO_4 and HNO_3) to obtain smaller-sized sheets ranging from 50 nm to 2 μm and provide oxygen-

functional groups that enabled solubilization in water. After hydrothermal treatment under weakly alkaline conditions (pH = 8), GQDs presenting 9.6 nm average diameter and blue luminescence were obtained. In this work, the authors proposed that the cutting of the graphene sheets occurs through the presence of aligned epoxy and carbonyl groups on the GSs' basal plane (Fig. 1.1). These defects were then attacked during hydrothermal synthesis, cutting the sheets, and resulting in GQDs with carboxylic groups on the edges. Later, the same group proposed another hydrothermal route to obtain smaller and more crystalline GQDs.[47] They used higher temperatures to obtain the GSs and alkaline conditions (pH = 12), which yielded green-luminescent GQDs with a lateral size of ca. 3 nm.
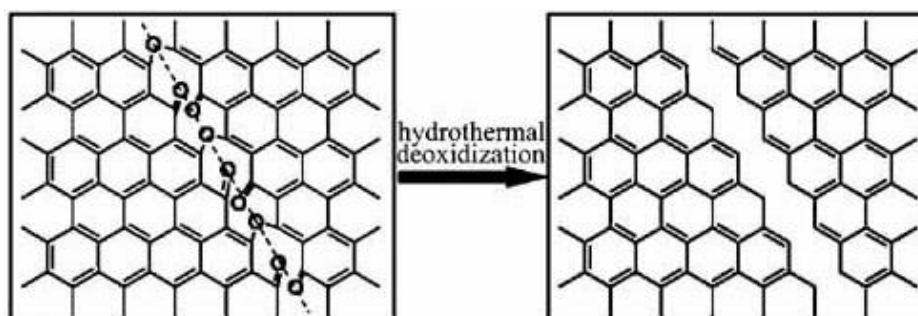
FIGURE 1.1: Proposed mechanism for the hydrothermal cutting of oxidized GSs into GQDs: a chain composed of epoxy and carbonyl pair groups is used to cut the sheet under hydrothermal treatment. Adapted with permission from [25], Copyright 2010 John Wiley and Sons.

Since their reports, many works using GO and hydrothermal synthesis to produce GQDs use an adapted version or the same procedures reported in these works,[48–50] including precursor treatment, multiple steps, and the use of strong acids. These works show that the synthesis conditions exert a direct influence on the materials' properties, structure, and morphology.[4,51] In this scenario, there is room for the search for more viable, safer, faster, and simpler synthesis, as well as for studies that provide a deeper knowledge concerning the influence of the synthesis parameters on the GQDs' features.

Photoluminescence properties

One of the most investigated GQDs' properties is their PL, a phenomenon in which energy is released as electromagnetic radiation (photons) by a material subjected to excitation by a light source. When the fluorescent material

absorbs an energy greater than its bandgap, electrons are promoted from the valence to the conduction band, reaching an excited state. Upon returning to the ground state, energy is released in the form of photons.[52]

The PL intensity of GQDs can be estimated by calculating the quantum yield (QY), which is given by the ratio: photons emitted by fluorescence/photons absorbed by the material. In this way, the QY represents the probability of the material returning from the excited to the ground state by luminescence (radiative emission) rather than by nonradiative processes.[53] As is the case for other carbon nanomaterials, the QY of GQDs is typically low, usually inferior to 25% for GQDs without surface passivation.[54,55]

Although the GQDs' PL is related to the existence of the bandgap in these materials, this PL mechanism in GQDs has not yet been completely elucidated. In general, GQDs present an excitation-dependent PL behavior, which is related to the multiple emission sources presented by the GQDs. The PL in GQDs can be divided into two types of emissions: the intrinsic state emission, related to the GQDs' morphology (size and edges), and the defect state emission, related to the functionalities or vacancies created on their surface.[54,56] Because each one responds in a particular way to the excitation used, one may be dominant over the others in a certain wavelength, leading to excitation-dependent behavior.[54,57]

The size of the GQDs will reflect on the bandgap energy that, as a consequence, will change the PL behavior of the GQDs. Materials with a larger bandgap release more energy when the electron returns to the ground state, which reflects in a shorter emission wavelength and a higher PL intensity.[58] Such effect was observed by Liu et al., in which a decrease in the PL intensity was observed as the size of the GQDs increased.[59] As a consequence, quantum confinement and edge effects become less relevant, reducing the bandgap of GQDs and, consequently, their photoluminescent properties. In theory, the bandgap of GQDs can vary from about 7 eV (the bandgap of benzene) to zero, the graphene bandgap.[60] GQDs are reported to emit light at several wavelengths, from ultraviolet (UV) to red, with emission at blue and green regions being the most common.[61,62] The GQDs edges also exert influence on the PL behavior, since armchair and zigzag edges exhibit different quantum confinement properties. GQDs with armchair edges present larger bandgaps than those with zigzag edges, leading to a blue shift in the PL emission.[58,63]

While the effect of size and edges of GQDs on their PL behavior is well understood, there is no consensus about the effect of the functionalities present on the GQDs' surface yet. Yang's group has suggested that the PL mechanism in GQDs results from competition among various emission centers.[20,64,65] They proposed that hydroxyl groups favor the blue PL emission, while the carbonyl and carboxylic groups on the GQDs' edges contribute to a green emission. Epoxy groups, in turn, have been shown to act as traps providing non-radiative recombination and decreasing the PL intensity of the material.[6,36,52] Removing the oxygen functionalities of the GQDs' surface also leads to PL behavior changes. Jang et al. showed that the chemical reduction of GQDs led to blue emissions due to the formation of sp^2 domains, while sp^3 carbon hybridization from the bonding with oxygen groups contributed to green emissions.[66] In addition, surface passivation[67] and doping GQDs with heteroatoms has been shown to affect the PL mechanism in varied ways, depending on the element used, and the site of functionalization, for example.[31,68,69] Such strategies and the GQDs reduction are also frequently used to enhance the QY of GQDs.

The GQDs' PL properties enable their use as fluorescent sensors. Many analytes have been detected using GQDs as luminescent probes, including metal ions,[70,71] small molecules (such as dopamine, 2,4,6-trinitrotoluene (TNT), and picric acid),[72–74] and large biomaterials, including tumor cells and carcinoembryonic antigen.[75,76] In general, the analyte detection is made by quenching the GQDs luminescence intensity upon physical or chemical binding that can change their electronic structure. In this regard, the PL intensity, i.e., the GQDs' QY is very important for achieving low limits of detection (LOD) and high sensitivity,[77,78] which was also explored in this PhD project.

1.2. MXenes

In addition to increasing the research interest in carbon-based nanomaterials, the discovery of graphene also fostered the investigation for new two-dimensional (2D) materials. One class of materials inspired by the graphene discovery is the MXene family. MXenes are carbides and nitrides of transition metals presenting the general formula of $M_{n+1}X_nT_x$, where M is a transition metal, X is either carbon and/or nitrogen, and T_x represents the terminations on the surface of the outmost transition metal layers.[79,80] As shown in Fig. 1.2, many elements have been used to obtain

different MXenes. By combining different metal atoms with several possible terminations, an unlimited number of MXenes can be obtained and, as a consequence, materials with distinct properties can be synthesized.[80]
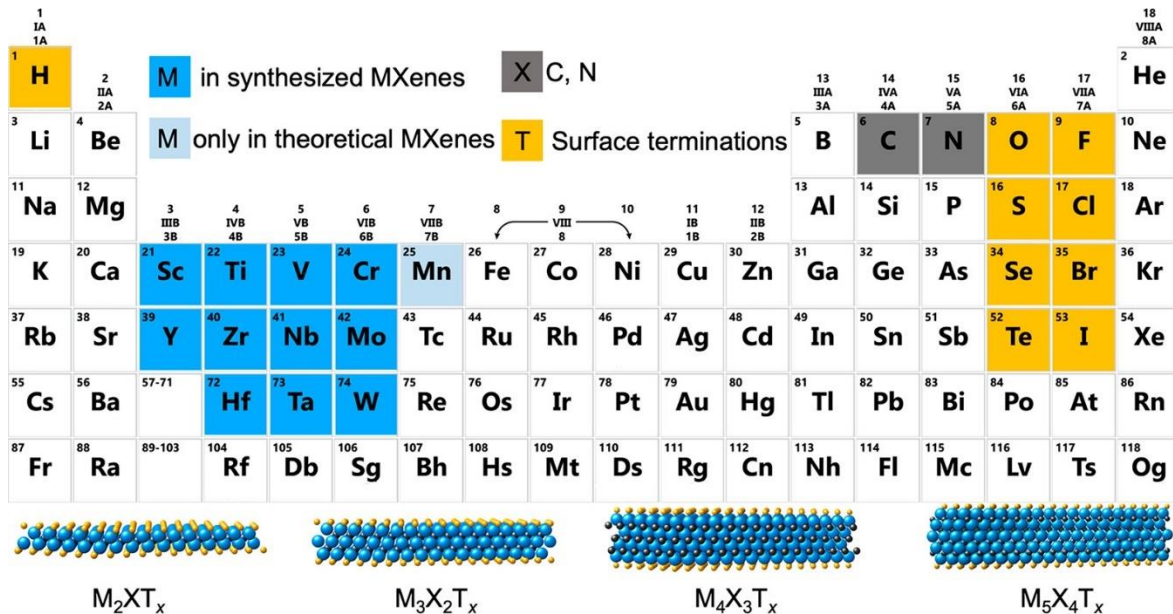
FIGURE 1.2: Periodic table showing possible MXenes compositions. Four typical MXene structures are schematic illustrated at the bottom. Reproduced with permission from [80], Copyright 2021 American Chemical Society.

Most of the MXenes reported so far have been obtained using MAX phases as the precursor material (Fig. 1.3). MAX phases are layered ternary carbides and nitrides presenting a $M_{n+1}AX_n$ formula, in which M is a transition metal, X is carbon and/or nitrogen, while A is an element of the IIIA or IVA group.[79,81] In this way, the A element in the MAX phase can be regarded as the layer that keeps the MXenes together in the structure by M-A bonds. Therefore, unlike other 2D materials in which only van der Waals forces keep them stacked, enabling the isolation of layers through shear or other mechanical strategies, MXenes are usually obtained from the 3D precursor by selectively etching the A element from MAX phases. The selective etching is possible because the M-A bonding is weaker than the M-X bonds, making the A layer more chemically reactive.[82,83]
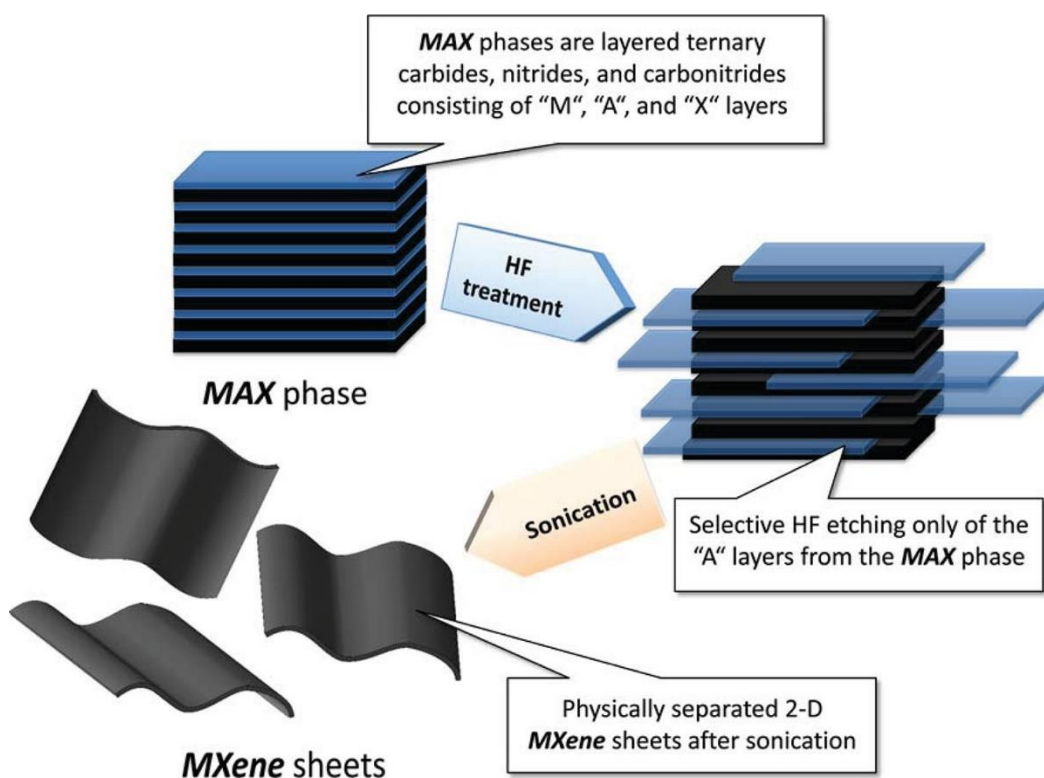
FIGURE 1.3: Schematic illustration of MXenes synthesis: etching and delamination. Reproduced with permission from [83], Copyright 2012 American Chemical Society.

The synthesis method employed is crucial for the MXene properties obtained. Besides the morphological aspects such as size and defects that will play a fundamental role in the MXene physicochemical features, the surface terminations of MXenes are also highly dependent on the synthesis conditions.[84,85] Although there are some synthesis routes that do not require the use of fluoride-containing solvents, the main MXene synthesis methods make use of fluoride-containing acidic solutions,[86,87] such as hydrofluoric acid (HF) or a mix of lithium fluoride and hydrochloric acid (HCl).[81,88] Since too high temperatures and strong etching agents can lead to the formation of undesirable structures, such as rock salts and the etching of both the A and M elements, the precise balance between temperature and the activity of the etchant needs to be carefully controlled during synthesis.[82,83]

Titanium Carbide (Ti$_3$C$_2$T$_x$)

The first MXene reported was the titanium carbide (Ti$_3$C$_2$T$_x$) in 2011 by Gogotsi and Barsoum groups.[89] Since then, Ti$_3$C$_2$T$_x$ has been the most studied MXene and has been used in many different areas,[79] such as in sensors,[90,91] energy storage devices,[92–94] electromagnetic interference shielding,[95,96] and biomedical

applications.[97,98] Besides presenting high strength and stiffness, [84,99] good flexibility, and large specific surface area,[83,100] unlike most of the previous 2D materials, $Ti_3C_2T_x$ displays a metallic electrical conductivity, with values as high as 20 kS cm^{-1} being reported.[80,101]

Since top-down selective chemical etching using HF is the most reported synthesis used to obtain $Ti_3C_2T_x$, the synthesized material presents surface termination consisting of OH, O, and F in different ratios, depending on the synthesis conditions used.[79,80] In addition to strongly influencing the material properties, the surface terminations endow hydrophilicity to the MXene, enabling the preparation of aqueous colloidal solutions and the use of a wide range of solvents, which is a severe limitation for other 2D materials.[80,102]

The surface terminations are also crucial in the most explored application of $Ti_3C_2T_x$, i.e., in energy storage. It has been demonstrated that the high capacitance values reported in acidic electrolytes are related to the surface redox reactions between the protons inserted into the MXene layers and the O terminations, which are converted in OH groups (Eq. 1.1), resulting in the characteristic pseudocapacitive behavior.[103–105] Other features, such as fast charge transport arising from the electrochemically active sites, the negative surface charge, and the spontaneous intercalation of cations, also contribute to the highlighted performance of the $Ti_3C_2T_x$ as supercapacitor.[80,106,107]

$$Ti_3C_2O_x(OH)_yF_z + \delta\bar{e} + \delta H^+ \leftrightarrow Ti_3C_2O_{x-\delta}(OH)_{y+\delta}F_z \quad \text{(Eq. 1.1)}$$
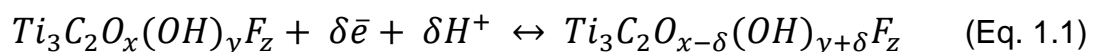
If, on the one hand, $Ti_3C_2T_x$ has characteristics that enable achieving good performance for energy storage, on the other hand, the material may present some limitations. One of the drawbacks presented by $Ti_3C_2T_x$ when used as a supercapacitor electrode is the restacking of the MXene layers. The restacking limits ion transport in thick films and impairs the intercalation of protons between the layers, reducing the occurrence of redox reactions and decreasing the capacitance performance.[105,108] In this regard, some strategies to circumvent the MXene restacking have been proposed. Xia et al., for instance, reported vertically aligned MXene sheets, in which diffusion limitations are minimized and a high capacitance value is obtained.[109] Another alternative is the use of nanomaterials that can act as pillars between the

MXene layers, preventing restacking, increasing ions diffusion, and maintaining high capacitance during measurements.[108,110,111]

Using acidic electrolytes with $Ti_3C_2T_x$ gives rise to high capacitance values due to the presence of protons. However, such electrolytes can be usually used only in relatively narrow potential windows (not higher than 1V).[105,112,113] The impossibility of using larger potential windows is due to the high amount of water present in these electrolytes. In these cases, the decomposition of the electrode and electrolyte occurs more easily, reducing the operating potential window of the device.[114] To enlarge the voltage window and as a consequence increase the energy density of the supercapacitor, highly concentrated electrolytes can be used. In this manner, the water activity is reduced making it difficult for parasitic side reactions to occur, which enables the exploration of the extreme potential regions. On the other hand, the low amount of water generally increases diffusion limitations of the electrolyte and leads to moderate capacitance values.[93,115,116] The decrease in capacitance also has a contribution of the absence of the hydrogen bond network provided by the water that contributes to the energy storage mechanism.[92] In this scenario, there is room for the search for the precise combination between electrode materials architecture and electrolyte composition, which was also explored in this PhD project.

2.   Goals and Overview

The objective of this thesis was to harness the potential of emerging 0D and 2D nanomaterials, specifically graphene quantum dots and $Ti_3C_2T_x$ MXene, respectively, with the aim of enhancing sensor capabilities (in the case of GQDs) and optimizing energy storage devices (in the case of MXenes). In this regard, the goal was to rationally design experiments and nanostructures to overcome existing limitations regarding the synthesis of GQDs and the use of MXene as a supercapacitor.

As specific goals, we can cite:

– To evaluate parameters of GQDs hydrothermal synthesis aiming at optimizing the quantum yield value of the material through a simpler and more viable synthesis;

– To characterize the synthesized GQDs in order to correlate their physical-chemical properties with the parameters evaluated in the syntheses;

– To apply the synthesized GQDs as fluorescent sensors;

– To synthesize $Ti_3C_2T_x$ and obtain a nanocomposite using a nanomaterial that can act as pillars between the MXene sheet;

– To use the MXene-based hybrid material as a supercapacitor electrode to achieve high capacitance and wide potential window.

Chapters Overview

Initially, hydrothermal synthesis was investigated to obtain GQDs with optimized QY values. The influence of the concentration and the pH of the GO solution and the temperature of the synthesis on the materials' properties was evaluated. Then, the fluorescent detection of Fe^{3+} was performed with selected materials. Chapter I presents the main results, indicating that GQDs can be rationally synthesized aiming at specific applications, and shows the detection performance of the synthesized materials.

In Chapter II, nanodiamonds (NDs) were used as pillars between the $Ti_3C_2T_x$ layers. The pillaring effect prevented the restacking of the MXene layers, favoring proton diffusion, while the use of 3 M $AlCl_3$ enabled the achievement of high capacitance and a large potential window.

General conclusions and future perspectives are presented in the sequence in which the evaluation of the results reported is provided.

3. Chapter I: Graphene quantum dots synthesis and photoluminescence sensing application*

*The content of this chapter is an adaptation of the article entitled: "**Rational hydrothermal synthesis of graphene quantum dots with optimized luminescent properties for sensing applications**" by M. H. M. Facure, R. Schneider, L. A. Mercante, and D. S. Correa, published in Materials Today Chemistry.

Reference: *Materials Today Chemistry* 23 (2022) 100755.[117]

3.1. Abstract

Hydrothermal synthesis using graphene oxide (GO) as a precursor has been used to produce luminescent graphene quantum dots (GQDs). However, such a method usually requires many reagents and multistep pretreatments, while can give rise to GQDs with low quantum yield (QY). Here, we investigated the concentration, the temperature of synthesis, and the pH of the GO solution used in the hydrothermal method through factorial design experiments aiming to optimize the QY of GQDs to reach a better control of their luminescent properties. The best synthesis condition (2 mg/mL, 175 °C, and pH = 8.0) yielded GQDs with a relatively high QY (8.9%) without the need of using laborious steps or dopants. GQDs synthesized under different conditions were characterized to understand the role of each synthesis parameter in the materials' structure and luminescence properties. It was found that the control of the synthesis parameters enables the tailoring of the amount of specific oxygen functionalities onto the surface of the GQDs. By changing the synthesis' conditions, it was possible to prioritize the production of GQDs with more hydroxyl or carboxyl groups, which influence their luminescent properties. The as-developed GQDs with tailored composition were used as luminescent probes to detect Fe^{3+}. The lowest limit of detection (0.136 μM) was achieved using GQDs with higher amounts of carboxylic groups, while wider linear range was obtained by GQDs with superior QY. Thus, our findings contribute to rationally produce GQDs with tailored properties for varied applications by simply adjusting the synthesis conditions and suggest a pathway to understand the mechanism of detection of GQDs-based optical sensors.

3.2. Introduction

The last decade has witnessed an unprecedented number of investigations on the synthesis and application of graphene-based materials owing to their remarkable electrical and mechanical properties.[1,118,119] Among many members of the graphene family, graphene quantum dots (GQDs) have been attracting enormous interest because of their tunable bandgap, owing to their reduced size compared with standard graphene sheets.[4,38] The bandgap is responsible for the photoluminescence (PL) properties of GQDs, which, in turn, depends on their characteristics (e.g. functional groups, size, edges, and so on).[4,6,58,120] In this regard,

the synthesis method used to obtain GQDs is determinant for the material structure and consequently their PL behavior.[6,38,58]

The syntheses of GQDs are broadly classified into top-down and bottom-up methods. A highly used top-down strategy to produce GQDs is the hydrothermal method using graphene oxide (GO) as the precursor material.[4,39] In this route, the GO is 'broken' into tiny fragments under high temperature and high-pressure conditions in a sealed autoclave.[6,39] The use of GO as a precursor leads to GQDs with different oxygen functionalities, such as hydroxyl, carboxyl, carbonyl, and epoxy groups, which has a prominent influence on their properties.[49,50] In this regard, the parameters used in the hydrothermal synthesis, such as GO concentration, temperature, and pH, will affect the GQDs composition and, therefore, are key in modulating their properties.[4,6]

Hydrothermal synthesis using GO as the precursor material was first proposed by Pan et al.[25] in 2010 and was further improved in 2012,[47] giving rise to GQDs with quantum yields (QYs) of 6.9% and 7.5%, respectively. Since then, several studies related to the production of GQDs by hydrothermal methods using GO have been reported.[49,50] To obtain GQDs with enhanced values of QY, some of these procedures make use of precursor pretreatment and/or the addition of other reagents to favor the GO sheets cutting. The enhancement of QY can lead to improved performances, especially for sensing applications.[6,61,121] However, these approaches generally use multiple steps, strong acid reagents, and other materials to induce GO cutting, which makes the process laborious.[121–123] In this scenario, there is a need to seek simpler syntheses that require fewer steps, milder conditions, a smaller number of reagents but that still provide GQDs with comparable or enhanced QY values.[121] In addition, understanding the influence of the most relevant synthesis' parameters is mandatory to obtain tailored GQDs' structures with precise control.[18,124] In this way, GQDs possessing the desired characteristics can be smartly produced to be used in a given application.

Because of their large surface area-to-volume ratio, fast charge transfer, and multiple analyte recognition possibilities (e.g. functionalized groups, heteroatom doping, and π-π interaction), GQDs have been widely explored as a constituent material in electrical, electrochemical and optical sensors.[8,61] Regarding optical sensing, GQDs present advantages over commercial organic dyes and semiconductor quantum dots, including better biocompatibility and resistance to photobleaching, as well as lower toxicity, which prompt them to be used in biomedical and environmental

applications. Moreover, the photostability of GQDs enables high sensitivity and selectivity. In addition, GQDs are soluble in aqueous and many organic solvents.[78,125] In this way, changes in the fluorescence intensity of GQDs upon analyte interaction is a simple, fast, and reliable sensing method that does not require the use of expensive instrumentation and laborious sample treatment.[78] However, further investigations on the fluorescence properties of GQDs are still necessary to thoroughly understand the performance of these materials as PL sensors.[17,65]

In this work, we report the use of the hydrothermal method and the factorial design approach to rationally produce GQDs with controllable surface chemistry and optimum PL features for sensing applications. The concentration of GO (C_{GO}), the temperature of the synthesis (T), and the solution pH were optimized to obtain GQDs with higher QY values, as illustrated in Fig. 3.1(a). A QY of 8.9% was obtained without the need of pretreatment steps or the use of specific reagents to act as 'scissors' in the GO cutting process. To correlate the QY values with the materials properties, GQDs produced by three selected syntheses conditions were fully characterized using spectroscopy techniques and thermogravimetric analysis (TGA). The behavior of the obtained materials was related to the amount of specific functional groups present in the GQDs structure. Finally, the GQDs were applied in the PL detection of Fe^{3+}, as illustrated in Fig. 3.1(b), presenting different performances in accordance with their composition.

(a) GQDs production

Solution preparation

Hydrothermal synthesis

GQDs with optimized luminescent properties

Temperature controller

pH meter

t = 10 h

pH = 4.5, 8.0 and 9.5

[GO] = 1.25, 2.00 and 2.75 mg/mL

T = 130, 160 and 190 °C

GQDs-1
QY = 2.0 %

GQDs-2
QY = 6.0 %

GQDs-3
QY = 8.9 %

(b) Fe^{3+} detection

Fe^{3+} ions

PL measurements

PL Intensity

$[Fe^{3+}]$

Wavelength (nm)
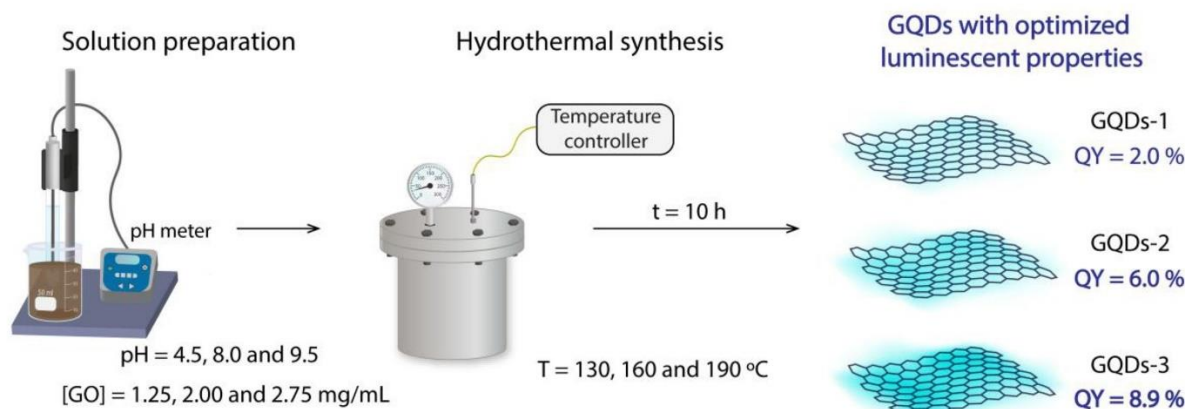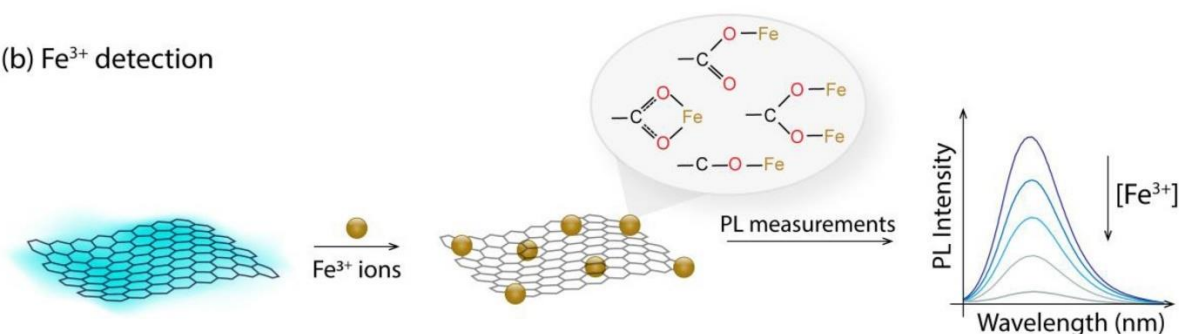
FIGURE 3.1: Schematic illustration of (a) the hydrothermal synthesis optimization and the production of GQDs with distinct composition and PL properties. (b) GQDs application in fluorescent detection of Fe^{3+}. GQD, graphene quantum dot; PL, photoluminescence. Reprinted with permission from Facure *et. al.*[117], Copyright 2022 Elsevier.

3.3. Experimental Section

3.3.1. Materials

Graphite and potassium permanganate ($KMnO_4$) were obtained from Dinamica, Brazil. Sulfuric acid (H_2SO_4), hydrochloric acid (HCl), sodium hydroxide (NaOH), hydrogen peroxide (H_2O_2), ferric chloride hexahydrate ($FeCl_3 \cdot 6H_2O$), copper(II) chloride dihydrate ($CuCl_2 \cdot 2H_2O$), tin(II) chloride dihydrate ($SnCl_2 \cdot 2H_2O$), aluminum chloride hexahydrate ($AlCl_3 \cdot 6H_2O$), nickel(II) chloride hexahydrate ($NiCl_2 \cdot 6H_2O$), cobalt(II) chloride hexahydrate ($CoCl_2 \cdot 6H_2O$), magnesium chloride hexahydrate ($MgCl_2 \cdot 6H_2O$), zinc nitrate ($Zi(NO_3)_2$), mercury(II) sulfate ($HgSO_4$), cadmium nitrate tetrahydrate ($Cd(NO_3)_2 \cdot 4H_2O$), manganese(II) acetate ($C_4H_6MnO_4$), lithium chloride (LiCl), potassium chloride (KCl), and sodium chloride (NaCl) were

purchased from Sigma-Aldrich. The chemicals were used as received, and all aqueous solutions were prepared using double-distilled water.

3.3.2. Syntheses of GQDs

GQDs were synthesized by hydrothermal method using GO as the precursor material. The GO was synthesized through an eco-friendly modified Hummers' method previously reported elsewhere.[126–128] To be used in the GQDs syntheses, a stock aqueous dispersion of GO (100 mL) was prepared with a concentration between 4 and 6 mg/mL. Briefly, the GO powder obtained in the Hummers' method was initially dispersed by ultrasonic probe sonication (Branson Digital Sonifier SFX 550) (11 W) for 20 min. The dispersion was left stirring overnight and then centrifuged at 8000 rpm for 30 min to remove the unexfoliated material.

The syntheses of the GQDs were carried out in a 50 mL Teflon lined stainless steel autoclave. To obtain the optimization of the C_{GO}, T, and pH used in the GQDs syntheses, factorial experiments were designed changing these parameters and fixing the reaction time (10 h) and the GO dispersion volume (40 mL). For the GQDs syntheses, the GO stock dispersion was diluted to the desired concentration, and the pH was changed using aqueous solutions of NaOH or HCl. Then, the dispersion was sealed in the autoclave and heated at 1 ºC/min to the temperature of the synthesis, which was maintained for 10 h. The GQDs solution was obtained by filtering the resultant product of the hydrothermal synthesis with 0.22 µm syringe filters. The GQDs powder used in the characterization techniques was obtained by freeze-drying (L108 Liotop) this filtered solution.

3.3.3. Characterization

Transmission electron microscopy (TEM) and high-resolution TEM images of GQDs were obtained using a FEI Tecnai G2F20 microscope (accelerating voltage of 200 kV). Atomic force microscopy (AFM) images of GQDs were obtained using a Bruker MultiMode8 microscope. The samples were prepared by placing a small drop of the GQDs suspensions (in water) on a carbon-coated copper grid and mica substrates for the TEM and AFM images, respectively. For the AFM images, the GQDs solutions were previously dialyzed using a membrane with nominal molecular weight cut-offs of 2 kDa.

The PL experiments were performed in a Shimadzu (RF-5301PC) spectrofluorometer using a quartz cuvette. UV-vis absorption spectroscopy of the solutions was performed using a Shimadzu (UV-1900) spectrophotometer. The absorbance spectra were collected from 200 to 700 nm.

Fourier transform infrared (FTIR) spectroscopy was carried out in a Bruker Vertex 70 equipment using the ATR mode for the freeze-dried GQDs powders. 64 scans were collected from 4000 to 400 cm^{-1} at a 4 cm^{-1} resolution.

X-ray photoelectron spectroscopy (XPS) analyses were performed using an ESCALAB-MKII spectrometer with an X-ray source excitation of 1486.6 eV (Al Ka radiation). The C1s spectrum (284.6 eV) was used as references for the binding energies with an accuracy of ±0.1 eV. Silicon wafers were used as substrates for the GQDs deposition.

TGA was carried out using a TGAQ500 (TA Instruments) analyzer. The freeze-dried GQDs (ca. 5 mg) were heated in platinum pans from room temperature to 800 ºC at a ramp rate of 10 ºC/min using nitrogen flux (40 mL/min).

3.3.4. QY measurements

The QY values of the GQDs in water were calculated using the comparative method[129] through the following equation:

$$QY = QY_R \frac{I}{I_R} \frac{A_R}{A} \frac{n^2}{n_R^2} , \qquad \text{(Eq. 3.1)}$$

where I is the measured integrated fluorescence intensity, A is the optical density, and n is the refractive index of the solvent. A can be obtained by the GQDs absorbance value recorded in the UV-vis spectrum at the wavelength used in the PL excitation (λex). The absorbance value should be inferior to 0.1 to minimize reabsorption effects. I can be obtained through the area under the luminescence spectrum.[6,130] The subscript R is referred to the reference. Here, quinine sulfate was used as the standard reference in 0.1 mol/L H_2SO_4 ($QY_R = 54\%$). The QY values were obtained using $\lambda ex = 320$ nm.

3.3.5. Fe^{3+} detection

A quartz cuvette was filled with 2 mL of the GQDs solution and Fe^{3+} was added in various concentrations using stock solutions with concentrations of 1×10^{-3}

and 10 $\times$ 10^{-3} mol/L, leading to a PL quenching. The measurements were performed at room temperature ($\approx$25 °C) using a fixed λex at 320 nm and recording the PL emission intensity at 442 nm. The interference tests were performed by adding 5 μL of a 0.1 mol/L solution containing the other metal ions. All the sensitivity and selectivity experiments were conducted in triplicate.

3.4. Results and discussion

3.4.1. Optimization of GQDs hydrothermal synthesis

A factorial design was used to evaluate the best conditions to optimize the QY of the GQDs produced by the hydrothermal method. In this regard, previous experiments were performed to evaluate the parameters to be used in the factorial design and their values. C_{GO}, T, and pH showed to be the most relevant parameters in the QY of the synthesized GQDs. Table 3.1 shows the full 2^3 factorial designs with four center points and the resultant QY of each synthesis.

TABLE 3.1: Factorial design for C_{GO}, T, and pH parameters (variables) and the QY values (response) of the GQDs obtained in each synthesis. The coded levels are in parenthesis.

Experiment	C_{GO} (mg/mL)	T (°C)	pH	QY (%)
1	1.25 (-1)	130 (-1)	4.5 (-1)	5.0
2	2.75 (+1)	130 (-1)	4.5 (-1)	4.2
3	1.25 (-1)	130 (-1)	9.5 (+1)	6.6
4	2.75 (+1)	130 (-1)	9.5 (+1)	6.0
5	1.25 (-1)	190 (+1)	4.5 (-1)	2.0
6	2.75 (+1)	190 (+1)	4.5 (-1)	1.6
7	1.25 (-1)	190 (+1)	9.5 (+1)	5.9
8	2.75 (+1)	190 (+1)	9.5 (+1)	5.5
9	2.00 (0)	160 (0)	7 (0)	8.0
10	2.00 (0)	160 (0)	7 (0)	7.8
11	2.00 (0)	160 (0)	7 (0)	8.3
12	2.00 (0)	160 (0)	7 (0)	7.3

Analysis of variance was used to verify the significance of the parameters and their interactions.[131] At a 95% of confidence level, all the parameters were found to be significant as well as the quadratic coefficient for C_{GO} and the interaction between T and pH. The model obtained can be expressed by Eq. A1. The response surface plots of the 2^3 factorial design with the effect of C_{GO} and T and C_{GO} and pH on the QY of the GQDs are presented in Fig. 3.2(a) and (b), respectively. As can be noticed, regardless of the T or pH values, the optimal C_{GO} for obtaining a higher QY is around 2 mg/mL. However, in this first design, an optimal value for pH and T was not obtained. In this way, based on the values of QY obtained in the first factorial design (Table 3.1) and after further investigations to evaluate the values for T and pH, a reduced design 2^2 with two center points was proposed (Table 3.2), fixing the C_{GO} at the optimal value (2 mg/mL).
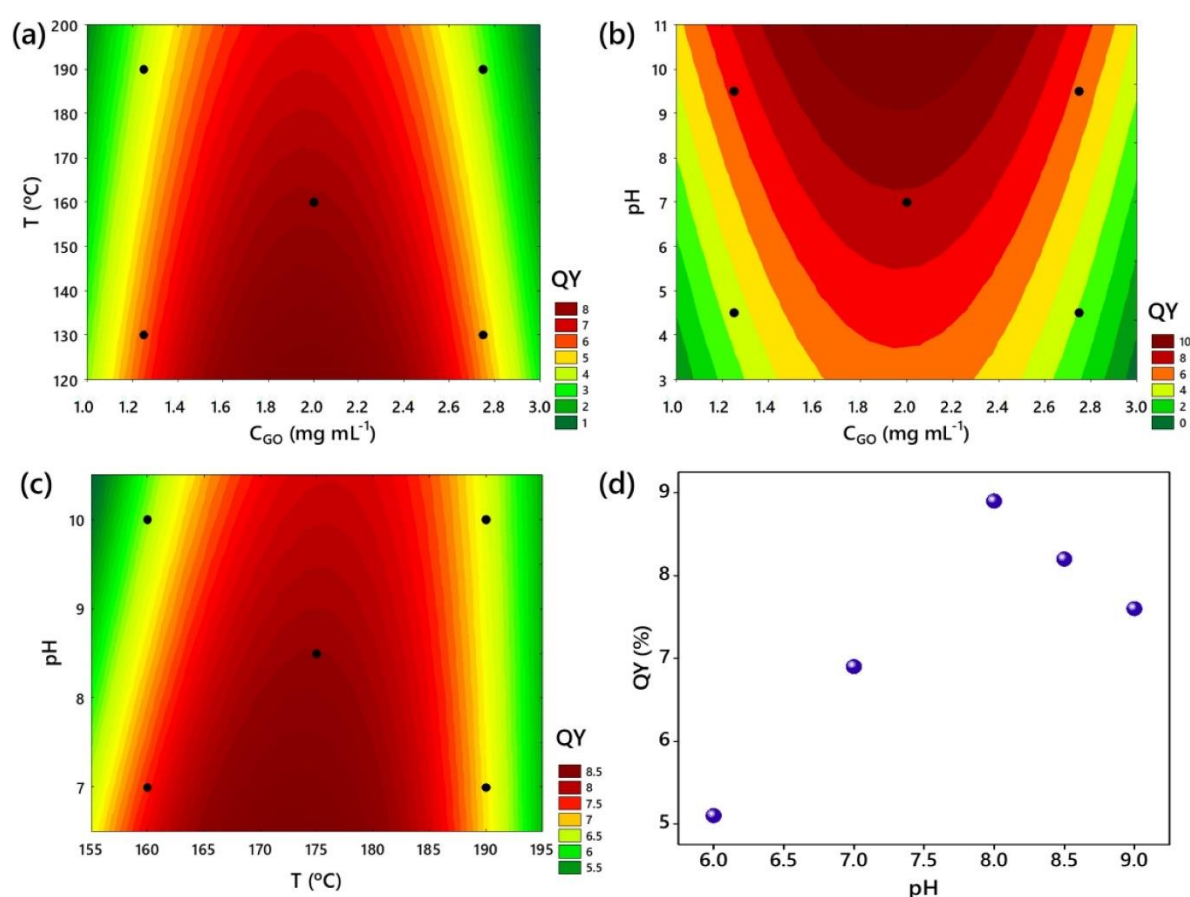
FIGURE 3.2: Response surface plots obtained by the first design (2^3) showing the effects of (a) T and C_{GO} and (b) pH and C_{GO} on the QY of the GQDs. (c) Response surface plots obtained by the reduced design (2^2) showing the effects of pH and T on the QY of the GQDs. The black dots represent the conditions in which the syntheses of the factorial design were performed. (d) Variation of the QY obtained in the GQD syntheses for different pH values (C_{GO} = 2 mg/mL, T = 175 ºC). GQD, graphene

quantum dot; QY, quantum yield. Reprinted with permission from Facure *et. al.*[117], Copyright 2022 Elsevier.

TABLE 3.2: Factorial design for T and pH parameters (variables) and the QY values (response) of the GQDs obtained in each synthesis. The coded levels are in parenthesis.

Experiment	T (°C)	pH	QY (%)
1	160 (-1)	7 (-1)	7.5
2	190 (+1)	7 (-1)	6.8
3	160 (-1)	10 (+1)	6.4
4	190 (+1)	10 (+1)	6.6
5	175 (0)	8.5 (0)	8.1
6	175 (0)	8.5 (0)	8.3

The same statistical treatment used in the first design was again performed for the reduced design (2^2), which model can be expressed by Eq. A2. The design resulted in an optimal value for T ($\approx$175 °C), as shown in Fig. 3.2(c). The reduced design did not yield the best pH value. To find the optimum pH, the C_{GO} and T were fixed (2 mg/mL and 175 °C, respectively), and the pH of the synthesis was varied. Fig. 3.2(d) shows that to obtain the highest QY, the optimum pH value for the hydrothermal syntheses is 8.0. In the optimized condition, i.e. C_{GO} = 2 mg/mL, T = 175 °C, and pH = 8, the highest QY was found to be 8.9%.

As can be compared with other syntheses performed (Tables 3.1 and 3.2), the optimum synthesis yielded the highest QY value. Such value is comparable or even superior to other syntheses reported in the literature, in which the GO is pretreated or scissoring reagents are used, as shown in Table A1. In this way, by using the optimum parameters for the hydrothermal synthesis, one can produce GQDs with enhanced QY values without making use of multiple synthesis steps, additional reagents, or laborious processes.

It is worth mentioning that to achieve even higher QY values, other synthesis methods can be used, as well as doping or surface modification of the GQDs. In general, the enhancement in the QY is generally associated with the improvement of the electron density and the creation of additional electronic states that act as new pathways for photon absorption and PL emission.[132–135] Some GQDs reported in the literature that use such strategies are shown in Table A2.

3.4.2. Characterization of GQDs

TEM images and the corresponding size distribution (Fig. A1a-c) show that the synthesized GQDs have a near-spherical morphology with an average size of 5.8 ± 0.9 nm. Furthermore, high-resolution TEM images (Fig. A1d) reveal the crystalline nature of GQDs with an inter lattice distance of 0.21 nm, which corresponds to (102) diffraction planes of sp^2 graphitic carbon structure.[136] Physical-chemical characterizations of the GQDs were carried out to understand which features in their structure are responsible for the QY increment and learn the influence of each of these three parameters in the GQDs properties. To this end, three hydrothermal synthesis' conditions yielding GQDs with different QY were chosen to be characterized and later applied as optochemical sensors for Fe^{3+} detection. Table 3.3 shows the parameters used and the QY obtained in each synthesis condition. Hereafter, GQDs-1, GQDs-2, and GQDs-3 will be used in reference to each synthesis condition shown in Table 3.3. GQDs-3 is the material obtained using the optimal values of C_{GO}, T, and pH, as discussed in the previous section.

TABLE 3.3: Values of the parameters used in the GQD syntheses and the QY obtained.

Sample	C_{GO} (mg/mL)	T (ºC)	pH	QY (%)
GQDs-1	1.25	190	4.5	2.0
GQDs-2	2.00	130	9.5	6.0
GQDs-3	2.00	175	8.0	8.9

AFM images of the GQDs are shown in Fig. 3.3. The images show that the GQDs are well dispersed and the height of all the samples are between 0.5 and 1.5 nm, indicating the presence of 1-3 layers.[30]
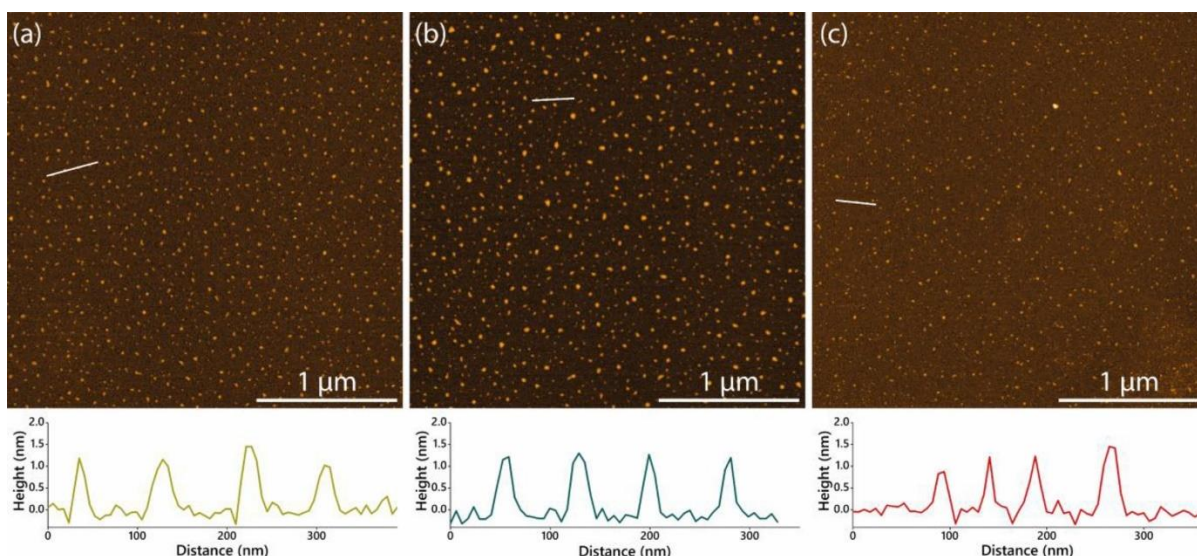
FIGURE 3.3: AFM images of (a) GQDs-1, (b) GQDs-2, and (c) GQDs-3. The graphs below the images show the height profile of the GQDs along the white lines in the images. AFM, atomic force microscopy; GQD, graphene quantum dot. Reprinted with permission from Facure *et. al.*[117], Copyright 2022 Elsevier.

Fig. 3.4(a) shows the UV-vis spectra of GQDs-1, GQDs-2, and GQDs-3. The spectra were recorded with the filtered solutions obtained from the hydrothermal syntheses without dilution. The three materials presented a peak at 230 nm assigned to the π-π^* transition of the C=C bonds in the GQDs core. In the region between 300 and 400 nm, it is possible to observe peaks related to the n-π^* transitions of the different oxygen functional groups in the GQDs structure.[137–139] Also, the UV-vis analyses indicate that the C_{GO} influences the amount of GQDs obtained. For instance, the GQDs-1, which synthesis was performed with a C_{GO} = 1.25 mg/mL, presented the lowest absorbance, indicating a smaller concentration of the GQDs in solution. On the other hand, the GQDs-2 and GQDs-3 synthesized with the same C_{GO} (2 mg/mL) showed very similar absorbance values, indicating similar GQDs concentrations. Thus, the C_{GO} seems to play two important roles in the obtained GQDs solution. Besides the relationship with the amount of the synthesized GQDs, C_{GO} = 2 mg/mL was shown to be the ideal concentration for the production of GQDs with higher QY values, as shown in Table 3.3. A possible reason may be associated with the interaction between GO sheets. Concentrations higher than the optimum value can influence the mechanism of sheet size reduction, while lower concentrations may not reach the best thermodynamic conditions for the synthesis of GQDs.
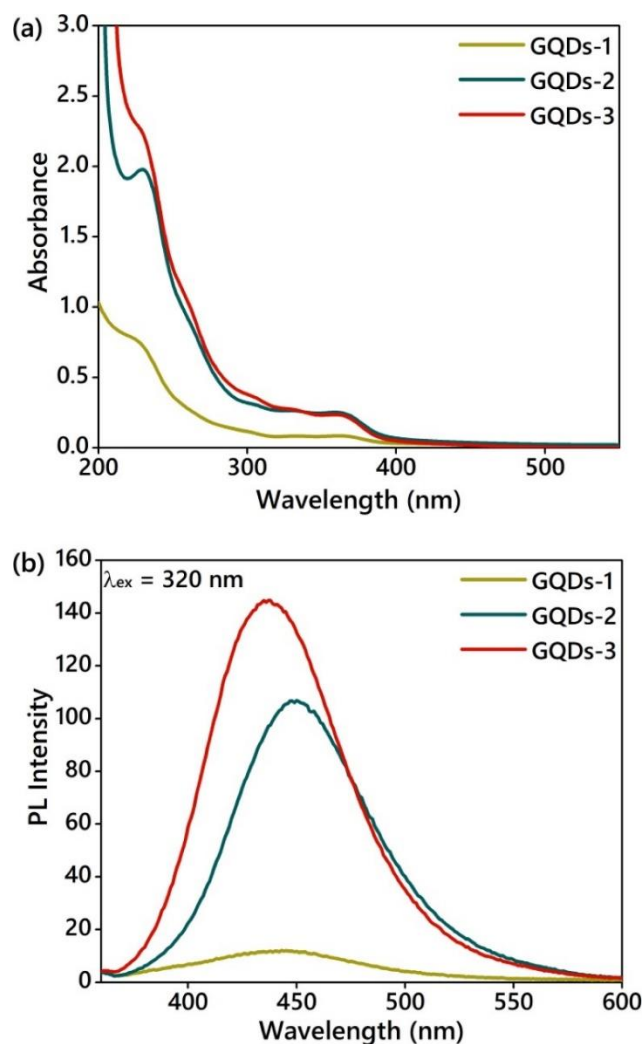
FIGURE 3.4: (a) UV-vis absorption and (b) PL emission spectra of GQDs-1, GQDs-2, and GQDs-3. GQD, graphene quantum dot; PL, photoluminescence; UV, ultraviolet. Reprinted with permission from Facure *et. al.*[117], Copyright 2022 Elsevier.

The PL spectra of the GQDs obtained using λex at 320 nm are shown in Fig. 3.4(b). It can be observed that the PL intensity is in accordance with the QY values of the GQDs (GQDs-3 > GQDs- 2 > GQDs-1). Moreover, the maximum emission wavelengths (λem) for GQDs-1, GQDs-2, and GQDs-3 are located at 443 nm, 450 nm, and 438 nm, respectively. The best λex (320 nm) is in accordance with other GQDs reported in the literature,[25,67] and the distinct maximum λem is another indication that the chemical structure of the GQDs can be tuned through adjustments in the hydrothermal synthesis parameters.[138]

It has been demonstrated that the optical properties of carbon nanomaterials are highly determined by the partially sp^2-hybridized carbon domains of their sp^3-hybridized amorphous cores.[58,140,141] Therefore, XPS was used to investigate the chemical composition of the different GQDs. As depicted in Fig. 3.5, the C 1s

spectra can be decomposed into three peaks, i.e. C=C/C-C, C-O, and C=O.[117,142,143] As shown in Table A3, the results reveal that the GQDs presented distinct peaks intensities, suggesting different degrees of surface oxidation. Since XPS analysis does not give information about specific oxygen functionalities, FTIR and TGA characterizations were further performed to obtain more information about the composition of each of the synthesized GQDs.
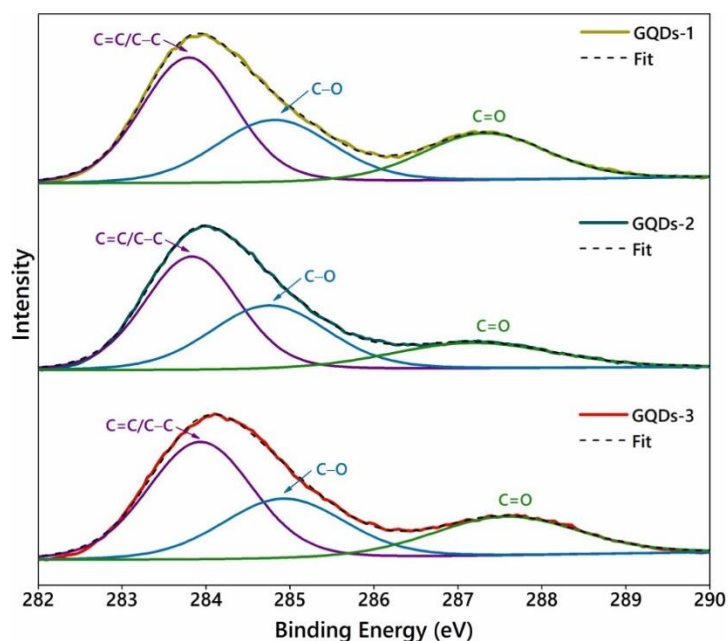
FIGURE 3.5: C 1s XPS spectra of GQDs-1, GQDs-2, and GQDs-3. GQD, graphene quantum dot; XPS, X-ray photoelectron spectroscopy. Reprinted with permission from Facure *et. al.*[117], Copyright 2022 Elsevier.

FTIR spectroscopy was used to further investigate the composition of the GQDs and get more information about the oxygen functionalities present in their structure. As shown in Fig. 3.6(a), all the GQDs spectra presented a peak at 1582 cm^{-1} assigned to the C=C bonds in the GQDs graphitic core. The other peaks are related to the functional oxygenated groups on their surface.[144,145] Compared to the GO spectrum (Fig. A2), it can be noticed that the peaks related to the C=O bonds (1665 cm^{-1}) and the C-O-C of the epoxy groups (1000 cm^{-1}) sharply decreased in intensity, indicating low amounts of carbonyl and epoxy groups in the GQDs structure.[29,145] This is in accordance with Pan et al.,[25] who proposed that the hydrothermal cutting mechanism of the GO is associated with the epoxy and carbonyl groups. Moreover, the decrease in the amount of the epoxy groups can favor the blue luminescence of GQDs because when such groups are present, they contribute to non-radioactive

emissions, decreasing the QY of the materials.[65] The other peaks are related to the angular O-H bonds deformation (1427 cm⁻¹), the axial deformation of the C-O bond of the carboxylic acid groups (1335 cm⁻¹), and the axial deformation of the C-O bonds in aromatic carbons (1100 cm⁻¹).[127,146]
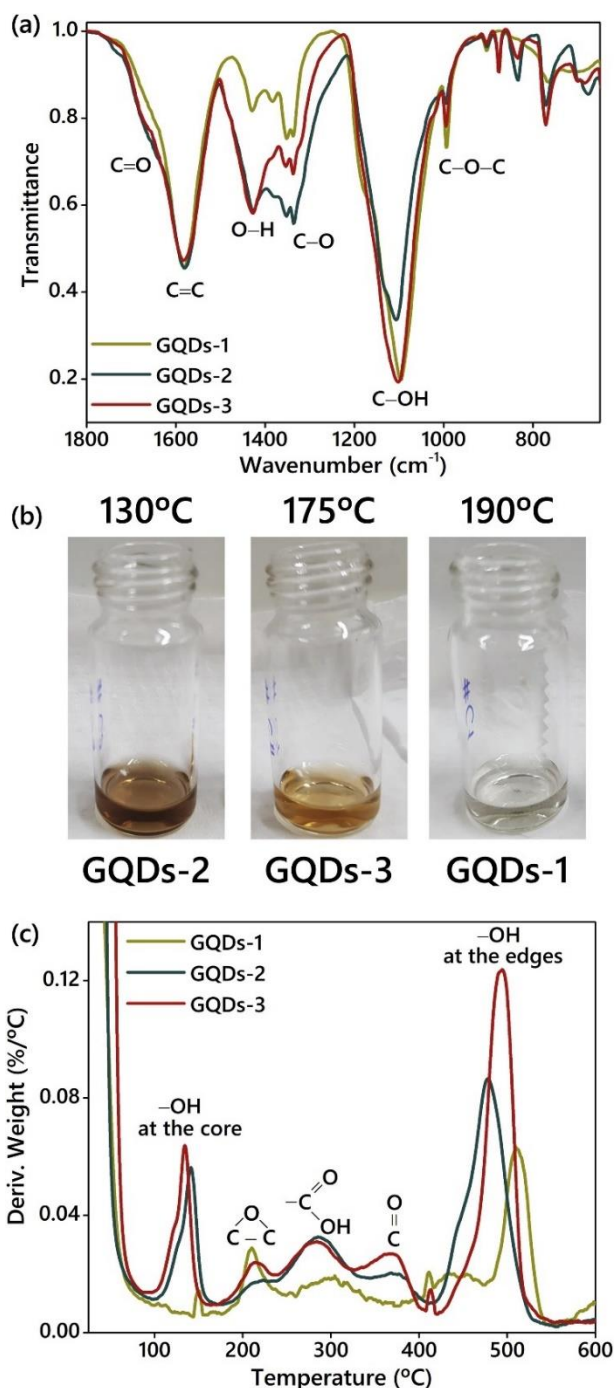
FIGURE 3.6: (a) FTIR spectra of GQDs-1, GQDs-2, and GQDs-3, (b) digital images showing the influence of the temperature used in the hydrothermal synthesis in the GQDs color, and (c) DTG curves of GQDs-1, GQDs-2, and GQDs-3. DTG, derivative thermogravimetric; GQD, graphene quantum dot; FTIR, Fourier transform infrared. Reprinted with permission from Facure *et. al.*[117], Copyright 2022 Elsevier.

The peaks at 1427 cm^{-1} presented the same intensity for GQDs- 2 and GQDs-3, while for GQDs-1, this peak showed to be less intense. These results can be attributed to the -OH groups in the core of the GQDs obtained through the ring-opening of the epoxy groups at pH > 7.[147–149] Because GQDs-2 and GQDs-3 were synthesized using basic pH, they presented more -OH groups in the core of the GQDs, compared to GQDs-1, that were obtained at pH 4.5. This peak is also related to the reminiscent -OH groups of the GO.[145,150] The intensity of the peaks at 1335 cm^{-1} indicates that the GQDs-2 have the highest amount of -COOH. As will be discussed further, this can be attributed mainly to the higher pH (9.5) used in the synthesis. The peak at 1100 cm^{-1} can be related to the -OH groups at the edge of the GQDs.[145,150] The fact that the GQDs-1 and GQDs-3 presented more -OH at the edges than GQDs-2 can be attributed to the superior quantity of -COOH groups in GQDs-2. It is well known that carboxylic groups in GO are located at the edges.[147,151] Therefore, since GQDs-2 have a greater amount of -COOH, they also presented a lower amount of -OH at their edges.

In this way, the QY of GQDs can be attributed to both T and pH. The lowest QY of GQDs-1 is related to the acidic pH used in the synthesis that did not induce the formation of -OH groups at the GQDs' core. As hydroxyl groups contribute to radioactive blue PL emissions,[56,65] the acid pH led to a low QY. Moreover, the higher T (190 ºC) favored the removal of some oxygen groups important to the fluorescent behavior of GQDs-1, as can be observed in the peak at 1335 cm^{-1}, also impairing the QY obtained. The slightly inferior QY of GQDs-2 compared to GQDs-3 can be ascribed by the functional groups present at the edges of the materials. Both presented -OH functionalities at the core, however, GQDs-2 edges contain more -COOH groups that contribute to green emission, leading to a decrease in the QY of GQDs with blue emission.[56] The GQDs-3, in turn, possess more -OH groups at the edges, contributing more to a blue PL and a higher QY. As the syntheses of GQDs-2 and GQDs-3 were performed with different pH and T, the PL responses can be associated with both parameters. To clearly observe the influence of each of these variables on the QY of GQDs, the FTIR characterizations were also performed using GQDs synthesized keeping all parameters fixed and varying only the T or only the pH.

Fig. A3(a) shows the FTIR spectra obtained from GQDs synthesized varying only the pH and maintaining T = 175 ºC. It is possible to observe that acidic pHs do not produce GQDs with many functional groups because the spectrum of the synthesis performed at pH = 4.5 presented low-intensity peaks related to the oxygen

functionalities. On the other hand, syntheses with high pHs seem to favor the presence of -COOH (1335 cm^{-1}) instead of the formation of -OH groups. As can be seen from the QY values obtained, the smaller amount of -OH in the GQDs prepared at higher pH presented a lower QY value (5.9%) than the GQDs produced at acidic pH (6.7%). Furthermore, very high pH values can favor the collapse of GO sheets in solution and consequently induce GO aggregation,[152] hampering the formation of GQDs. Thus, there is an optimal pH value for the syntheses of GQDs that mainly favors the formation of -OH groups and leads to higher QY. As shown in the previous section, this optimum pH is 8.0, i.e. a basic pH that favors epoxy ring-opening and the formation of -OH groups but not excessively high to avoid GO aggregation and allow the GQDs production.

The FTIR spectra obtained from the synthesized GQDs varying the T at pH = 8, shown in Fig. A3(b), reveal that this parameter is crucial for the resulting amount of hydroxyl groups (1427 cm^{-1} and 1100 cm^{-1}) in GQDs. The peak related to the -COOH (1335 cm^{-1}) presented small intensity variations, possibly because all syntheses were carried out at the same pH. It is possible to observe that -OH groups in GQDs are favored at specific temperatures. Low T may not be sufficient for the formation of GQDs functionalized with such groups, as the GO cutting into GQDs can be impaired by the insufficient energy supplied to the system. Thus, the structure of GQDs obtained at low T tends to be more similar to the structure of the GO. This can be corroborated by the color of the GQDs synthesized at 130 ℃, which yields a brownish solution (Fig. 3.6(b)), resembling the color of the GO solution. At the other extreme, high T promotes the removal of -OH groups. For higher T, GQDs solution becomes more transparent (Fig. 3.6(b)), indicating the removal of the oxygen functional groups. In this sense, there seems to be a trade-off about the increase in T. Specifically, on one hand, a higher T seems to favor the cutting of the GO, attacking the defects in the layers and favoring -OH and -COOH groups on the edges of the GQDs.[149,150] On the other hand, too high temperatures lead to the removal of the oxygen functional groups, including the -OH groups at the core, which have an important contribution to a blue emission. The FTIR analyzes corroborate the results obtained in the factorial designs, which showed optimum pH and T parameters.

TGA was used to better understand the structures of GQDs and evaluate the presence and proportion of each of the oxygen functional groups. In the TGA curves (Fig. A4), it is possible to observe that the thermal degradation behavior of all

GQDs presented a similar behavior. The weight loss before 100 ºC is related to the desorption of water from the material. For higher temperatures, the oxygen functional groups are gradually removed from the graphite structure of the GQDs, and the graphite structure is decomposed at temperatures above 800 ºC.[141,153] To better analyze the evolution of the oxygen functionalities in the GQDs, the derivative thermogravimetric (DTG) curves were obtained, as shown in Fig. 3.6(c). The first peak, located between 100 and 170 ºC, is related to the -OH groups present in the GQDs core, which are less stable. The next peak, located between 170 and 250 ºC, is related to the epoxy groups, also in the core of the GQDs.[153,154] The GQDs-1 presented the least amount of in-plane -OH groups and the greatest amount of epoxy groups. This is related to the pH used in the synthesis and the epoxy ring-opening,[148] as discussed in the FTIR analyses. Conversely, a higher amount of in-plane -OH groups and fewer epoxy groups can be observed in the DTG curves for the syntheses at basic pH (GQDs-2 and GQDs-3). The peak between 250 and 325 ºC is related to carboxylic groups, while the peak between 325 and 400 ºC is related to C=O groups.[153,154] As can be noted, the GQDs-1 presented a smaller amount of these oxygen functionalities, while the GQDs-2 sample presented the highest amount of -COOH groups, in accordance with the FTIR analyses. Finally, the peak between 450 and 550 ºC is related to the -OH groups located at the edges of the GQDs. These groups are more stable and therefore need higher temperatures to decompose.[145,153,154] Once again, the results are in agreement with those obtained through FTIR analyses, in which the samples presented higher amounts of -OH groups as follows: GQDs-3 > GQDs-2 > GQDs-1. Thus, the TGA and DTG analyses allowed the identification of the main difference between the GQDs-2 and GQDs-3, namely the amount of -OH and -COOH groups at the edges of the materials.

Although there is a relationship between the GQDs sizes and the types of edges with the PL behavior of the material[29,58,65] (which means that the oxygen functionalities are not solely responsible for such behavior), the PL λem for the -OH and -COOH groups were fixed as an approach to evaluate the contribution of these groups for the GQDs luminescence. The -OH groups contribute to blue emission, while -COOH groups contribute to green emission.[56,64,65] Thus, the PL spectra of the synthesized GQDs were deconvoluted into two peaks, fixing the λem at 435 nm, relative to the luminescent response of -OH, and at 462 nm, related to the response of the -COOH groups. As can be noticed in Fig. 3.7, GQDs-2 present a higher maximum

λem (450 nm) in the PL response (77.4%) because of a greater contribution from the large number of -COOH groups. GQDs-3, which have the highest QY value, have a greater contribution from the -OH (59.1%), leading to the lowest value of maximum *λem*. However, it is important to note that both functional groups are important for GQDs luminescence.
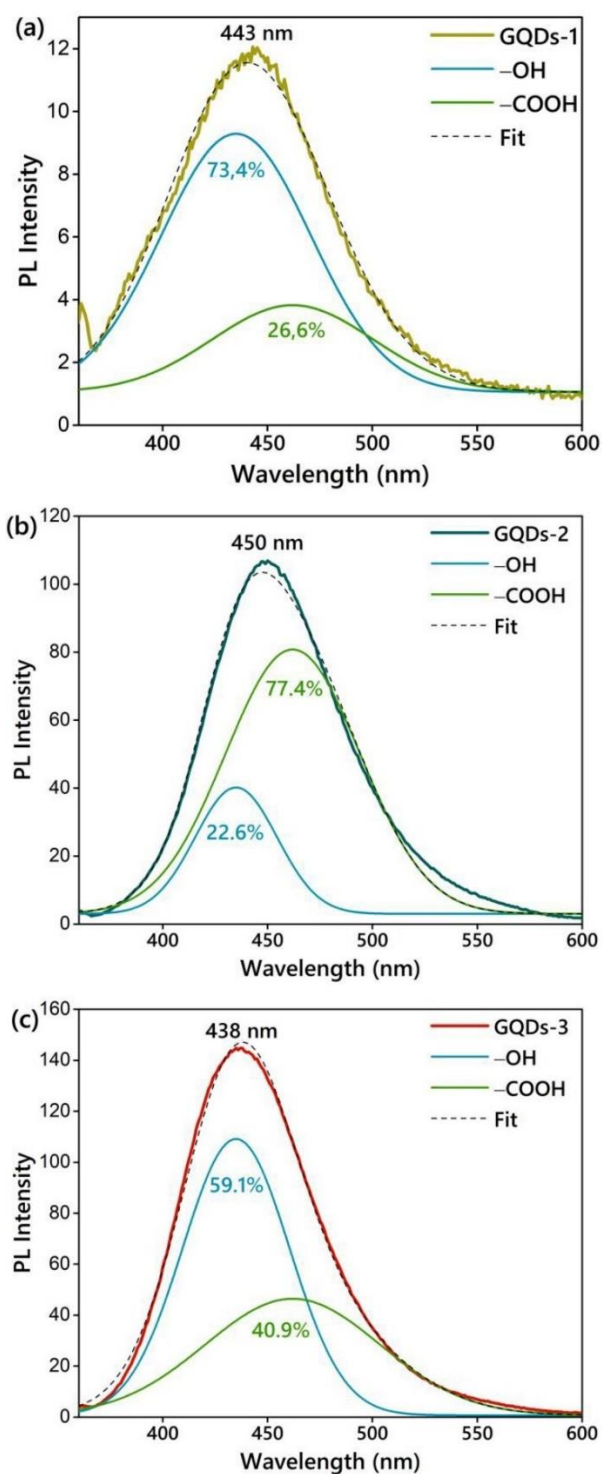
FIGURE 3.7: Deconvoluted PL spectra of (a) GQDs-1 (b) GQDs-2, and (c) GQDs-3 using two peaks centered at 435 and 462 nm related to the -OH and -COOH groups,

respectively. GQD, graphene quantum dot; PL, photoluminescence. Reprinted with permission from Facure *et. al.*[117], Copyright 2022 Elsevier.

In this way, the characterizations performed in this work enabled the evaluation of how the composition of GQDs and their most important functional groups contribute to their luminescent behavior. For instance, the -OH group contributes to a higher QY as their emissions are at the blue region, while the -COOH groups are also important for luminescence, but their emission occurs at longer λ, which can lead to a decrease in the QY value.

3.4.3. Fe^{3+} detection

After getting knowledge on the GQDs structures, the materials were explored as fluorescent probes to optically detect Fe^{3+}. First, the pH that yields the highest PL intensity for each GQDs sample was studied. As can be observed in Fig. A5, the best pH value for GQDs-1 and GQDs-3 is 8.0, while for GQDs-2 is 6.0. These results indicate that the protonation of GQDs plays an important role in fluorescence intensity. The variation in GQDs fluorescence intensity may be attributed to the protonation and deprotonation of oxygen functional groups on the GQD surface, which change their electron distribution. The lower optimum pH value for GQDs-2 can be explained in terms of the higher amount of carboxylic groups in this material since pKa for carboxylic groups is smaller than the pKa for hydroxyl groups.[155,156]

Then, GQDs were used to detect Fe^{3+} through PL quenching experiments. Fig. 3.8(a, c, and e) show the PL spectra of GQDs-1, GQDs-2, and GQDs-3, respectively, after successive additions of Fe^{3+}. The limit of detection (LOD) was defined as 3 σ/S, where σ is the standard deviation of the quenching obtained for the lowest concentration of Fe^{3+} added to the solution, and S is the slope of the calibration curve.[157,158] Fig. 3.8(b, d, and f) show the PL quenching (I/I_0) vs. the concentration of Fe^{3+} for GQDs-1, GQDs-2, and GQDs-3, respectively. The LOD and the linear range obtained for each GQDs sample are presented in Table 3.4. All the LOD obtained are lower than the maximum contaminant level allowed by the U.S. Environmental Protection Agency for Fe^{3+} in drinking water (5.37 μM).[159] Interestingly, the best LOD was obtained for GQDs-2, which is ten times lower than that for GQDs-3. Although hydroxyl groups also participate in the Fe^{3+} detection mechanism, the better performance can be attributed to the elevated number of carboxylic acid groups

in GQDs-2. The binding of Fe^{3+} ions to GQDs can be considered from the viewpoint of the Pearson acid-base concept (hard-soft acid-base theory).[160,161] The higher amount of carboxylate groups of GQDs offers hard binding sites to form complexes with hard Fe^{3+} metal ions. Because electron transfer is known to be an important pathway to quench the fluorescence of GQDs probes,[162,163] the high affinity of Fe^{3+} to carboxyl groups leads to a stronger quenching effect and thus to a lower LOD. The performance of the GQDs-2 for Fe^{3+} detection was found to be superior to other reported GQDs probes, as shown in Table 3.5, indicating its suitability as probes for optical sensors.
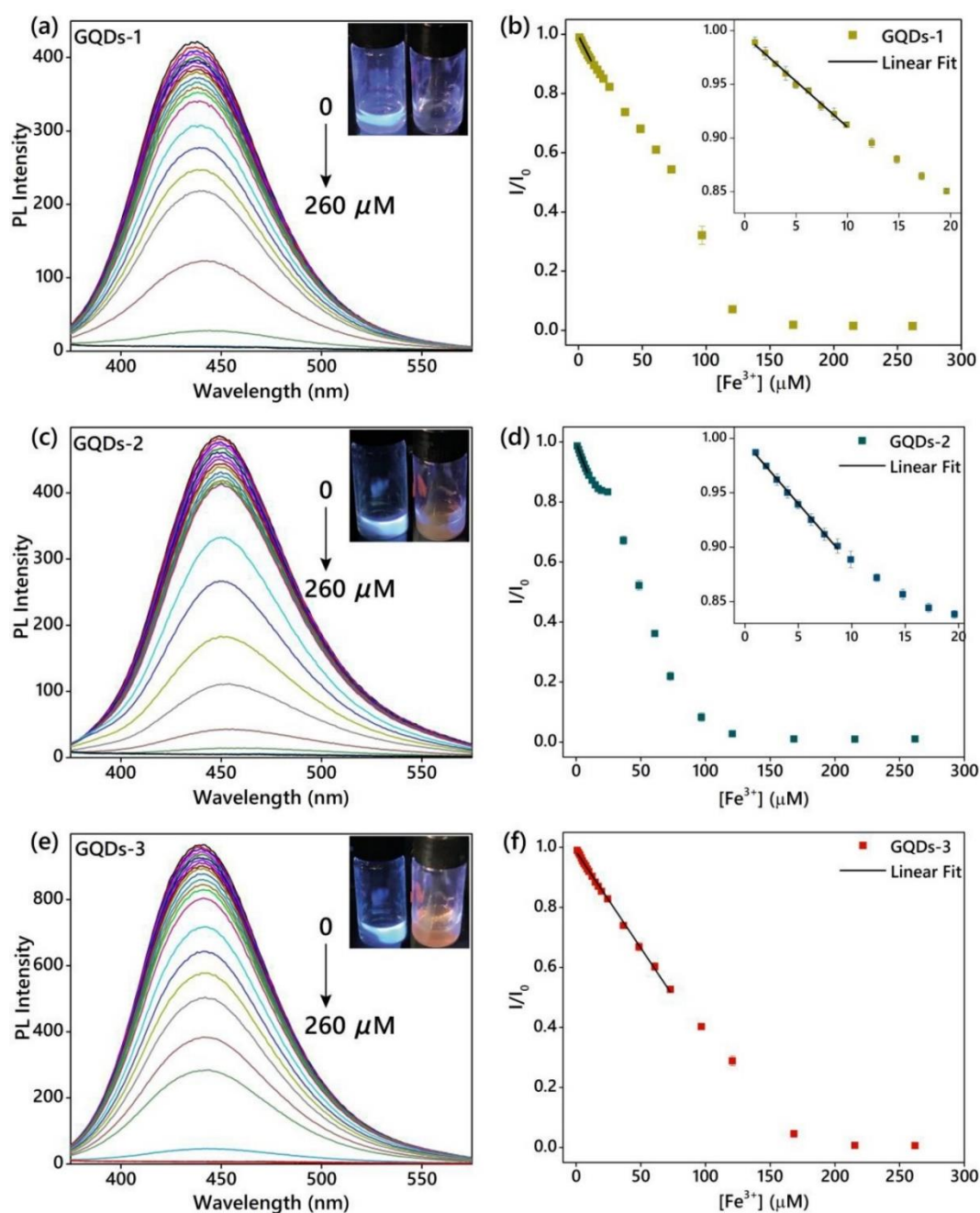
FIGURE 3.8: PL spectra showing the quenching of (a) GQDs-1, (c) GQDs-2, and (e) GQDs-3 upon Fe^{3+} detection. The insets show the images of the GQDs excited by a

320 nm laser before (left image) and after Fe^{3+} addition (right image). PL quenching responses (I/I_0) vs. the Fe^{3+} concentration using (b) GQDs-1, (d) GQDs-2, and (f) GQDs-3 as detection probes. The insets show the linear regression curves used in the limit of detection (LOD) calculation. GQD, graphene quantum dot; PL, photoluminescence. Reprinted with permission from Facure *et. al.*[117], Copyright 2022 Elsevier.

TABLE 3.4: Values of limit of detection and the linear range for Fe^{3+} detection for the samples GQDs-1, GQDs-2, and GQDs-3.

	GQDs-1	GQDs-2	GQDs-3
Limit of Detection (μM Fe^{3+})	1.72	0.136	1.36
Linear Range (μM Fe^{3+})	1 – 10	1 – 8.75	1 – 75

TABLE 3.5: Comparison of the Fe^{3+} sensing performance of other works using GQDs.

GQDs	Detection limit (μM)	Ref.
GQDs	10	164
GQDs	7.22	165
GQDs	0.45	166
N-GQDs	0.09	167
S-GQDs	0.0042	168
GQDs-2	0.136	This work

Although the lowest LOD was observed for the GQDs-2, a wider linear range was obtained for the GQDs-3 sample, which can be related to its higher QY. For example, after the addition of 250 nmol of Fe^{3+}, the quenching of the PL intensity for GQDs-3 was found to be of ca. 70%, while for GQDs-1 and GQDs-2 it was over 90%. The higher PL intensity of GQDs-3 enabled the acquisition of a wider linear range and reliable measurements using higher amounts of Fe^{3+}. In this sense, the control and understanding of the parameters used in the hydrothermal synthesis and the tailoring of the GQDs structure are of paramount importance for specific applications. In this case, if the purpose is to detect the lowest amount of Fe^{3+} in aqueous solutions, GQDs-2 may be more suitable because of the lower LOD and the higher affinity between Fe^{3+} and the carboxylic functional groups. On the other hand, if the goal is to detect samples containing Fe^{3+} at elevated concentrations, the QY of GQDs-2 may not be appropriate, and therefore, GQDs-3 will be the most suitable material for this purpose.

The selectivity of GQDs-2 and GQDs-3 was tested against several other metal ions, as shown in Fig. 3.9. The GQDs were found to be highly selective for Fe^{3+}, even when a mix of metal ions was used as potential interferents. This selectivity was corroborated by other reports using GQDs as probes.[165,166,169] The high selectivity of GQDs toward Fe^{3+} may be associated with the greater metal-ligand formation constants of Fe^{3+} with ligands containing carboxyl groups at neutral and basic pHs. In this way, GQDs presented the highest affinity and a higher chelating speed of Fe^{3+} than other metal ions. Such behavior was also reported in other works.[170–172] Therefore, a coordinated Fe/GQD complex may be formed, which will promote charge transfer and inhibit exciton recombination,[163,173] thus leading to PL quenching behavior.
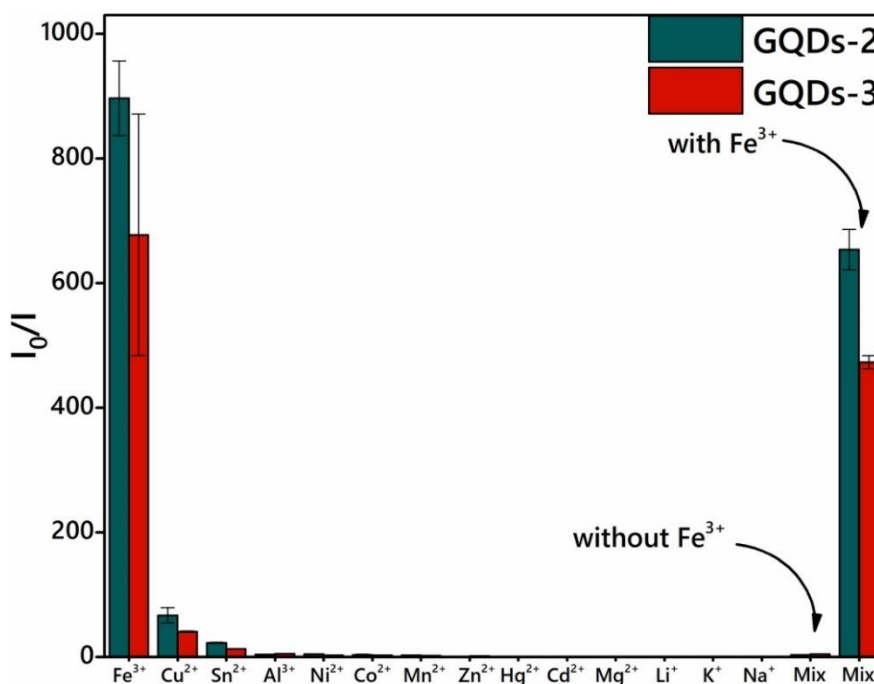
FIGURE 3.9: PL intensity ratio (I_0/I) of GQDs-2 and GQDs-3 for various metal ions and mixes of metal ions with and without Fe^{3+}. GQD, graphene quantum dot; PL, photoluminescence. Reprinted with permission from Facure *et. al.*[117], Copyright 2022 Elsevier.

Therefore, by controlling the synthesis parameters, GQDs with specific characteristics can be produced and used as sensitive and selective probes for Fe^{3+} detection at distinct concentrations ranges. Furthermore, the tailoring of the GQDs structure can also be important for other applications. For instance, the performance of GQDs as enzyme mimicking has been shown to be related to the oxygen functional groups.[174] Specifically, the carboxylic groups act as binding sites, and the -C=O groups

are the active sites for decomposing H_2O_2 and generating $\bullet OH$ radicals, while the -OH groups decrease the catalytic activity of the GQDs.

3.5. Conclusions

In this study, the hydrothermal synthesis' parameters to produce GQDs with enhanced QY values were optimized using factorial design experiments. The results indicated optimum values for C_{GO} (2 mg/mL), T (175 °C), and pH (8.0), which resulted in GQDs with QY of 8.9%. The syntheses did not use any precursor pre-treatment steps or cutting reagents. The highest QY obtained is comparable or even superior to other reported GQDs synthesized by more laborious hydrothermal synthesis. The parameters used showed a significant influence on the GQDs composition. The QY and the luminescent properties of the materials could be adjusted by changing the amount of oxygen functionalities present in the GQDs, favoring the production of GQDs with more hydroxyl or carboxyl groups at their edges. To illustrate the potential applications, GQDs with distinct compositions were used as optical probes for selective Fe^{3+} detection. The performance of the various synthesized GQDs was found to be associated with the functional groups present in the material. A lower LOD of 0.136 μM was obtained for the GQDs with a majority of carboxylic groups (GQDs-2), while a wider linear range was observed for the GQDs with higher QY (GQDs-3). In this way, the role of each synthesis' parameter and its influence on the GQDs compositions can be used to enhance the QY and tailor the GQDs properties for varied applications using simpler and optimized chemical routes.

4.   Chapter II: Expanded voltage window of MXene/Nanodiamonds supercapacitors in AlCl₃ electrolyte*

*The content of this chapter is an adaptation of the article entitled: "**Pillaring effect of nanodiamonds and expanded voltage window of Ti₃C₂T_x supercapacitors in AlCl₃ electrolyte**" by M. H. M. Facure, K. Matthews, R. Wang, R. W. Lord, D. S. Correa, and Y. Gogotsi, published in Energy Storage Materials.

Reference: Energy Storage Materials 61 (2023) 102919.[175]

4.1. Abstract

MXenes have demonstrated excellent performance as constituent materials for supercapacitor electrodes. One of the most outstanding achievements is the capacitance obtained with 2D $Ti_3C_2T_x$ in H_2SO_4 electrolyte, which is related to the O/OH titanium surface termination redox process. However, the narrow (under 1 V) potential window of highly acidic electrolytes is a limiting feature for many applications. In this scenario, materials and electrolytes that produce high capacitance and large potential windows are highly sought after. Herein, we used nanodiamonds (NDs) to pillar the $Ti_3C_2T_x$ structure and obtain superior capacitive storage in $AlCl_3$ electrolytes. The pillaring effect prevents the restacking of MXene layers, reducing diffusion limitations and resulting in a high-rate performance with a capacitance of 235 F/g (561 F/cm^3). The use of 3 M $AlCl_3$ provided protons that contributed to the capacitance obtained and allowed an expansion of the potential window to 1.2 V, due to the lowered activity of water in the electrolyte. The results reflect the need for a proper combination of electrode architecture and electrolyte formulation while providing a direction for the exploration of more efficient, safe, and inexpensive supercapacitor devices.

4.2. Introduction

Among the many potential applications of MXenes,[89] energy storage has aroused the most interest due to MXenes' 2D morphology and attractive properties, such as high electrical conductivity and a large redox-active surface.[107,112,176,177] On the cell level, the performance of MXenes in energy storage applications depends on the electrode architecture, surface chemistry, and electrolyte.[103] Specifically for their use as supercapacitor electrodes, the highest capacitance values were reported using $Ti_3C_2T_x$ (T_x represents surface terminations such as O, OH, and F) in H_2SO_4 electrolyte. Such high performance is mainly attributed to the surface redox process caused by the intercalation of protons between $Ti_3C_2T_x$ layers and the protonation/deprotonation of the MXene. The intercalated protons react with the O terminations of MXene and form OH groups, thus changing the Ti oxidation state, which results in the pseudocapacitive behavior.[103–105]

To obtain better performance, regarding not only capacitive values but also higher energy densities at fast rates, an appropriate MXene interlayer distance is

key to decreasing diffusion limitations and improving the accessibility of ions. In this regard, spacer materials have been proposed as pillars between the layers, leading to improved performances.[105,108] In addition to reducing diffusion limitations by creating fast ion transport pathways, spacers also prevent the usual and undesirable restacking of the $Ti_3C_2T_x$ layers.[105,108] Among many alternatives that can be used as pillars between MXene layers, carbon nanomaterials have shown to be a promising strategy. For instance, carbon nanotubes,[111,178] graphene-based materials[179,180] and carbon dots[110] have been employed to prevent the self-restacking of MXene sheets. Moreover, the synergistic effect obtained by combining MXenes and carbon materials can result in better performance due to the large surface area, high conductivity, and chemical stability characteristic of the composites produced.[181,182]

Given the potential of these hybrid structures, the performance of new combinations of MXenes with carbon nanomaterials not yet explored for use in energy devices should be investigated. Specifically, the use of 0D nanoparticles is particularly interesting due to its morphology and size. While 1D and 2D carbon materials may present difficulties to be inserted between MXene layers, 0D particles can act as pillars between the layers and occupy a smaller active area on the MXene compared to their high-dimensional counterparts. In this scenario, the combination of MXenes with nanodiamonds (NDs) has not yet been explored in supercapacitor electrodes. NDs are 0D particles with an sp^3 diamond core that may be partially covered by graphitic or amorphous carbon[183,184] and can give rise to improved capacitive energy storage when combined with MXene. Unlike nanotubes or graphene, NDs are hydrophilic, have =O and -OH terminations,[183] and can be easily mixed with MXenes in aqueous solutions, not requiring the use of surfactants.

Although high capacitance values have been obtained with $Ti_3C_2T_x$ in H_2SO_4, only relatively narrow potential windows (usually less than 1 V) have been achieved with this electrolyte.[105,112,113] Wider voltage windows are crucial for obtaining supercapacitors with superior energy densities (E), since it is proportional to the square of the voltage (V), according to the formula for a double-layer capacitor:

$$E = \frac{CV^2}{2},$$ (Eq. 4.1)

in which C is the capacitance.[114,185] An alternative to expanding the working potential window is the use of highly concentrated electrolytes. For instance, water-in-salt (WIS) electrolytes have been shown to suppress oxygen and hydrogen evolution and

$Ti_3C_2T_x$ oxidation. Such behavior is attributed to the lesser amount of free water at the electrode's surface and its reduced activity, which hinders the electrode's degradation and the electrolyte's decomposition, leading to a wider potential window.[93,116] However, the use of WIS electrolytes with MXenes generally produces moderate capacitance values.[93,115] Therefore, an electrolyte capable of yielding a wider stable potential window and high capacitance is highly desirable.

MXenes have been mainly explored in electrochemical systems using monovalent cations, but there are still limited studies using aqueous multivalent cation electrolytes.[186,187] The multivalent cation electrolytes can lead to higher capacitance and energy density values.[188,189] Furthermore, some multivalent ions, such as Zn^{2+} and Al^{3+}, have a strong Lewis acidic character, providing protons to water, which is beneficial for obtaining higher capacitance values with $Ti_3C_2T_x$ electrodes, as earlier mentioned. However, using electrolytes containing Zn^{2+} can limit the voltage window since metal plating occurs under relatively high negative potentials.[190] Therefore, among different multivalent cations, Al^{3+}-containing electrolytes represent an interesting alternative not yet fully explored with MXenes. Being an abundant metal, using aluminum in electrolytes can reduce the device fabrication cost while improving safety and performance.[191,192]

In this work, we combined for the first time $Ti_3C_2T_x$ and NDs to be used in an electrochemical supercapacitor. The use of NDs as pillaring particles avoided $Ti_3C_2T_x$ layer restacking and reduced diffusion limitations. In addition, the current collector-free MXene/ND 2D/0D hybrid electrode allowed the use of electrolytes containing corrosive Cl^- anions due to the chemical stability of $Ti_3C_2T_x$ and NDs in chloride solutions. The hybrid material was tested using different multivalent cation electrolytes ($CaCl_2$, $MgCl_2$, $ZnCl_2$, and $AlCl_3$) and the best capacitance values were obtained in 3 M $AlCl_3$. The superior performance relies on the combination of electrolyte formulation and electrode architecture design. The high capacitance values obtained were ascribed to the presence of protons in the $AlCl_3$ solution. Furthermore, unlike H_2SO_4 and HCl aqueous electrolytes, the $AlCl_3$ concentration can be tailored to produce quasi-saturated solutions that enable operation in a larger potential window.

4.3. Materials and methods

4.3.1. Chemicals

The Ti_3AlC_2 MAX phase was obtained from Carbon-Ukraine, Ltd. Hydrofluoric acid (HF, 48.5–51%, Acros Organics), hydrochloric acid (HCl, 36.5–38%, Fisher Scientific), and lithium chloride (LiCl, 99%, Acros Organics) were used in the synthesis and delamination of the MXene. Sulfuric acid (H_2SO_4, 98%), calcium chloride ($CaCl_2$, anhydrous, ≥97%), magnesium chloride ($MgCl_2$, anhydrous, ≥ 98%), zinc chloride ($ZnCl_2$, ≥ 98%), and aluminum chloride hexahydrate ($AlCl_3 \cdot 6H_2O$, 99%) were obtained from Sigma-Aldrich and used to prepare the electrolyte solutions. Commercial nanodiamonds (NanoBlox, Inc.) with a particle size of ~4 – 5 nm, obtained by detonation synthesis and acid purification, were used in this study. All the chemicals were used as received.

4.3.2. $Ti_3C_2T_x$ MXene synthesis

The $Ti_3C_2T_x$ synthesis was adapted from the procedure described elsewhere.[101] Briefly, 1 g of MAX phase was added into a solution containing 12 mL of HCl, 6 mL of DI water, and 2 mL of HF. The resulting mixture was stirred for 24 h at 35 °C and 300 rpm. Then, the multilayered MXene was washed through successive centrifugation cycles until the pH reached a value ≥ 6. The obtained multilayer MXene slurry was then dispersed in 50 mL of a 0.5 M LiCl solution. After stirring the mixture for 24 h at 35 °C, centrifugation cycles (3500 rpm for 5 min) were performed to remove the excess of LiCl. The transparent supernatant was discarded until the solution started to present a black color, indicating the presence of delaminated $Ti_3C_2T_x$, which was then collected. The collected $Ti_3C_2T_x$ solution was concentrated through centrifugation at 10,000 rpm for 10 min. Before obtaining the films through filtration, the $Ti_3C_2T_x$ solution (2 mg/mL) was probe-sonicated (Fisher FB505) at 250 W and 50% amplitude for 10 min.

4.3.3. Supercapacitor electrodes production

The electrodes used in the electrochemical measurements were obtained by vacuum-assisted filtration of the $Ti_3C_2T_x$ and $Ti_3C_2T_x$/NDs dispersions in water (1.5 mg/mL). For the $Ti_3C_2T_x$/NDs films, colloidal dispersions containing 5, 10, and 30% of NDs in relation to the mass of $Ti_3C_2T_x$ (% w/w) were used. They were prepared by mixing the right volume of a 2 mg/mL dispersion of NDs with a 2 mg/mL

dispersion of $Ti_3C_2T_x$ and adjusting the concentration used in the filtration with DI water. The mass of MXene was constant for all the films produced. From now on, the films containing NDs will be referred to as $Ti_3C_2T_x$/NDs-Y%, with Y being the loading of NDs used.

AC counter electrode films were prepared by mixing 95 wt% of YP50F (Kuraray, Japan) with 5 wt% of polytetrafluorethylene. The obtained mixture was dissolved in ethanol and dried overnight. The slurry was then rolled to produce ~100 μm thick films, that were punched to obtain films with diameters of 5 mm.

4.3.4. Physicochemical characterization

Transmission electron microscopy (TEM) and the high-resolution TEM (HR-TEM) images were obtained in a JEOL 2100F microscope operating at 200 kV. The samples were prepared by drop-casting the MXene and the NDs aqueous dispersion onto a lacey carbon-coated, Cu grid. Scanning electron microscopy (SEM) images were obtained using a Zeiss Supra VP50 microscope. Cryo-fracture was performed with liquid N_2 and the fractured films were used to obtain the cross-sectional images.

X-ray powder diffraction (XRD) analyses were performed with the vacuum-filtrated films in a Rigaku SmartLab diffractometer, using a 40 kV/44 mA X-ray source for the 2θ range of 3–70°. X-ray photoelectron spectroscopy (XPS) analysis was performed with the NDs powder in a PHI VersaProbe 5000 instrument (Physical Electronics) using a 100 μm and 25 W monochromatic Al-Kα (1486.6 eV) X-ray source. An Evolution 201 (ThermoScientific) spectrophotometer was used in the UV-vis analysis. The spectrum was collected from 200 to 1000 nm using a quartz cuvette. A Fisher Scientific Model 505 Sonic Dismembrator was used to sonicate the $Ti_3C_2T_x$ solution. The average flake size measurements of the $Ti_3C_2T_x$ were performed in a Malvern Panalytical Zetasizer Nano ZS using a polystyrene cuvette.

4.3.5. Electrochemical characterizations

Swagelok cells were used in all electrochemical experiments. The $Ti_3C_2T_x$ and $Ti_3C_2T_x$/NDs films were used as working electrodes, Ag/AgCl (for the chloride electrolytes) and Hg/Hg_2SO_4 (for H_2SO_4) as the reference electrodes, and activated carbon (AC) as the counter electrode. The working electrodes were prepared by punching discs with diameters of 3 mm from the MXene vacuum-filtrated films. To

calculate the specific and volumetric capacitances, the discs were weighted using a Mettler Toledo UMX2 microbalance and had their thickness measured with a digital micrometer. Unless otherwise stated, all the results were obtained using electrodes of ~1 mg/cm². Glassy carbon electrodes were used as current collectors in the three electrodes cell and Celgard (25 μm thick 3501 polypropylene membrane) was used as the separator between the counter and the working electrodes.

All the electrochemical experiments were performed using a VMP3 potentiostat (BioLogic) at room temperature. The gravimetric specific capacitance (C) was calculated using the anodic peak in the cyclic voltammograms (CVs) using the following equation:

$$C = \frac{\int i \, dt}{m \, V},$$
<div align="right">(Eq. 4.2)</div>

where i is the current measured as a function of time (t), m is the mass of the working electrode used, and V is the voltage window.[93]

The kinetics of the electrode charging was determined by calculating the b value in the equation:

$$i_p = a v^b,$$
<div align="right">(Eq. 4.3)</div>

where a and b are adjustable parameters, i_p is the anodic peak current, and v is the scan rate.[114]

The electrochemical impedance spectroscopy (EIS) measurements were carried out by sweeping the frequency from 500 kHz to 0.1 Hz at an amplitude of 10 mV.

4.4. Results and discussion

4.4.1. Materials characterization

TEM images were used to characterize $Ti_3C_2T_x$ and the NDs. $Ti_3C_2T_x$ flakes with a few micrometers in size are shown in Fig. 4.1a. The flakes are uniform with no apparent defects on their surface and present well-defined edges. The HR-TEM image (Fig. B1a) corroborates with the high-quality MXene synthesized. The selected area electron diffraction (SAED) pattern (Fig. B1b) shows the hexagonal atomic structure. The TEM analyses confirm the success of synthesizing high-quality and crystalline MXene.[193] In Fig. 4.1b we observe an agglomerate of NDs and isolated

NDs particles around it. Fig. 4.1c shows the high-resolution TEM image of a few NDs particles, revealing crystalline diamond cores surrounded by small regions of amorphous carbon.[184,194]
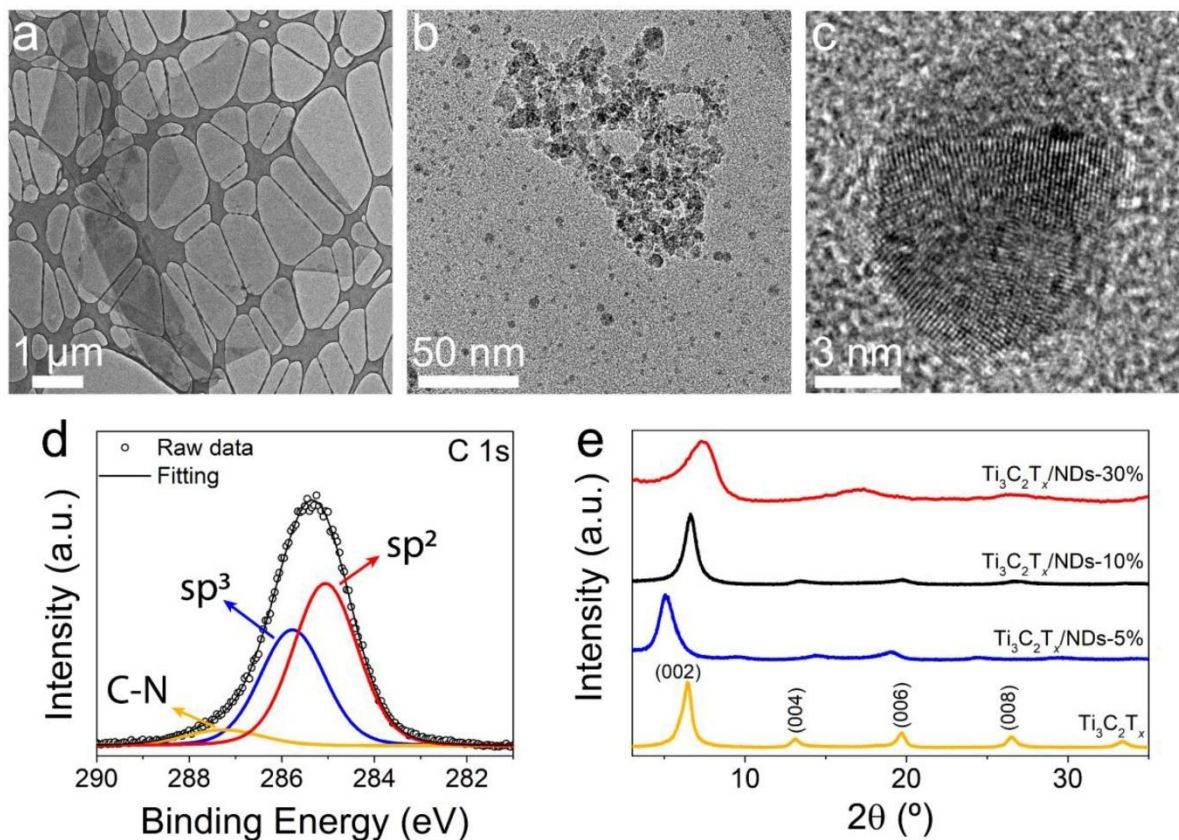
FIGURE 4.1: Transmission electron microscopy (TEM) images of (a) $Ti_3C_2T_x$ and (b) nanodiamonds (NDs). (c) High-resolution TEM image of a few ND particles. (d) C 1s X-ray photoelectron spectroscopy (XPS) spectrum of the NDs. (d) X-ray diffraction (XRD) patterns of the $Ti_3C_2T_x$ and $Ti_3C_2T_x$/NDs hybrid films. Reprinted with permission from Facure *et. al.*[175], Copyright 2023 Elsevier.

The XPS survey spectrum of the NDs (Fig. B2) shows peaks related to the presence of C, O, and N on the NDs' surface. The atomic quantification was estimated to be 87.3% of C, 12% of O, and 0.7% of N. The high-resolution C 1s spectrum (Fig. 4.1d) presents a fitted peak centered at 285.3 eV. The XPS data were fitted by three peaks, centered at 285.0, 285.8, and 287.2 eV. The peaks at 285.0 and 285.8 eV can be respectively ascribed to sp^2- and sp^3-hybridized carbon, while the peak at 287.2 eV is attributed to C–N and defects on the NDs' surface.[195] The first two peaks represent 93.5% of the fitted data (54.7% of sp^2 carbons and 39.0% of sp^3 hybridization) and the peak related to C–N and defects represents only 6.3%.

The XRD pattern of the Ti_3AlC_2 MAX phase used to synthesize the $Ti_3C_2T_x$ is shown in Fig. B3a. After MXene synthesis, many of the MAX phase crystallographic peaks vanish, and the resulting vacuum-filtrated MXene film pattern presents only the (00l) peaks, confirming the synthesis of the $Ti_3C_2T_x$.[196] The UV-vis spectrum of the obtained $Ti_3C_2T_x$ solution (Fig. B4a) shows a plasmonic peak around 770 nm, a peak at 320 nm, and a shoulder centered at 265 nm, also confirming the successful synthesis of the $Ti_3C_2T_x$ MXene.[101] In order to enhance ion accessibility and improve the electrochemical performance of the materials, the size of the $Ti_3C_2T_x$ flakes was reduced using probe-sonication.[113,197] The dynamic light scattering (DLS) technique was used to evaluate the reduction of the MXene flakes' average size. Despite the assumption made by the DLS technique that particles are spherical, which does not hold true for 2D MXene layers,[196] researchers have still utilized DLS to evaluate changes in the MXenes particle size.[198,199] Fig. B4b shows that the average size of the flakes was reduced from 615 to 220 nm after 10 min of sonication.

MXene and NDs dispersions were used to obtain the hybrid films by vacuum filtration. A cross-sectional SEM image and a digital picture of the obtained flexible free-standing $Ti_3C_2T_x$/NDs-10% film are shown in Fig. B5. The cross-sectional image (Fig. B5a) shows the layered structure of the $Ti_3C_2T_x$/NDs-10% film which is similar to the morphology observed in other reported MXene films,[110,186] showing that the incorporation of the NDs did not impair an orderly stacking of MXene flakes during vacuum filtration. XRD was used to further characterize the structure obtained in the vacuum-filtrated films. The XRD patterns in Fig. 4.1e show that the films containing the NDs presented the same profile, with the presence of only (00l) peaks. Incorporating the NDs changed the (002) peak position, width, and intensity (Fig. B3b), which shows that the NDs were successfully intercalated between the MXene layers. In the $Ti_3C_2T_x$/NDs-5% film, the (002) peak is centered at $2\theta = 5.1°$, indicating that the average d-spacing increased from 13.8 Å ($2\theta = 6.4°$ for the $Ti_3C_2T_x$ film) to 17.3 Å. The $Ti_3C_2T_x$/NDs-10% film presented little variation in the position of the (002) peak, compared to the film without NDs, of only 0.2°, while the (002) peak of the $Ti_3C_2T_x$/NDs-30% film is located at $2\theta = 7.4°$. In terms of intensity, only the $Ti_3C_2T_x$/NDs-10% film presented a (002) peak with a higher intensity than the $Ti_3C_2T_x$ film. The lower intensities indicate a fewer number of flakes aligned in the out-of-plane direction.[196] In addition, all the films containing NDs presented broader (002) peaks. The full width at half-maximum (FWHM) values for the $Ti_3C_2T_x$/NDs-5% and $Ti_3C_2T_x$/NDs-30% films

were 1.2° and 3.5°, while the $Ti_3C_2T_x$/NDs-10% presented a closer FWHM value (0.9°) when compared to the film without NDs (0.7°). The broader peaks indicate a wider distribution of the d-spacing.[200] The broader peaks in the films containing 5% of NDs may be ascribed to the lower amount of NDs inserted only between some particles, leading to a nonuniform spacing, while for the $Ti_3C_2T_x$/NDs-30% films, clustering of the NDs and an over-occupation of sites led to a restacking disorder. In contrast, a narrow distribution of the d-spacing was obtained in the sample containing 10% of NDs, showing that this amount is more suitable to provide a regular d-spacing. The XRD results show that the use of 10% NDs loading, despite not significantly altering the d-spacing of MXene, presented a more homogeneous lamellar structure, with greater flake alignment, matching the pristine film.

4.4.2. $Ti_3C_2T_x$/NDs as supercapacitor electrode

To evaluate the performance of the hybrid material as a supercapacitor electrode, different multivalent cation electrolytes were used. The $Ti_3C_2T_x$/NDs-10% electrode was tested in 5 M $CaCl_2$, 3 M $MgCl_2$, 10 m (mol/kg water) $ZnCl_2$, and 3 M $AlCl_3$, besides the standard 5 M LiCl. The multivalent cation electrolytes were prepared in close-to-saturation concentrations to reduce side reactions by lowering the amount of free water at the electrode's surface.

As seen in Fig. 4.2a, the CV profile obtained for $Ti_3C_2T_x$/NDs-10% in 3 M $AlCl_3$ shows cathodic and anodic peaks with little separation in the region from -0.4 to -0.8 V *vs* Ag/AgCl (the potentials in this study were recorded using an Ag/AgCl reference electrode, unless otherwise specified), resembling the CV with signature redox peaks of $Ti_3C_2T_x$ in acidic media.[112,113] Since 3 M $AlCl_3$ gives rise to a very acidic solution (pH < 1), these peaks can be ascribed to the intercalation of H+ between the MXene layers, which leads to surface redox reactions.[104,105] The CV for 10 m $ZnCl_2$ shows smaller anodic peaks between -0.3 and -0.6 V. The smaller peaks observed in the CV for 10 m $ZnCl_2$ can also be ascribed to the presence of protons since the pH of the electrolyte was found to be 1.1. To obtain the full contribution of protons intercalation with $ZnCl_2$, more negative potentials should be tested. However, zinc plating occurs at potentials lower than -0.7 V (Fig. B6a), which limits the exploration of Zn-containing electrolytes in larger potential windows.[190] Rectangular CV shapes, characteristic of double-layer capacitors, were observed in the non-acidic electrolytes (LiCl, $CaCl_2$, and $MgCl_2$ with pH of 5.2, 8.9, and 7.2, respectively), in which

no peaks were observed. Because of protons intercalation and the resulting surface redox process, the highest capacitance was obtained using 3 M AlCl$_3$ (235 F/g and 561 F/cm^3 at 2 mV/s), as shown in Fig. B6b.
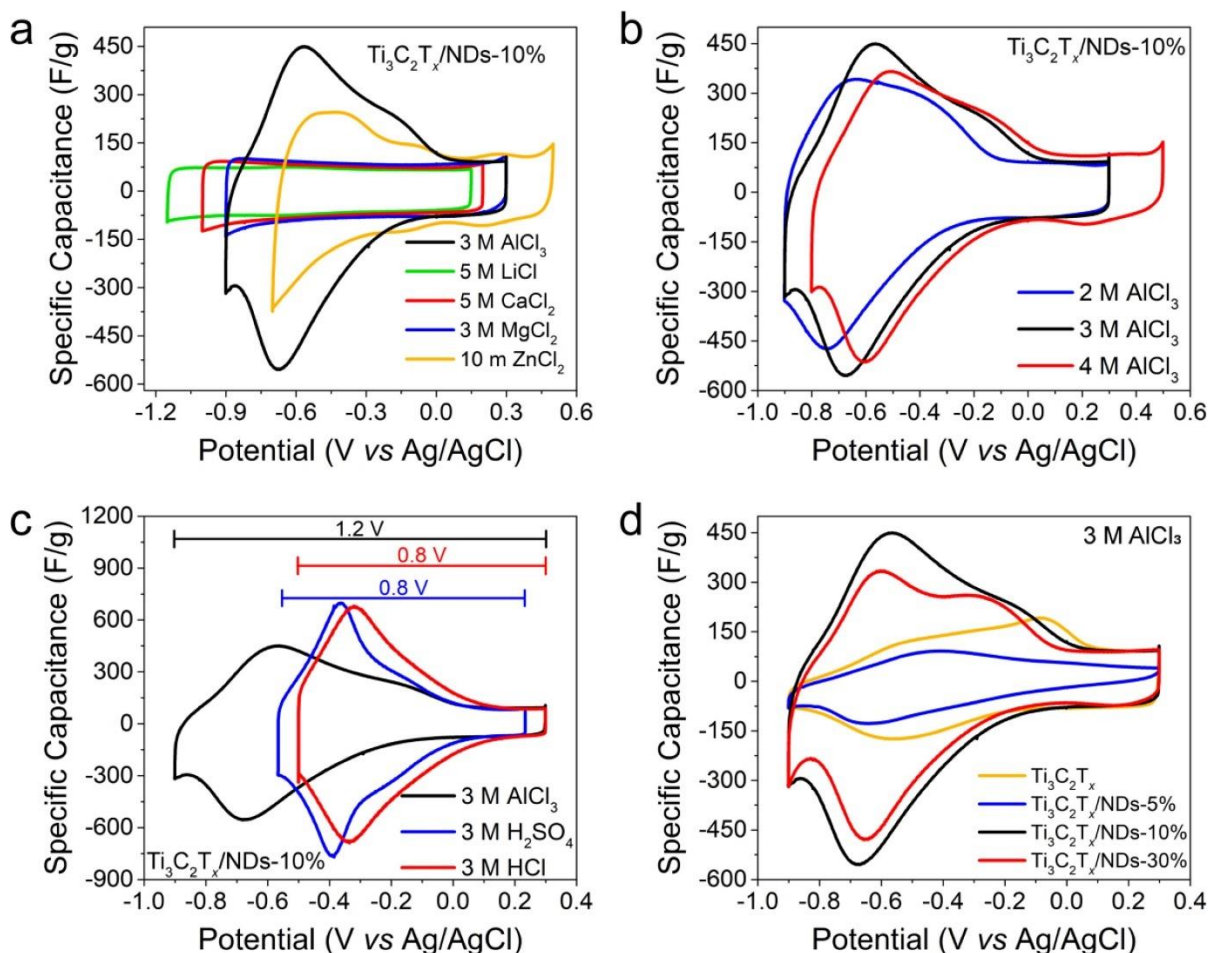
FIGURE 4.2: Electrochemical performance of Ti$_3$C$_2$T$_x$/NDs as a supercapacitor electrode. Cyclic voltammograms (CVs) for Ti$_3$C$_2$T$_x$/NDs-10% in (a) 5 M LiCl, 5 M CaCl$_2$, 3 M MgCl$_2$, 10 m ZnCl$_2$, and 3 M AlCl$_3$, (b) in AlCl$_3$ with different concentrations (2 M, 3 M, and 4 M), (c) in 3 M AlCl$_3$, 3 M HCl, and 3 M H$_2$SO$_4$ (the potentials for H$_2$SO$_4$ were converted from Hg/Hg$_2$SO$_4$ to Ag/AgCl), and (d) for Ti$_3$C$_2$T$_x$ and Ti$_3$C$_2$T$_x$/NDs hybrids with different NDs loadings (5, 10, and 30%). All the CVs were collected at 2 mV/s. Reprinted with permission from Facure *et. al.*[175], Copyright 2023 Elsevier.

The effect of AlCl$_3$ concentration was also investigated using the Ti$_3$C$_2$T$_x$/NDs-10% (Fig. 4.2b). The 2 and 4 M electrolytes presented specific capacitances of 196 and 204 F/g, respectively. We believe that the inferior values obtained are related to the fewer protons in the 2 M AlCl$_3$ and an inferior amount of water available in the 4 M electrolyte compared to the 3 M concentration. Shao et al. demonstrated that confined H$_2$O molecules between Ti$_3$C$_2$T$_x$ layers play a pivotal role in the charging storage mechanism in acidic media.[92] The water molecules help

the formation of a hydrogen bond network that enables fast kinetics by charge compensation through high-rate diffusion of H$^+$ and favoring the Ti redox reactions, which leads to higher capacitance values. Also, the 4 M concentration presents higher viscosity, which hinders the ions' accessibility to the Ti$_3$C$_2$T$_x$ surface. In conclusion, the 3 M electrolyte presents the right tradeoff between protons and water molecules, giving rise to high capacitance values and preventing side reactions, thus enabling the exploration of wider voltage windows.

Since the capacitance obtained using AlCl$_3$ can be attributed to the presence of protons, the Ti$_3$C$_2$T$_x$/NDs-10% electrode was also tested in 3 M HCl and 3 M H$_2$SO$_4$ for comparison. It can be seen from Fig. 4.2c that the peaks related to the H$^+$ intercalation in the acidic electrolytes presented higher intensities when compared to those obtained in 3 M AlCl$_3$. Consequently, the capacitance values obtained in 3 M HCl (311 F/g) and 3 M H$_2$SO$_4$ (301 F/g) were also higher than the capacitance for AlCl$_3$. As discussed above, the water plays a role in increasing the capacitance obtained by providing a hydrogen bond network that leads to enhanced diffusion of protons.[92] Based on that, in comparison with the 3 M AlCl$_3$ electrolyte, the superior capacitance values obtained in HCl and H$_2$SO$_4$ can be mainly ascribed to the higher availability of water molecules in these electrolytes. Other factors can slightly contribute to the enhanced capacitance, such as lower viscosity and high ionic conductivity, but with a much inferior effect than the water availability difference. However, the potential windows obtained for HCl and H$_2$SO$_4$ are only 0.8 V, while the voltage window for 3 M AlCl$_3$ was 1.2 V (from -0.9 to 0.3 V). Exploring a broader potential window in AlCl$_3$ is possible because a close-to-saturation concentration can be obtained, which lowers the activity of water by hindering parasitic side reactions.[93,116] Thus, on one hand, the lower amount of water leads to a slight decrease in the obtained capacitance value, but on the other hand, it gives rise to larger potential windows. Therefore, the use of AlCl$_3$ represents the advantage of using an electrolyte that contains protons, which gives rise to high capacitance values and, at the same time, allows the manipulation of its concentration to obtain larger potential windows, which is important to achieve higher energy densities.

To evaluate the effect of the NDs in the capacitance obtained, CV measurements were performed using the pure Ti$_3$C$_2$T$_x$ and the hybrid films (Fig. 4.2d). The specific capacitance values obtained for Ti$_3$C$_2$T$_x$, Ti$_3$C$_2$T$_x$/NDs-5%, and Ti$_3$C$_2$T$_x$/NDs-30% were 111 F/g, 62 F/g, and 196 F/g at 2 mV/s, respectively.

Therefore, using 10% of NDs increased the capacitance of $Ti_3C_2T_x$ by over 110% in 3 M $AlCl_3$. The performance enhancement can be mainly attributed to the structure obtained with the NDs acting as pillars between MXene layers, which avoided restacking of the layers, reduced diffusion limitations, and improved proton accessibility to the MXene surface.

The capacitance obtained for the hybrids containing 5 and 30% of NDs are smaller than the capacitance obtained for the film containing 10% (235 F/g). The lower capacitance for the film containing 5% of NDs can be related to the insufficient amount of NDs used, which was unable to efficiently act as pillars in the $Ti_3C_2T_x$ structure during electrochemical measurements, as schematically illustrated in Fig. 4.3. Also, since NDs are non-conductive nanomaterials,[183] at high concentrations, their presence decreased the electrical conductivity of the electrode, which hampered its performance and led to a capacitance even lower than that of the pure MXene film. As a consequence, smaller peaks related to the proton intercalation and redox reactions at the MXene surface were observed in the correspondent CV.
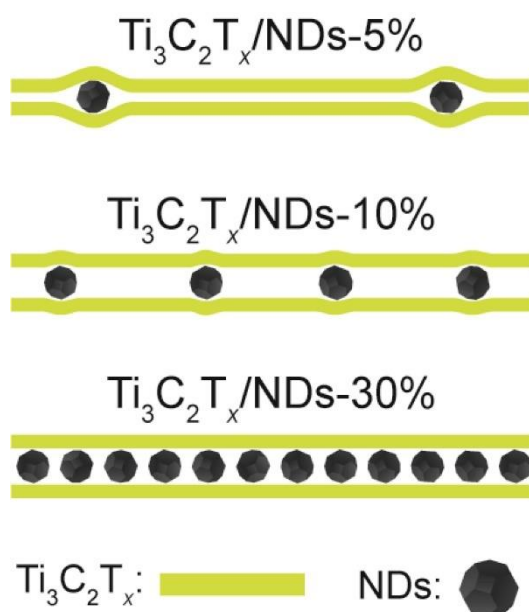
FIGURE 4.3: Schematic illustration of the MXene layers restacking during electrochemical measurements using different amounts of NDs. The amount of NDs used in the $Ti_3C_2T_x$/NDs-10% and $Ti_3C_2T_x$/NDs-30% is sufficient to avoid the restacking of the sheets, which is not the case for $Ti_3C_2T_x$/NDs-5% film. Reprinted with permission from Facure *et. al.*[175], Copyright 2023 Elsevier.

The performance of the $Ti_3C_2T_x$/NDs-30% film was higher than the films containing 5% NDs and the pure MXene film due to the pillaring effect obtained by

using 30% of NDs. However, when compared to the performance obtained with the Ti$_3$C$_2$T$_x$/NDs-10% film, the slightly inferior capacitance obtained with the films containing 30% of NDs can be ascribed to the less electrically conductive structure obtained using more NDs. For instance, the electrical conductivity of the Ti$_3$C$_2$T$_x$ film, ~10,100 S/cm, decreased to ~4700 S/cm and ~2400 S/cm for the films with 10% and 30% NDs, respectively. The CVs for the films containing 10% and 30% of NDs are very similar in shape, presenting defined peaks related to the pseudocapacitive process derived from the H$^+$ intercalation. These results indicate that a similar extension of Ti$_3$C$_2$T$_x$ structure opening is achieved when using 10 and 30% of NDs (as shown in Figs. 4.1e and B3b) and that these amounts are sufficient to avoid the restacking of MXene sheets, as illustrated in Fig. 4.3. In this way, 10% NDs is sufficient to obtain the pillaring effect on the Ti$_3$C$_2$T$_x$ layers and avoid their restacking, while the use of a higher amount led to a decrease in the film's electrical conductivity, which in turn reduced the capacitance value obtained.

Fig. 4.4a shows the CVs obtained with Ti$_3$C$_2$T$_x$/NDs-10% in 3 M AlCl$_3$ at different scan rates, from 2 to 1000 mV/s. With the increase in the scan rate, the peaks become less defined due to the sluggish kinetics at high rates. The chronoamperometry data (Fig. B7) shows that -0.9 V is the maximum negative potential for Ti$_3$C$_2$T$_x$/NDs-10% in 3 M AlCl$_3$, indicating negligible contributions from parasitic reactions in the 1.2 V potential window used.[185] The capacitance comparison of the Ti$_3$C$_2$T$_x$ electrodes containing different amounts of NDs at varied scan rates is shown in Fig. 4.4b. Ti$_3$C$_2$T$_x$/NDs-10% and Ti$_3$C$_2$T$_x$/NDs-30% presented higher capacitance values at all tested scan rates when compared to the Ti$_3$C$_2$T$_x$ and Ti$_3$C$_2$T$_x$/NDs-5% electrodes, reflecting the beneficial effect of using NDs as pillars of the MXene framework. For example, the gravimetric capacitance of the Ti$_3$C$_2$T$_x$/NDs-10% at 100 (140 F/g) and 1000 mV/s (61 F/g) is 259 and 306% higher than that obtained for Ti$_3$C$_2$T$_x$ at the same scan rates. The better performance of the Ti$_3$C$_2$T$_x$/NDs-30% film at higher scan rates can be related to improved electrolyte access to the MXene. The capacitance retentions (Fig. B8) at 1000 mV/s of the Ti$_3$C$_2$T$_x$/NDs-10% and Ti$_3$C$_2$T$_x$/NDs-30% electrodes were found to be 26% and 42%, respectively, while for Ti$_3$C$_2$T$_x$ it was 13%.
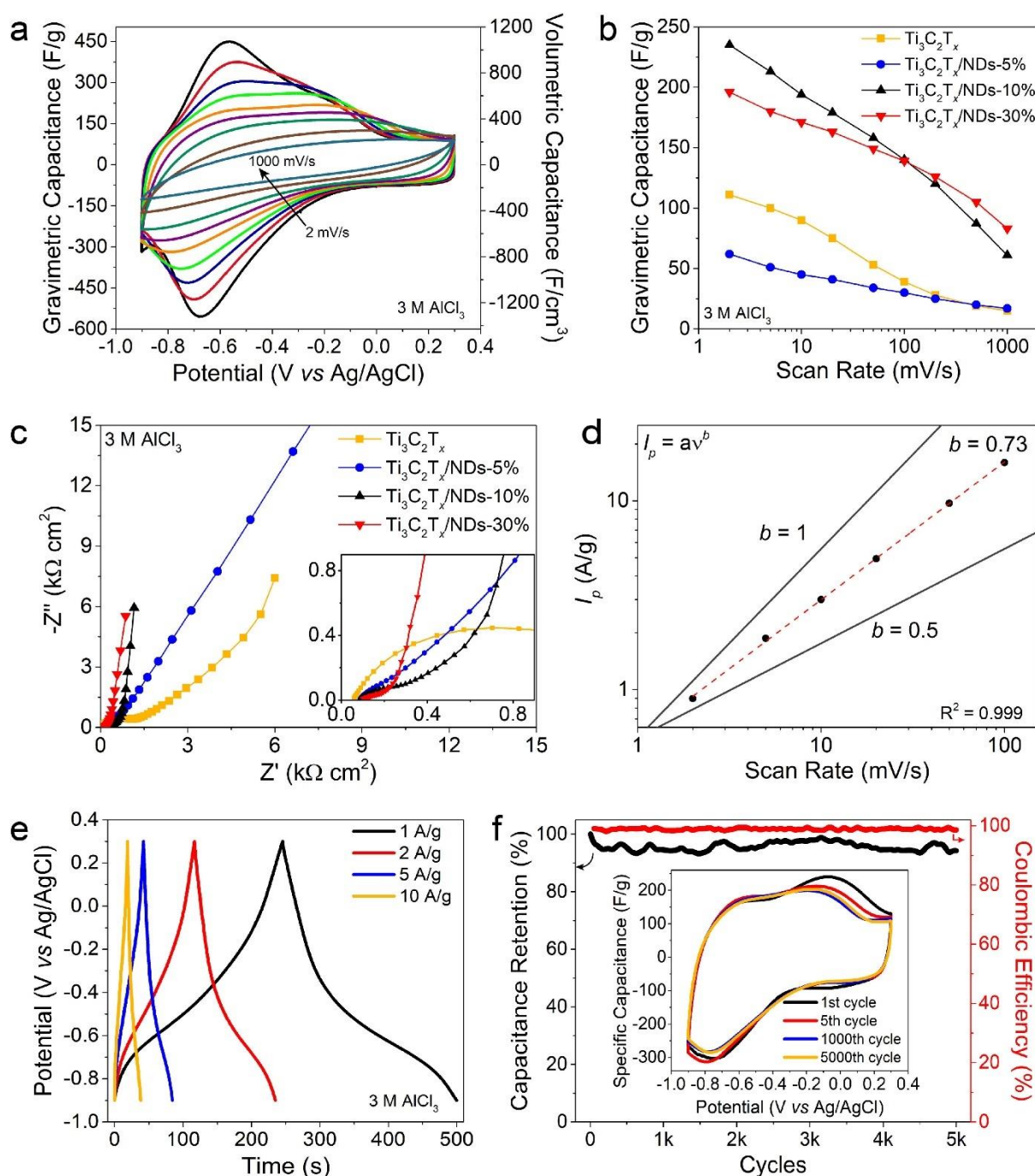
FIGURE 4.4: (a) Cyclic voltammograms (CVs) for Ti₃C₂Tₓ/NDs-10% in 3 M AlCl₃ at different scan rates (2, 5, 10, 20, 50, 100, 200, 500, and 1000 mV/s). (b) Gravimetric capacitance at different scan rates and (c) EIS for Ti₃C₂Tₓ and Ti₃C₂Tₓ/NDs electrodes collected at the open circuit potential (OCP) in 3 M AlCl₃. The inset in (c) shows the EIS data collected in the high-frequency region. (d) Determination of the *b* value from the slope of the log of the anodic peak current (I*p*) *vs* the log of the scan rate (*v*) from 2 to 100 mV/s in 3 M AlCl₃. (e) Galvanostatic charge-discharge (GCD) curves of Ti₃C₂Tₓ/NDs-10% in 3 M AlCl₃ at current densities of 1, 2, 5, and 10 A/g. (f) Capacitance retention and coulombic efficiency of Ti₃C₂Tₓ/NDs-10% in 3 M AlCl₃ over 5000 cycles at 100 mV/s. The inset shows the CVs for Ti₃C₂Tₓ/NDs-10% in 3 M AlCl₃ at the 1st, 5th, 1000th, and 5000th cycles. Reprinted with permission from Facure *et. al.*[175], Copyright 2023 Elsevier.

The electrochemical performance of $Ti_3C_2T_x$ films at high scan rates is highly dependent on ion diffusion.[113] To evaluate the diffusion contribution in each case, EIS characterization was performed. The Nyquist plots obtained (Fig. 4.4c) show nearly vertical lines at low frequency for $Ti_3C_2T_x$/NDs-10% and $Ti_3C_2T_x$/NDs-30%, while curves with smaller slopes are observed for $Ti_3C_2T_x$ and $Ti_3C_2T_x$/NDs-5%. The results show that diffusion is highly favored in the samples containing higher amounts of NDs (10% and 30%), while the inferior performance of $Ti_3C_2T_x$ and $Ti_3C_2T_x$/NDs-5% can be ascribed to the restacking of the MXene layers. Thus, the higher capacitance values and the better high-rate performance can be ascribed to the ion pathway optimization obtained when using NDs as pillars of the $Ti_3C_2T_x$ layers. The EIS data is also in accordance with the CVs obtained for each electrode (Fig. 4.2d), as discussed previously.

Given the highest capacitance value obtained with $Ti_3C_2T_x$/NDs-10% in 3 M AlCl₃, the system was further characterized. The slope (*b* value) of the curve obtained from the logarithm of the anodic peak current (I*p*) *vs* the logarithm of the scan rate was calculated (Fig. 4.4d). From 2 to 100 mV/s, a *b* value of 0.73 was obtained, indicating a contribution of both surface- and diffusion-controlled kinetics.[114] The electrochemical impedance spectra obtained at different potentials (Fig. B9) also indicate the contribution of these two processes. When the impedance was collected at 0.2 V, a potential in which the charge storage arises mainly from the electrical double-layer capacitance, the slope in the low-frequency range is almost vertical, indicating high diffusion and surface-controlled kinetics. When the impedance is recorded at -0.6 V, a region in which there are peaks in the CVs related to the redox reactions from proton intercalation, the slope of the curves at low frequencies decreases. This behavior suggests a diffusion-controlled process and a pseudocapacitive charge storage mechanism at this potential range. As stated above, the contribution of both processes reflects the b value obtained.[114]

The galvanostatic charge-discharge (GCD) curves for $Ti_3C_2T_x$/NDs-10% in 3 M AlCl₃ at different current densities are shown in Fig. 4.4e. The GCD profiles obtained are characteristic of pseudocapacitive materials,[114] in accordance with what was observed in the other characterizations performed (CVs and *b* value). The Coulombic efficiency at 1 A/g was found to be 96.5%. As shown in Fig. 4.4f, the $Ti_3C_2T_x$/NDs-10% electrode presented high stability, retaining 94% of the capacitance after 5000 cycles at 100 mV/s and presenting a coulombic efficiency close to 100%

over all cycles, confirming the absence of parasitic reactions. The stability results show that the use of NDs as pillars is effective in avoiding the restacking of the MXene layers, creating sustainable ion diffusion pathways, and contributing to the high stability of the material to be used in long-term cycling.

Commercial supercapacitors are constituted of electrodes with areal loading of about 10 mg/cm^2.[201] To evaluate the performance of the Ti$_3$C$_2$T$_x$/NDs-10% at higher mass densities, an electrode of 8.3 mg/cm^2 was used. Fig. B10 shows the CVs obtained in 3 M AlCl$_3$ at different scan rates. It is possible to see the peaks related to proton intercalation at low scan rates. The capacitance of the high-density film was 92.3 F/g at 2 mV/s, ca. 40% of the capacitance obtained with the 1 mg/cm^2 film. These results show that even at high mass loadings, the pillaring effect of the NDs is still observed, which enables the use of thicker electrodes in AlCl$_3$ and other acidic electrolytes.

4.5. Conclusions

In this work, hybrid supercapacitor electrode films were obtained using Ti$_3$C$_2$T$_x$ and nanodiamonds. It was shown that the NDs acted as pillars between the MXene layers, which enabled the use of the hybrid electrodes in AlCl$_3$ electrolyte, providing high capacitance values and superior high-rate performance. The obtained capacitance was attributed mainly to the H$^+$ redox reaction with O terminations. In comparison to the pure Ti$_3$C$_2$T$_x$ film, the excellent performance of the Ti$_3$C$_2$T$_x$/NDs-10% is due to the pillaring effect that effectively prevented the restacking of the MXene sheets. Furthermore, the use of 3 M AlCl$_3$, in addition to providing protons that led to high capacitance values, also expanded the potential window. It was possible due to the concentration used that reduces the availability of water, avoiding side reactions under extreme potentials. This system can also be explored in future works to deeply investigate the performance of a full-cell supercapacitor and the device's energy density. The results presented here show that high capacitance values can be obtained without using electrolytes which are limited in the potential window, giving rise to higher energy densities while retaining high power density. Also, other types of MXenes and electrolytes can be further explored using NDs in the search for even better performances.

5.   Final remarks and Future Perspectives

In this thesis, different nanomaterials were rationally synthesized for optimizing their performance as sensors and supercapacitor electrode. Specifically, in the first work, GQDs hydrothermal synthesis was systematically studied aiming to obtain higher QY values and more in-depth knowledge about the relationship of the synthesis parameters with the GQDs properties. The GQDs were then used in fluorescence sensing of Fe^{3+} ions, which helped to understand the performance of the tested materials. A few remarks about the results obtained can be highlighted:

- The use of factorial designs to study the GQDs hydrothermal synthesis led to a condition in which an optimized QY value was obtained by using a simpler hydrothermal synthesis route compared to those previously reported in the literature;

- The characterization of the synthesized GQDs enabled the understanding of the influence of the synthesis parameters on the GQDs properties;

- By obtaining GQDs with different features, Fe^{3+} detection could be performed with different sensitivity and linear range.

In the other work, $Ti_3C_2T_x$ MXenes were combined with nanodiamonds which acted as pillars between the MXene layers and enabled the achievement of high capacitance values, good high-rate performance, and large potential window in $AlCl_3$ electrolyte. Here, we can highlight that:

- The study of the appropriate amount of NDs to use as pillars between the MXene sheets led to an optimized value that resulted in high proton diffusion and in a good performance as a supercapacitor electrode;

- The use of 3 M $AlCl_3$ also shown to be appropriate to provide the right balance between protons, that contributed to the pseudo-capacitance mechanism, and water, that contributed to the enhancement of the capacitance;

- The electrolyte also enabled the use of a relatively large potential window due to its high concentration.

In summary, the results presented here illustrate that by investigating and rationally designing customized nanomaterials, one can achieve devices with enhanced performances for a given application.

In terms of future works, the results presented here enable the tailoring of the GQDs properties for other applications due to the knowledge acquired regarding

how syntheses influence the properties and composition of this material. For instance, the performance of the GQDs when used as nanozyme for sensing, in catalysis, and as adsorbent can be optimized since it is very influenced by the functional groups present on the material's surface, which in turn, can be tailored by the synthesis conditions. Also, the results obtained suggest that other nanomaterials can be explored in combination with MXenes, as well as other electrolytes can be investigated for supercapacitor devices with enhanced properties. Also, MXenes show high potential to be further explored in other several applications, such as in printable electronics, sensing, and environmental remediation.

6.   References

(1)   Novoselov, K. S.; Geim, A. K.; Morozov, S. V; Jiang, D.; Zhang, Y.; Dubonos, S. V; Grigorieva, I. V; Firsov, A. A. Electric Field Effect in Atomically Thin Carbon Films. *Science* **2004**, *306* (5696), 666 LP – 669. https://doi.org/10.1126/science.1102896.

(2)   Novoselov, K. S.; Jiang, D.; Schedin, F.; Booth, T. J.; Khotkevich, V. V.; Morozov, S. V.; Geim, A. K. Two-Dimensional Atomic Crystals. *Proceedings of the National Academy of Sciences* **2005**, *102* (30), 10451–10453. https://doi.org/10.1073/pnas.0502848102.

(3)   Jariwala, D.; Sangwan, V. K.; Lauhon, L. J.; Marks, T. J.; Hersam, M. C. Carbon Nanomaterials for Electronics, Optoelectronics, Photovoltaics, and Sensing. *Chem Soc Rev* **2013**, *42* (7), 2824–2860. https://doi.org/10.1039/C2CS35335K.

(4)   Tian, P.; Tang, L.; Teng, K. S.; Lau, S. P. Graphene Quantum Dots from Chemistry to Applications. *Mater Today Chem* **2018**, *10*, 221–258. https://doi.org/10.1016/j.mtchem.2018.09.007.

(5)   Ponomarenko, L. A.; Schedin, F.; Katsnelson, M. I.; Yang, R.; Hill, E. W.; Novoselov, K. S.; Geim, A. K. Chaotic Dirac Billiard in Graphene Quantum Dots. *Science* **2008**, *320* (5874), 356 LP – 358. https://doi.org/10.1126/science.1154663.

(6)   Facure, M. H. M.; Schneider, R.; Mercante, L. A.; Correa, D. S. A Review on Graphene Quantum Dots and Their Nanocomposites: From Laboratory Synthesis towards Agricultural and Environmental Applications. *Environ Sci Nano* **2020**, *7* (12), 3710–3734. https://doi.org/10.1039/D0EN00787K.

(7)   Haque, E.; Kim, J.; Malgras, V.; Reddy, K. R.; Ward, A. C.; You, J.; Bando, Y.; Hossain, Md. S. A.; Yamauchi, Y. Recent Advances in Graphene Quantum Dots: Synthesis, Properties, and Applications. *Small Methods* **2018**, *2* (10), 1800050. https://doi.org/10.1002/smtd.201800050.

(8)   Facure, M. H. M.; Schneider, R.; Lima, J. B. S.; Mercante, L. A.; Correa, D. S. Graphene Quantum Dots-Based Nanocomposites Applied in Electrochemical Sensors: A Recent Survey. *Electrochem* **2021**, *2* (3). https://doi.org/10.3390/electrochem2030032.

(9)   Liu, F.; Jang, M.-H.; Ha, H. D.; Kim, J.-H.; Cho, Y.-H.; Seo, T. S. Facile Synthetic Method for Pristine Graphene Quantum Dots and Graphene Oxide Quantum Dots: Origin of Blue and Green Luminescence. *Advanced Materials* **2013**, *25* (27), 3657–3662. https://doi.org/10.1002/adma.201300233.

(10)   Ha, H. D.; Jang, M.-H.; Liu, F.; Cho, Y.-H.; Seo, T. S. Upconversion Photoluminescent Metal Ion Sensors via Two Photon Absorption in Graphene Oxide Quantum Dots. *Carbon N Y* **2015**, *81*, 367–375. https://doi.org/10.1016/j.carbon.2014.09.069.

(11)   Bacon, M.; Bradley, S. J.; Nann, T. Graphene Quantum Dots. *Particle & Particle Systems Characterization* **2014**, *31*, 415–428. https://doi.org/10.1002/ppsc.201300252.

(12) Li, L.; Wu, G.; Yang, G.; Peng, J.; Zhao, J.; Zhu, J. J. Focusing on Luminescent Graphene Quantum Dots: Current Status and Future Perspectives. *Nanoscale* **2013**, *5* (10), 4015–4039. https://doi.org/10.1039/c3nr33849e.

(13) Feng, J.; Dong, H.; Yu, L.; Dong, L. The Optical and Electronic Properties of Graphene Quantum Dots with Oxygen-Containing Groups: A Density Functional Theory Study. *J Mater Chem C Mater* **2017**, *5* (24), 5984–5993. https://doi.org/10.1039/C7TC00631D.

(14) Gao, W.; Alemany, L. B.; Ci, L.; Ajayan, P. M. New Insights into the Structure and Reduction of Graphite Oxide. *Nat Chem* **2009**, *1* (5), 403–408. https://doi.org/10.1038/nchem.281.

(15) Facure, M. H. M.; Schneider, R.; Alvarenga, A. D.; Mercante, L. A.; Correa, D. S. Forms of Graphene I—Graphene Oxide and Reduced Graphene Oxide. In *Recent Advances in Graphene and Graphene-Based Technologies*; IOP Publishing, 2023; pp 3–27. https://doi.org/10.1088/978-0-7503-3999-5ch3.

(16) Sanati, F. F. and A. L. Graphene Quantum Dots in Electrochemical Sensors/Biosensors. *Curr Anal Chem* **2019**, *15* (2), 103–123. https://doi.org/10.2174/1573411014666180319145506.

(17) Li, M.; Chen, T.; Gooding, J. J.; Liu, J. Review of Carbon and Graphene Quantum Dots for Sensing. *ACS Sens* **2019**, *4* (7), 1732–1748. https://doi.org/10.1021/acssensors.9b00514.

(18) Yan, Y.; Gong, J.; Chen, J.; Zeng, Z.; Huang, W.; Pu, K.; Liu, J.; Chen, P. Recent Advances on Graphene Quantum Dots: From Chemistry and Physics to Applications. *Advanced Materials* **2019**, *31* (21), 1–22. https://doi.org/10.1002/adma.201808283.

(19) Dong, Y.; Shao, J.; Chen, C.; Li, H.; Wang, R.; Chi, Y.; Lin, X.; Chen, G. Blue Luminescent Graphene Quantum Dots and Graphene Oxide Prepared by Tuning the Carbonization Degree of Citric Acid. *Carbon N Y* **2012**, *50* (12), 4738–4743. https://doi.org/10.1016/j.carbon.2012.06.002.

(20) Zhu, S.; Shao, J.; Song, Y.; Zhao, X.; Du, J.; Wang, L.; Wang, H.; Zhang, K.; Zhang, J.; Yang, B. Investigating the Surface State of Graphene Quantum Dots. *Nanoscale* **2015**, *7* (17), 7927–7933. https://doi.org/10.1039/c5nr01178g.

(21) Mei, S.; Wei, X.; Hu, Z.; Wei, C.; Su, D.; Yang, D.; Zhang, G.; Zhang, W.; Guo, R. Amphipathic Carbon Dots with Solvent-Dependent Optical Properties and Sensing Application. *Opt Mater (Amst)* **2019**, *89*, 224–230. https://doi.org/10.1016/j.optmat.2019.01.021.

(22) Xi, F.; Zhao, J.; Shen, C.; He, J.; Chen, J.; Yan, Y.; Li, K.; Liu, J.; Chen, P. Amphiphilic Graphene Quantum Dots as a New Class of Surfactants. *Carbon N Y* **2019**, *153*, 127–135. https://doi.org/10.1016/j.carbon.2019.07.014.

(23) Sun, Y.; Wang, S.; Li, C.; Luo, P.; Tao, L.; Wei, Y.; Shi, G. Large Scale Preparation of Graphene Quantum Dots from Graphite with Tunable Fluorescence Properties. *Physical Chemistry Chemical Physics* **2013**, *15* (24), 9907–9913. https://doi.org/10.1039/c3cp50691f.

(24) Pan, D.; Guo, L.; Zhang, J.; Xi, C.; Xue, Q.; Huang, H.; Li, J.; Zhang, Z.; Yu, W.; Chen, Z.; Li, Z.; Wu, M. Cutting Sp^2 Clusters in Graphene Sheets into Colloidal Graphene Quantum Dots with Strong Green Fluorescence. *J Mater Chem* **2012**, *22* (8), 3314–3318. https://doi.org/10.1039/c2jm16005f.

(25) Pan, D.; Zhang, J.; Li, Z.; Wu, M. Hydrothermal Route for Cutting Graphene Sheets into Blue-Luminescent Graphene Quantum Dots. *Advanced Materials* **2010**, *22* (6), 734–738. https://doi.org/10.1002/adma.200902825.

(26) Chen, W.; Li, F.; Wu, C.; Guo, T. Optical Properties of Fluorescent Zigzag Graphene Quantum Dots Derived from Multi-Walled Carbon Nanotubes. *Appl Phys Lett* **2014**, *104* (6), 63109. https://doi.org/10.1063/1.4863963.

(27) Peng, J.; Gao, W.; Gupta, B. K.; Liu, Z.; Romero-Aburto, R.; Ge, L.; Song, L.; Alemany, L. B.; Zhan, X.; Gao, G.; Vithayathil, S. A.; Kaipparettu, B. A.; Marti, A. A.; Hayashi, T.; Zhu, J.-J.; Ajayan, P. M. Graphene Quantum Dots Derived from Carbon Fibers. *Nano Lett* **2012**, *12* (2), 844–849. https://doi.org/10.1021/nl2038979.

(28) Chen, A.; Zhao, C.; Yu, Y.; Yang, J. Graphene Quantum Dots Derived from Carbon Fibers for Oxidation of Dopamine. *Journal of Wuhan University of Technology-Mater. Sci. Ed.* **2016**, *31* (6), 1294–1297. https://doi.org/10.1007/s11595-016-1529-y.

(29) Xie, J.-D. De; Lai, G.-W. W.; Huq, M. M. Hydrothermal Route to Graphene Quantum Dots: Effects of Precursor and Temperature. *Diam Relat Mater* **2017**, *79* (July), 112–118. https://doi.org/10.1016/j.diamond.2017.08.014.

(30) Tian, R.; Zhong, S.; Wu, J.; Jiang, W.; Wang, T. Facile Hydrothermal Method to Prepare Graphene Quantum Dots from Graphene Oxide with Different Photoluminescences. *RSC Adv* **2016**, *6* (46), 40422–40426. https://doi.org/10.1039/C6RA00780E.

(31) Sun, J.; Yang, S.; Wang, Z.; Shen, H.; Xu, T.; Sun, L.; Li, H.; Chen, W.; Jiang, X.; Ding, G.; Kang, Z.; Xie, X.; Jiang, M. Ultra-High Quantum Yield of Graphene Quantum Dots: Aromatic-Nitrogen Doping and Photoluminescence Mechanism. *Particle and Particle Systems Characterization* **2015**, *32* (4), 434–440. https://doi.org/10.1002/ppsc.201400189.

(32) Zhu, S.; Zhang, J.; Qiao, C.; Tang, S.; Li, Y.; Yuan, W.; Li, B.; Tian, L.; Liu, F.; Hu, R.; Gao, H.; Wei, H.; Zhang, H.; Sun, H.; Yang, B. Strongly Green-Photoluminescent Graphene Quantum Dots for Bioimaging Applications. *Chemical Communications* **2011**, *47* (24), 6858–6860. https://doi.org/10.1039/C1CC11122A.

(33) He, M.; Guo, X.; Huang, J.; Shen, H.; Zeng, Q.; Wang, L. Mass Production of Tunable Multicolor Graphene Quantum Dots from an Energy Resource of Coke by a One-Step Electrochemical Exfoliation. *Carbon N Y* **2018**, *140*, 508–520. https://doi.org/10.1016/j.carbon.2018.08.067.

(34) Chu, K.; Adsetts, J. R.; He, S.; Zhan, Z.; Yang, L.; Wong, J. M.; Love, D. A.; Ding, Z. Electrogenerated Chemiluminescence and Electroluminescence of N-Doped Graphene Quantum Dots Fabricated from an Electrochemical Exfoliation Process in Nitrogen-Containing

Electrolytes. *Chemistry – A European Journal* **2020**, *26* (68), 15892–15900. https://doi.org/10.1002/chem.202003395.

(35) Zhang, C.; Cui, Y.; Song, L.; Liu, X.; Hu, Z. Microwave Assisted One-Pot Synthesis of Graphene Quantum Dots as Highly Sensitive Fluorescent Probes for Detection of Iron Ions and PH Value. *Talanta* **2016**, *150*, 54–60. https://doi.org/10.1016/j.talanta.2015.12.015.

(36) Li, L.-L.; Ji, J.; Fei, R.; Wang, C.-Z.; Lu, Q.; Zhang, J.-R.; Jiang, L.-P.; Zhu, J.-J. A Facile Microwave Avenue to Electrochemiluminescent Two-Color Graphene Quantum Dots. *Adv Funct Mater* **2012**, *22* (14), 2971–2979. https://doi.org/10.1002/adfm.201200166.

(37) Zhu, Y.; Wang, G.; Jiang, H.; Chen, L.; Zhang, X. One-Step Ultrasonic Synthesis of Graphene Quantum Dots with High Quantum Yield and Their Application in Sensing Alkaline Phosphatase. *Chemical Communications* **2015**, *51* (5), 948–951. https://doi.org/10.1039/C4CC07449A.

(38) Benítez-Martínez, S.; Valcárcel, M. Graphene Quantum Dots in Analytical Science. *Trends in Analytical Chemistry* **2015**, *72*, 93–113. https://doi.org/10.1016/j.trac.2015.03.020.

(39) Chen, W.; Lv, G.; Hu, W.; Li, D.; Chen, S.; Dai, Z. Synthesis and Applications of Graphene Quantum Dots: A Review. *Nanotechnol Rev* **2018**, *7* (2), 157–185. https://doi.org/10.1515/ntrev-2017-0199.

(40) Chua, C. K.; Sofer, Z.; Šimek, P.; Jankovský, O.; Klímová, K.; Bakardjieva, S.; Hrdličková Kučková, Š.; Pumera, M. Synthesis of Strongly Fluorescent Graphene Quantum Dots by Cage-Opening Buckminsterfullerene. *ACS Nano* **2015**, *9* (3), 2548–2555. https://doi.org/10.1021/nn505639q.

(41) Kaciulis, S.; Mezzi, A.; Soltani, P.; Pizzoferrato, R.; Ciotta, E.; Prosposito, P. Graphene Quantum Dots Obtained by Unfolding Fullerene. *Thin Solid Films* **2019**, *673*, 19–25. https://doi.org/10.1016/j.tsf.2019.01.030.

(42) Hallaj, T.; Amjadi, M.; Manzoori, J. L.; Shokri, R. Chemiluminescence Reaction of Glucose-Derived Graphene Quantum Dots with Hypochlorite, and Its Application to the Determination of Free Chlorine. *Microchimica Acta* **2015**, *182* (3), 789–796. https://doi.org/10.1007/s00604-014-1389-0.

(43) Shehab, M.; Ebrahim, S.; Soliman, M. Graphene Quantum Dots Prepared from Glucose as Optical Sensor for Glucose. *J Lumin* **2017**, *184*, 110–116. https://doi.org/10.1016/j.jlumin.2016.12.006.

(44) Wang, S.; Chen, Z. G.; Cole, I.; Li, Q. Structural Evolution of Graphene Quantum Dots during Thermal Decomposition of Citric Acid and the Corresponding Photoluminescence. *Carbon N Y* **2015**, *82* (C), 304–313. https://doi.org/10.1016/j.carbon.2014.10.075.

(45) Alizadeh, T.; Shokri, M. A New Humidity Sensor Based upon Graphene Quantum Dots Prepared via Carbonization of Citric Acid. *Sens Actuators B Chem* **2016**, *222*, 728–734. https://doi.org/10.1016/j.snb.2015.08.122.

(46) Wu, X.; Tian, F.; Wang, W.; Chen, J.; Wu, M.; Zhao, J. X. Fabrication of Highly Fluorescent Graphene Quantum Dots Using L-Glutamic Acid for in Vitro/in Vivo Imaging and Sensing. *J Mater Chem C Mater* **2013**, *1* (31), 4676–4684. https://doi.org/10.1039/C3TC30820K.

(47) Pan, D.; Guo, L.; Zhang, J.; Xi, C.; Xue, Q.; Huang, H.; Li, J.; Zhang, Z.; Yu, W.; Chen, Z.; Li, Z.; Wu, M. Cutting Sp^2 clusters in Graphene Sheets into Colloidal Graphene Quantum Dots with Strong Green Fluorescence. *J Mater Chem* **2012**, *22* (8), 3314–3318. https://doi.org/10.1039/C2JM16005F.

(48) Lu, Q.; Zhang, Y.; Liu, S. Graphene Quantum Dots Enhanced Photocatalytic Activity of Zinc Porphyrin toward the Degradation of Methylene Blue under Visible-Light Irradiation. *J Mater Chem A Mater* **2015**, *3* (16), 8552–8558. https://doi.org/10.1039/C5TA00525F.

(49) Zhao, M. Direct Synthesis of Graphene Quantum Dots with Different Fluorescence Properties by Oxidation of Graphene Oxide Using Nitric Acid. *Applied Sciences* **2018**, *8* (8). https://doi.org/10.3390/app8081303.

(50) Kim, J.; Lee, B.; Kim, Y. J.; Hwang, S. W. Enhancement of Dye-Sensitized Solar Cells Efficiency Using Graphene Quantum Dots as Photoanode. *Bull Korean Chem Soc* **2019**, *40* (1), 56–61. https://doi.org/10.1002/bkcs.11664.

(51) Moreira Facure, M. H.; Schneider, R.; Mercante, L.; Correa, D. A Review on Graphene Quantum Dots and Their Nanocomposites: From Laboratory Synthesis towards Agricultural and Environmental Applications. *Environ Sci Nano* **2020**. https://doi.org/10.1039/d0en00787k.

(52) Costa-Fernández, J. M.; Pereiro, R.; Sanz-Medel, A. The Use of Luminescent Quantum Dots for Optical Sensing. *Trends in Analytical Chemistry* **2006**, *25* (3), 207–218. https://doi.org/10.1016/j.trac.2005.07.008.

(53) Valenta, J. Determination of Absolute Quantum Yields of Luminescing Nanomaterials over a Broad Spectral Range: From the Integrating Sphere Theory to the Correct Methodology. *Nanoscience Methods* **2014**, *3* (January 2017), 11–27. https://doi.org/10.1080/21642311.2014.884288.

(54) Xie, R.; Wang, Z.; Zhou, W.; Liu, Y.; Fan, L.; Li, Y.; Li, X. Graphene Quantum Dots as Smart Probes for Biosensing. In *Analytical Methods*; 2016; Vol. 8, pp 4001–4006. https://doi.org/10.1039/c6ay00289g.

(55) Zhang, Z.; Zhang, J.; Chen, N.; Qu, L. Graphene Quantum Dots: An Emerging Material for Energy-Related Applications and Beyond. *Energy Environ Sci* **2012**, *5* (10), 8869–8890. https://doi.org/10.1039/c2ee22982j.

(56) Zhu, S.; Zhang, J.; Tang, S.; Qiao, C.; Wang, L.; Wang, H.; Liu, X.; Li, B.; Li, Y.; Yu, W.; Wang, X.; Sun, H.; Yang, B. Surface Chemistry Routes to Modulate the Photoluminescence of Graphene Quantum Dots: From Fluorescence Mechanism to up-Conversion Bioimaging Applications. *Adv Funct Mater* **2012**, *22* (22), 4732–4740. https://doi.org/10.1002/adfm.201201499.

(57) Tang, L.; Ji, R.; Cao, X.; Lin, J.; Jiang, H.; Li, X.; Teng, K. S.; Luk, C. M.; Zeng, S.; Hao, J.; Lau, S. P. Deep Ultraviolet Photoluminescence of Water-Soluble Self-Passivated Graphene Quantum Dots. *ACS Nano* **2012**, *6* (6), 5102–5110. https://doi.org/10.1021/nn300760g.

(58) Zhu, S.; Song, Y.; Zhao, X.; Shao, J.; Zhang, J.; Yang, B. The Photoluminescence Mechanism in Carbon Dots (Graphene Quantum

Dots, Carbon Nanodots, and Polymer Dots): Current State and Future Perspective. *Nano Res* **2015**, *8* (2), 355–381. https://doi.org/10.1007/s12274-014-0644-3.

(59) Liu, Y.; Wang, R.; Lang, J.; Yan, X. Insight into the Formation Mechanism of Graphene Quantum Dots and the Size Effect on Their Electrochemical Behaviors. *Physical Chemistry Chemical Physics* **2015**, *17* (21), 14028–14035. https://doi.org/10.1039/C5CP00646E.

(60) Shen, J.; Zhu, Y.; Yang, X.; Li, C. Graphene Quantum Dots: Emergent Nanolights for Bioimaging, Sensors, Catalysis and Photovoltaic Devices. *Chemical Communications* **2012**, *48*, 3686–3699. https://doi.org/10.1039/c2cc00110a.

(61) Sun, H.; Wu, L.; Wei, W.; Qu, X. Recent Advances in Graphene Quantum Dots for Sensing. *Materials Today* **2013**, *16* (11), 433–442. https://doi.org/10.1016/j.mattod.2013.10.020.

(62) Zheng, X. T.; Ananthanarayanan, A.; Luo, K. Q.; Chen, P. Glowing Graphene Quantum Dots and Carbon Dots: Properties, Syntheses, and Biological Applications. *Small.* 2015, pp 1620–1636. https://doi.org/10.1002/smll.201402648.

(63) Kundu, S.; Pillai, V. K. Synthesis and Characterization of Graphene Quantum Dots. *Physical Sciences Reviews* **2019**, *5* (4), 1–35. https://doi.org/10.1515/psr-2019-0013.

(64) Wang, L.; Zhu, S. J.; Wang, H. Y.; Qu, S. N.; Zhang, Y. L.; Zhang, J. H.; Chen, Q. D.; Xu, H. L.; Han, W.; Yang, B.; Sun, H. B. Common Origin of Green Luminescence in Carbon Nanodots and Graphene Quantum Dots. *ACS Nano* **2014**, *8* (3), 2541–2547. https://doi.org/10.1021/nn500368m.

(65) Zhu, S.; Song, Y.; Wang, J.; Wan, H.; Zhang, Y.; Ning, Y.; Yang, B. Photoluminescence Mechanism in Graphene Quantum Dots: Quantum Confinement Effect and Surface/Edge State. *Nano Today* **2017**, *13*, 10–14. https://doi.org/10.1016/j.nantod.2016.12.006.

(66) Jang, M.-H.; Ha, H. D.; Lee, E.-S.; Liu, F.; Kim, Y.-H.; Seo, T. S.; Cho, Y.-H. Is the Chain of Oxidation and Reduction Process Reversible in Luminescent Graphene Quantum Dots? *Small* **2015**, *11* (31), 3773–3781. https://doi.org/10.1002/smll.201500206.

(67) Shen, J.; Zhu, Y.; Yang, X.; Zong, J.; Zhang, J.; Li, C. One-Pot Hydrothermal Synthesis of Graphene Quantum Dots Surface-Passivated by Polyethylene Glycol and Their Photoelectric Conversion under near-Infrared Light. *New Journal of Chemistry* **2012**, *36* (1), 97–101. https://doi.org/10.1039/c1nj20658c.

(68) Tetsuka, H.; Asahi, R.; Nagoya, A.; Okamoto, K.; Tajima, I.; Ohta, R.; Okamoto, A. Optically Tunable Amino-Functionalized Graphene Quantum Dots. *Advanced Materials* **2012**, *24* (39), 5333–5338. https://doi.org/10.1002/adma.201201930.

(69) Qu, D.; Zheng, M.; Du, P.; Zhou, Y.; Zhang, L.; Li, D.; Tan, H.; Zhao, Z.; Xie, Z.; Sun, Z. Highly Luminescent S, N Co-Doped Graphene Quantum Dots with Broad Visible Absorption Bands for Visible Light Photocatalysts.

Nanoscale **2013**, *5* (24), 12272–12277. https://doi.org/10.1039/c3nr04402e.

(70) Yeh, P.-C.; Yoon, S.; Kurniawan, D.; Chung, Y. G.; Chiang, W.-H. Unraveling the Fluorescence Quenching of Colloidal Graphene Quantum Dots for Selective Metal Ion Detection. *ACS Appl Nano Mater* **2021**, *4* (6), 5636–5642. https://doi.org/10.1021/acsanm.1c00740.

(71) Anusuya, T.; Kumar, V.; Kumar, V. Hydrophilic Graphene Quantum Dots as Turn-off Fluorescent Nanoprobes for Toxic Heavy Metal Ions Detection in Aqueous Media. *Chemosphere* **2021**, *282*, 131019. https://doi.org/10.1016/j.chemosphere.2021.131019.

(72) Ma, Y.; Chen, A. Y.; Xie, X. F.; Wang, X. Y.; Wang, D.; Wang, P.; Li, H. J.; Yang, J. H.; Li, Y. Doping Effect and Fluorescence Quenching Mechanism of N-Doped Graphene Quantum Dots in the Detection of Dopamine. *Talanta* **2019**, *196*, 563–571. https://doi.org/10.1016/j.talanta.2019.01.001.

(73) Fan, L.; Hu, Y.; Wang, X.; Zhang, L.; Li, F.; Han, D.; Li, Z.; Zhang, Q.; Wang, Z.; Niu, L. Fluorescence Resonance Energy Transfer Quenching at the Surface of Graphene Quantum Dots for Ultrasensitive Detection of TNT. *Talanta* **2012**, *101*, 192–197. https://doi.org/10.1016/j.talanta.2012.08.048.

(74) Mukherjee, D.; Das, P.; Kundu, S.; Mandal, B. Engineering of Graphene Quantum Dots by Varying the Properties of Graphene Oxide for Fluorescence Detection of Picric Acid. *Chemosphere* **2022**, *300*, 134432. https://doi.org/10.1016/j.chemosphere.2022.134432.

(75) Asghari, S.; Mahmoudifard, M. The Detection of the Captured Circulating Tumor Cells on the Core-Shell Nanofibrous Membrane Using Hyaluronic Acid-Functionalized Graphene Quantum Dots. *J Biomed Mater Res B Appl Biomater* **2023**, *111* (5), 1121–1132. https://doi.org/10.1002/jbm.b.35219.

(76) Tade, R. S.; Patil, P. O. Fabrication of Poly-l-Lysine-Functionalized Graphene Quantum Dots for the Label-Free Fluorescent-Based Detection of Carcinoembryonic Antigen. *ACS Biomater Sci Eng* **2022**, *8* (2), 470–483. https://doi.org/10.1021/acsbiomaterials.1c01087.

(77) Li, G.; Liu, Z.; Gao, W.; Tang, B. Recent Advancement in Graphene Quantum Dots Based Fluorescent Sensor: Design, Construction and Bio-Medical Applications. *Coord Chem Rev* **2023**, *478*, 214966. https://doi.org/10.1016/j.ccr.2022.214966.

(78) Zhou, S.; Xu, H.; Gan, W.; Yuan, Q. Graphene Quantum Dots: Recent Progress in Preparation and Fluorescence Sensing Applications. *RSC Adv* **2016**, *6* (112), 110775–110788. https://doi.org/10.1039/c6ra24349e.

(79) Gogotsi, Y.; Anasori, B. The Rise of MXenes. *ACS Nano* **2019**, *13* (8), 8491–8494. https://doi.org/10.1021/acsnano.9b06394.

(80) Gogotsi, Y.; Huang, Q. MXenes: Two-Dimensional Building Blocks for Future Materials and Devices. *ACS Nano* **2021**, *15* (4), 5775–5780. https://doi.org/10.1021/acsnano.1c03161.

(81) Anasori, B.; Gogotsi, Y. Introduction to 2D Transition Metal Carbides and Nitrides (MXenes). In *2D Metal Carbides and Nitrides (MXenes): Structure,*

Properties and Applications; Anasori, B., Gogotsi, Y., Eds.; Springer International Publishing: Cham, 2019; pp 3–12. https://doi.org/10.1007/978-3-030-19026-2_1.

(82) Naguib, M.; Mochalin, V. N.; Barsoum, M. W.; Gogotsi, Y. 25th Anniversary Article: MXenes: A New Family of Two-Dimensional Materials. *Advanced Materials* **2014**, *26* (7), 992–1005. https://doi.org/10.1002/adma.201304138.

(83) Naguib, M.; Mashtalir, O.; Carle, J.; Presser, V.; Lu, J.; Hultman, L.; Gogotsi, Y.; Barsoum, M. W. Two-Dimensional Transition Metal Carbides. *ACS Nano* **2012**, *6* (2), 1322–1331. https://doi.org/10.1021/nn204153h.

(84) Salim, O.; Mahmoud, K. A.; Pant, K. K.; Joshi, R. K. Introduction to MXenes: Synthesis and Characteristics. *Mater Today Chem* **2019**, *14*, 100191. https://doi.org/10.1016/j.mtchem.2019.08.010.

(85) Naguib, M.; Barsoum, M. W.; Gogotsi, Y. Ten Years of Progress in the Synthesis and Development of MXenes. *Advanced Materials* **2021**, *2103393*, 1–10. https://doi.org/10.1002/adma.202103393.

(86) Yang, S.; Zhang, P.; Wang, F.; Ricciardulli, A. G.; Lohe, M. R.; Blom, P. W. M.; Feng, X. Fluoride-Free Synthesis of Two-Dimensional Titanium Carbide (MXene) Using A Binary Aqueous System. *Angewandte Chemie International Edition* **2018**, *57* (47), 15491–15495. https://doi.org/10.1002/anie.201809662.

(87) Sun, W.; Shah, S. A.; Chen, Y.; Tan, Z.; Gao, H.; Habib, T.; Radovic, M.; Green, M. J. Electrochemical Etching of Ti_2AlC to Ti_2CT_x (MXene) in Low-Concentration Hydrochloric Acid Solution. *J Mater Chem A Mater* **2017**, *5* (41), 21663–21668. https://doi.org/10.1039/C7TA05574A.

(88) Venkateshalu, S.; Grace, A. N. MXenes—A New Class of 2D Layered Materials: Synthesis, Properties, Applications as Supercapacitor Electrode and Beyond. *Appl Mater Today* **2020**, *18*, 100509. https://doi.org/10.1016/j.apmt.2019.100509.

(89) Naguib, M.; Kurtoglu, M.; Presser, V.; Lu, J.; Niu, J.; Heon, M.; Hultman, L.; Gogotsi, Y.; Barsoum, M. W. Two-Dimensional Nanocrystals Produced by Exfoliation of Ti_3AlC_2. *Advanced Materials* **2011**, *23* (37), 4248–4253. https://doi.org/10.1002/adma.201102306.

(90) Wang, Y.; Yue, Y.; Cheng, F.; Cheng, Y.; Ge, B.; Liu, N.; Gao, Y. $Ti_3C_2T_x$ MXene-Based Flexible Piezoresistive Physical Sensors. *ACS Nano* **2022**, *16* (2), 1734–1758. https://doi.org/10.1021/acsnano.1c09925.

(91) Kim, S. J.; Koh, H.-J.; Ren, C. E.; Kwon, O.; Maleski, K.; Cho, S.-Y.; Anasori, B.; Kim, C.-K.; Choi, Y.-K.; Kim, J.; Gogotsi, Y.; Jung, H.-T. Metallic $Ti_3C_2T_x$ MXene Gas Sensors with Ultrahigh Signal-to-Noise Ratio. *ACS Nano* **2018**, *12* (2), 986–993. https://doi.org/10.1021/acsnano.7b07460.

(92) Shao, H.; Xu, K.; Wu, Y. C.; Iadecola, A.; Liu, L.; Ma, H.; Qu, L.; Raymundo-Piñero, E.; Zhu, J.; Lin, Z.; Taberna, P. L.; Simon, P. Unraveling the Charge Storage Mechanism of $Ti_3C_2T_x$ MXene Electrode in Acidic Electrolyte. *ACS Energy Lett* **2020**, *5* (9), 2873–2880. https://doi.org/10.1021/acsenergylett.0c01290.

(93) Wang, X.; Mathis, T. S.; Sun, Y.; Tsai, W. Y.; Shpigel, N.; Shao, H.; Zhang, D.; Hantanasirisakul, K.; Malchik, F.; Balke, N.; Jiang, D. E.; Simon, P.; Gogotsi, Y. Titanium Carbide MXene Shows an Electrochemical Anomaly in Water-in-Salt Electrolytes. *ACS Nano* **2021**, *15* (9), 15274–15284. https://doi.org/10.1021/acsnano.1c06027.

(94) Sun, D.; Wang, M.; Li, Z.; Fan, G.; Fan, L.-Z.; Zhou, A. Two-Dimensional Ti_3C_2 as Anode Material for Li-Ion Batteries. *Electrochem commun* **2014**, *47*, 80–83. https://doi.org/10.1016/j.elecom.2014.07.026.

(95) Hu, S.; Li, S.; Xu, W.; Zhang, J.; Zhou, Y.; Cheng, Z. Rapid Preparation, Thermal Stability and Electromagnetic Interference Shielding Properties of Two-Dimensional Ti_3C_2 MXene. *Ceram Int* **2019**, *45* (16), 19902–19909. https://doi.org/10.1016/j.ceramint.2019.06.246.

(96) Zhou, Z.; Song, Q.; Huang, B.; Feng, S.; Lu, C. Facile Fabrication of Densely Packed Ti_3C_2 MXene/Nanocellulose Composite Films for Enhancing Electromagnetic Interference Shielding and Electro-/Photothermal Performance. *ACS Nano* **2021**, *15* (7), 12405–12417. https://doi.org/10.1021/acsnano.1c04526.

(97) Mi, X.; Su, Z.; Fu, Y.; Li, S.; Mo, A. 3D Printing of Ti_3C_2-MXene-Incorporated Composite Scaffolds for Accelerated Bone Regeneration. *Biomedical Materials* **2022**, *17* (3), 35002. https://doi.org/10.1088/1748-605X/ac5ffe.

(98) Siwal, S. S.; Kaur, H.; Chauhan, G.; Thakur, V. K. MXene-Based Nanomaterials for Biomedical Applications: Healthier Substitute Materials for the Future. *Adv Nanobiomed Res* **2023**, *3* (1), 2200123. https://doi.org/10.1002/anbr.202200123.

(99) Hatter, C. B.; Shah, J.; Anasori, B.; Gogotsi, Y. Micromechanical Response of Two-Dimensional Transition Metal Carbonitride (MXene) Reinforced Epoxy Composites. *Compos B Eng* **2020**, *182*, 107603. https://doi.org/10.1016/j.compositesb.2019.107603.

(100) Huang, W.-X.; Li, Z.-P.; Li, D.-D.; Hu, Z.-H.; Wu, C.; Lv, K.-L.; Li, Q. Ti_3C_2 MXene: Recent Progress in Its Fundamentals, Synthesis, and Applications. *Rare Metals* **2022**, *41* (10), 3268–3300. https://doi.org/10.1007/s12598-022-02058-2.

(101) Mathis, T. S.; Maleski, K.; Goad, A.; Sarycheva, A.; Anayee, M.; Foucher, A. C.; Hantanasirisakul, K.; Shuck, C. E.; Stach, E. A.; Gogotsi, Y. Modified MAX Phase Synthesis for Environmentally Stable and Highly Conductive Ti_3C_2 MXene. *ACS Nano* **2021**, *15* (4), 6420–6429. https://doi.org/10.1021/acsnano.0c08357.

(102) Kim, J.; Kwon, S.; Cho, D.-H.; Kang, B.; Kwon, H.; Kim, Y.; Park, S. O.; Jung, G. Y.; Shin, E.; Kim, W.-G.; Lee, H.; Ryu, G. H.; Choi, M.; Kim, T. H.; Oh, J.; Park, S.; Kwak, S. K.; Yoon, S. W.; Byun, D.; Lee, Z.; Lee, C. Direct Exfoliation and Dispersion of Two-Dimensional Materials in Pure Water via Temperature Control. *Nat Commun* **2015**, *6* (1), 8294. https://doi.org/10.1038/ncomms9294.

(103) Bergman, G.; Ballas, E.; Gao, Q.; Nimkar, A.; Gavriel, B.; Levi, M. D.; Sharon, D.; Malchik, F.; Wang, X.; Shpigel, N.; Mandler, D.; Aurbach, D. Elucidation of the Charging Mechanisms and the Coupled Structural–

Mechanical Behavior of $Ti_3C_2T_x$ (MXenes) Electrodes by In Situ Techniques. *Adv Energy Mater* **2023**, 2203154. https://doi.org/10.1002/aenm.202203154.

(104) Zhan, C.; Naguib, M.; Lukatskaya, M.; Kent, P. R. C.; Gogotsi, Y.; Jiang, D. Understanding the MXene Pseudocapacitance. *J Phys Chem Lett* **2018**, *9* (6), 1223–1228. https://doi.org/10.1021/acs.jpclett.8b00200.

(105) Mu, X.; Wang, D.; Du, F.; Chen, G.; Wang, C.; Wei, Y.; Gogotsi, Y.; Gao, Y.; Dall'Agnese, Y. Revealing the Pseudo-Intercalation Charge Storage Mechanism of MXenes in Acidic Electrolyte. *Adv Funct Mater* **2019**, *29* (29), 1902953. https://doi.org/10.1002/adfm.201902953.

(106) Naguib, M.; Come, J.; Dyatkin, B.; Presser, V.; Taberna, P.-L.; Simon, P.; Barsoum, M. W.; Gogotsi, Y. MXene: A Promising Transition Metal Carbide Anode for Lithium-Ion Batteries. *Electrochem commun* **2012**, *16* (1), 61–64. https://doi.org/10.1016/j.elecom.2012.01.002.

(107) Anasori, B.; Lukatskaya, M. R.; Gogotsi, Y. 2D Metal Carbides and Nitrides (MXenes) for Energy Storage. *Nat Rev Mater* **2017**, *2* (2), 16098. https://doi.org/10.1038/natrevmats.2016.98.

(108) Gao, X.; Du, X.; Mathis, T. S.; Zhang, M.; Wang, X.; Shui, J.; Gogotsi, Y.; Xu, M. Maximizing Ion Accessibility in MXene-Knotted Carbon Nanotube Composite Electrodes for High-Rate Electrochemical Energy Storage. *Nat Commun* **2020**, *11* (1), 6160. https://doi.org/10.1038/s41467-020-19992-3.

(109) Xia, Y.; Mathis, T. S.; Zhao, M.-Q.; Anasori, B.; Dang, A.; Zhou, Z.; Cho, H.; Gogotsi, Y.; Yang, S. Thickness-Independent Capacitance of Vertically Aligned Liquid-Crystalline MXenes. *Nature* **2018**, *557* (7705), 409–412. https://doi.org/10.1038/s41586-018-0109-z.

(110) Zhang, P.; Li, J.; Yang, D.; Soomro, R. A.; Xu, B. Flexible Carbon Dots-Intercalated MXene Film Electrode with Outstanding Volumetric Performance for Supercapacitors. *Adv Funct Mater* **2022**, *33* (1), 2209918. https://doi.org/10.1002/adfm.202209918.

(111) Fu, Q.; Wang, X.; Zhang, N.; Wen, J.; Li, L.; Gao, H.; Zhang, X. Self-Assembled $Ti_3C_2T_x$/SCNT Composite Electrode with Improved Electrochemical Performance for Supercapacitor. *J Colloid Interface Sci* **2018**, *511*, 128–134. https://doi.org/10.1016/j.jcis.2017.09.104.

(112) Lukatskaya, M. R.; Kota, S.; Lin, Z.; Zhao, M.-Q.; Shpigel, N.; Levi, M. D.; Halim, J.; Taberna, P.-L.; Barsoum, M. W.; Simon, P.; Gogotsi, Y. Ultra-High-Rate Pseudocapacitive Energy Storage in Two-Dimensional Transition Metal Carbides. *Nat Energy* **2017**, *2* (8), 17105. https://doi.org/10.1038/nenergy.2017.105.

(113) Tang, J.; Mathis, T.; Zhong, X.; Xiao, X.; Wang, H.; Anayee, M.; Pan, F.; Xu, B.; Gogotsi, Y. Optimizing Ion Pathway in Titanium Carbide MXene for Practical High-Rate Supercapacitor. *Adv Energy Mater* **2021**, *11* (4), 2003025. https://doi.org/10.1002/aenm.202003025.

(114) Mathis, T. S.; Kurra, N.; Wang, X.; Pinto, D.; Simon, P.; Gogotsi, Y. Energy Storage Data Reporting in Perspective—Guidelines for Interpreting the

Performance of Electrochemical Energy Storage Systems. *Adv Energy Mater* **2019**, *9* (39), 1–13. https://doi.org/10.1002/aenm.201902007.

(115) Tian, X.; Zhu, Q.; Xu, B. "Water-in-Salt" Electrolytes for Supercapacitors: A Review. *ChemSusChem* **2021**, *14* (12), 2501–2515. https://doi.org/10.1002/cssc.202100230.

(116) Suo, L.; Borodin, O.; Gao, T.; Olguin, M.; Ho, J.; Fan, X.; Luo, C.; Wang, C.; Xu, K. "Water-in-Salt" Electrolyte Enables High-Voltage Aqueous Lithium-Ion Chemistries. *Science* **2015**, *350* (6263), 938–943. https://doi.org/10.1126/science.aab1595.

(117) Facure, M. H. M.; Schneider, R.; Mercante, L. A.; Correa, D. S. Rational Hydrothermal Synthesis of Graphene Quantum Dots with Optimized Luminescent Properties for Sensing Applications. *Mater Today Chem* **2022**, *23*, 100755. https://doi.org/10.1016/j.mtchem.2021.100755.

(118) Geim, A. K.; Novoselov, K. S. The Rise of Graphene. *Nat Mater* **2007**, *6* (3), 183–191. https://doi.org/10.1038/nmat1849.

(119) Farjadian, F.; Abbaspour, S.; Sadatlu, M. A. A.; Mirkiani, S.; Ghasemi, A.; Hoseini-Ghahfarokhi, M.; Mozaffari, N.; Karimi, M.; Hamblin, M. R. Recent Developments in Graphene and Graphene Oxide: Properties, Synthesis, and Modifications: A Review. *ChemistrySelect* **2020**, *5* (33), 10200–10219. https://doi.org/10.1002/slct.202002501.

(120) Cotta, M. A. Quantum Dots and Their Applications: What Lies Ahead? *ACS Appl Nano Mater* **2020**, *3* (6), 4920–4924. https://doi.org/10.1021/acsanm.0c01386.

(121) Zhao, Y.; Wu, X.; Sun, S.; Ma, L.; Zhang, L.; Lin, H. A Facile and High-Efficient Approach to Yellow Emissive Graphene Quantum Dots from Graphene Oxide. *Carbon N Y* **2017**, *124*, 342–347. https://doi.org/10.1016/j.carbon.2017.09.011.

(122) Baragau, I.-A.; Power, N. P.; Morgan, D. J.; Lobo, R. A.; Roberts, C. S.; Titirici, M.-M.; Middelkoop, V.; Diaz, A.; Dunn, S.; Kellici, S. Efficient Continuous Hydrothermal Flow Synthesis of Carbon Quantum Dots from a Targeted Biomass Precursor for On–Off Metal Ions Nanosensing. *ACS Sustain Chem Eng* **2021**, *9* (6), 2559–2569. https://doi.org/10.1021/acssuschemeng.0c08594.

(123) Kellici, S.; Acord, J.; Moore, K. E.; Power, N. P.; Middelkoop, V.; Morgan, D. J.; Heil, T.; Coppo, P.; Baragau, I.-A.; Raston, C. L. Continuous Hydrothermal Flow Synthesis of Graphene Quantum Dots. *React Chem Eng* **2018**, *3* (6), 949–958. https://doi.org/10.1039/C8RE00158H.

(124) Yang, F.; Zhao, M.; Zheng, B.; Xiao, D.; Wu, L.; Guo, Y. Influence of PH on the Fluorescence Properties of Graphene Quantum Dots Using Ozonation Pre-Oxide Hydrothermal Synthesis. *J Mater Chem* **2012**, *22* (48), 25471–25479. https://doi.org/10.1039/C2JM35471C.

(125) Zheng, P.; Wu, N. Fluorescence and Sensing Applications of Graphene Oxide and Graphene Quantum Dots: A Review. *Chem Asian J* **2017**, *12* (18), 2343–2353. https://doi.org/10.1002/asia.201700814.

(126) Facure, M. H. M.; Mercante, L. A.; Mattoso, L. H. C.; Correa, D. S. Detection of Trace Levels of Organophosphate Pesticides Using an

Electronic Tongue Based on Graphene Hybrid Nanocomposites. *Talanta* **2017**, *167* (February), 59–66. https://doi.org/10.1016/j.talanta.2017.02.005.

(127) Facure, M. H. M.; Schneider, R.; dos Santos, D. M.; Correa, D. S. Impedimetric Electronic Tongue Based on Molybdenum Disulfide and Graphene Oxide for Monitoring Antibiotics in Liquid Media. *Talanta* **2020**, *217*, 121039. https://doi.org/10.1016/j.talanta.2020.121039.

(128) Chen, J.; Yao, B.; Li, C.; Shi, G. An Improved Hummers Method for Eco-Friendly Synthesis of Graphene Oxide. *Carbon N Y* **2013**, *64* (1), 225–229. https://doi.org/10.1016/j.carbon.2013.07.055.

(129) Rhys Williams, A. T.; Winfield, S. A.; Miller, J. N. Relative Fluorescence Quantum Yields Using a Computer-Controlled Luminescence Spectrometer. *Analyst* **1983**, *108* (1290), 1067–1071. https://doi.org/10.1039/an9830801067.

(130) Li, L.; Wu, G.; Hong, T.; Yin, Z.; Sun, D.; Abdel-Halim, E. S.; Zhu, J.-J. Graphene Quantum Dots as Fluorescence Probes for Turn-off Sensing of Melamine in the Presence of Hg^{2+}. *ACS Appl Mater Interfaces* **2014**, *6* (4), 2858–2864. https://doi.org/10.1021/am405305r.

(131) Andrade, D. F.; Machado, R. C.; Pereira-Filho, E. R. Proposition of Electronic Waste as a Reference Material – Part 2: Homogeneity, Stability, Characterization, and Uncertainties. *J Anal At Spectrom* **2019**, *34* (12), 2402–2410. https://doi.org/10.1039/C9JA00284G.

(132) Kharangarh, P. R.; Gupta, V.; Singh, A.; Bhardwaj, P.; Grace, A. N. An Efficient Pseudocapacitor Electrode Material with Co-Doping of Iron (II) and Sulfur in Luminescent Graphene Quantum Dots. *Diam Relat Mater* **2020**, *107*, 107913. https://doi.org/10.1016/j.diamond.2020.107913.

(133) Kharangarh, P. R.; Umapathy, S.; Singh, G. Thermal Effect of Sulfur Doping for Luminescent Graphene Quantum Dots. *ECS Journal of Solid State Science and Technology* **2018**, *7* (3), M29–M34. https://doi.org/10.1149/2.0041803jss.

(134) Dong, Y.; Pang, H.; Yang, H. Bin; Guo, C.; Shao, J.; Chi, Y.; Li, C. M.; Yu, T. Carbon-Based Dots Co-Doped with Nitrogen and Sulfur for High Quantum Yield and Excitation-Independent Emission. *Angewandte Chemie International Edition* **2013**, *52* (30), 7800–7804. https://doi.org/10.1002/anie.201301114.

(135) Kharangarh, P. R.; Umapathy, S.; Singh, G. Investigation of Sulfur Related Defects in Graphene Quantum Dots for Tuning Photoluminescence and High Quantum Yield. *Appl Surf Sci* **2018**, *449*, 363–370. https://doi.org/10.1016/j.apsusc.2018.01.026.

(136) Sun, H.; Gao, N.; Wu, L.; Ren, J.; Wei, W.; Qu, X. Highly Photoluminescent Amino-Functionalized Graphene Quantum Dots Used for Sensing Copper Ions. *Chemistry - A European Journal* **2013**, *19* (40), 13362–13368. https://doi.org/10.1002/chem.201302268.

(137) Jovanović, S. P.; Marković, Z. M.; Syrgiannis, Z.; Dramićanin, M. D.; Arcudi, F.; Parola, V. La; Budimir, M. D.; Marković, B. M. T. Enhancing Photoluminescence of Graphene Quantum Dots by Thermal Annealing of

the Graphite Precursor. *Mater Res Bull* **2017**, *93*, 183–193. https://doi.org/10.1016/j.materresbull.2017.04.052.

(138) Luo, P.; Qiu, Y.; Guan, X.; Jiang, L. Regulation of Photoluminescence Properties of Graphene Quantum Dots via Hydrothermal Treatment. *Physical Chemistry Chemical Physics* **2014**, *16* (35), 19011–19016. https://doi.org/10.1039/C4CP02652G.

(139) Dsouza, S. D.; Buerkle, M.; Brunet, P.; Maddi, C.; Padmanaban, D. B.; Morelli, A.; Payam, A. F.; Maguire, P.; Mariotti, D.; Svrcek, V. The Importance of Surface States in N-Doped Carbon Quantum Dots. *Carbon N Y* **2021**. https://doi.org/10.1016/j.carbon.2021.06.088.

(140) Tepliakov, N. V; Kundelev, E. V; Khavlyuk, P. D.; Xiong, Y.; Leonov, M. Y.; Zhu, W.; Baranov, A. V; Fedorov, A. V; Rogach, A. L.; Rukhlenko, I. D. Sp^2-Sp^3-Hybridized Atomic Domains Determine Optical Features of Carbon Dots. *ACS Nano* **2019**, *13* (9), 10737–10744. https://doi.org/10.1021/acsnano.9b05444.

(141) Biroju, R. K.; Rajender, G.; Giri, P. K. On the Origin and Tunability of Blue and Green Photoluminescence from Chemically Derived Graphene: Hydrogenation and Oxygenation Studies. *Carbon N Y* **2015**, *95*, 228–238. https://doi.org/10.1016/j.carbon.2015.08.036.

(142) Kim, J. K.; Kim, S. J.; Park, M. J.; Bae, S.; Cho, S.-P.; Du, Q. G.; Wang, D. H.; Park, J. H.; Hong, B. H. Surface-Engineered Graphene Quantum Dots Incorporated into Polymer Layers for High Performance Organic Photovoltaics. *Sci Rep* **2015**, *5* (1), 14276. https://doi.org/10.1038/srep14276.

(143) Hong, G. L.; Zhao, H. L.; Deng, H. H.; Yang, H. J.; Peng, H. P.; Liu, Y. H.; Chen, W. Fabrication of Ultra-Small Monolayer Graphene Quantum Dots by Pyrolysis of Trisodium Citrate for Fluorescent Cell Imaging. *Int J Nanomedicine* **2018**, *13*, 4807–4815. https://doi.org/10.2147/IJN.S168570.

(144) Trusovas, R.; Račiukaitis, G.; Niaura, G.; Barkauskas, J.; Valušis, G.; Pauliukaite, R. Recent Advances in Laser Utilization in the Chemical Modification of Graphene Oxide and Its Applications. *Adv Opt Mater* **2016**, *4* (1), 37–65. https://doi.org/10.1002/adom.201500469.

(145) Acik, M.; Lee, G.; Mattevi, C.; Pirkle, A.; Wallace, R. M.; Chhowalla, M.; Cho, K.; Chabal, Y. The Role of Oxygen during Thermal Reduction of Graphene Oxide Studied by Infrared Absorption Spectroscopy. *Journal of Physical Chemistry C* **2011**, *115* (40), 19761–19781. https://doi.org/10.1021/jp2052618.

(146) Silverstein, R. M.; Webster, F. X.; Kiemle, D. J.; Bryce, D. L. *Spectrometric Identification of Organic Compounds*, 8th ed.; Wiley, 2014.

(147) Mao, S.; Pu, H.; Chen, J. Graphene Oxide and Its Reduction: Modeling and Experimental Progress. *RSC Adv* **2012**, *2* (7), 2643–2662. https://doi.org/10.1039/c2ra00663d.

(148) Taniguchi, T.; Kurihara, S.; Tateishi, H.; Hatakeyama, K.; Koinuma, M.; Yokoi, H.; Hara, M.; Ishikawa, H.; Matsumoto, Y. PH-Driven, Reversible

Epoxy Ring Opening/Closing in Graphene Oxide. *Carbon N Y* **2015**, *84* (1), 560–566. https://doi.org/10.1016/j.carbon.2014.12.054.

(149) Kwan, Y. C. G.; Ng, G. M.; Huan, C. H. A. Identification of Functional Groups and Determination of Carboxyl Formation Temperature in Graphene Oxide Using the XPS O 1s Spectrum. *Thin Solid Films* **2015**, *590*, 40–48. https://doi.org/10.1016/j.tsf.2015.07.051.

(150) Le, G. T. T.; Manyam, J.; Opaprakasit, P.; Chanlek, N.; Grisdanurak, N.; Sreearunothai, P. Divergent Mechanisms for Thermal Reduction of Graphene Oxide and Their Highly Different Ion Affinities. *Diam Relat Mater* **2018**, *89* (September), 246–256. https://doi.org/10.1016/j.diamond.2018.09.006.

(151) Chua, C. K.; Pumera, M. Chemical Reduction of Graphene Oxide: A Synthetic Chemistry Viewpoint. *Chem. Soc. Rev.* **2014**, *43* (1), 291–312. https://doi.org/10.1039/C3CS60303B.

(152) Whitby, R. L. D.; Korobeinyk, A.; Gun'Ko, V. M.; Busquets, R.; Cundy, A. B.; László, K.; Skubiszewska-Ziba, J.; Leboda, R.; Tombacz, E.; Toth, I. Y.; Kovacs, K.; Mikhalovsky, S. V. PH-Driven Physicochemical Conformational Changes of Single-Layer Graphene Oxide. *Chemical Communications* **2011**, *47* (34), 9645–9647. https://doi.org/10.1039/c1cc13725e.

(153) Rajender, G.; Goswami, U.; Giri, P. K. Solvent Dependent Synthesis of Edge-Controlled Graphene Quantum Dots with High Photoluminescence Quantum Yield and Their Application in Confocal Imaging of Cancer Cells. *J Colloid Interface Sci* **2019**, *541*, 387–398. https://doi.org/10.1016/j.jcis.2019.01.099.

(154) Sengupta, I.; Chakraborty, S.; Talukdar, M.; Pal, S. K.; Chakraborty, S. Thermal Reduction of Graphene Oxide: How Temperature Influences Purity. *J Mater Res* **2018**, *33* (23), 4113–4122. https://doi.org/10.1557/jmr.2018.338.

(155) Orth, E. S.; Ferreira, J. G. L.; Fonsaca, J. E. S.; Blaskievicz, S. F.; Domingues, S. H.; Dasgupta, A.; Terrones, M.; Zarbin, A. J. G. PKa Determination of Graphene-like Materials: Validating Chemical Functionalization. *J Colloid Interface Sci* **2016**, *467*, 239–244. https://doi.org/10.1016/j.jcis.2016.01.013.

(156) Tang, H.; Zhang, S.; Huang, T.; Cui, F.; Xing, B. PH-Dependent Adsorption of Aromatic Compounds on Graphene Oxide: An Experimental, Molecular Dynamics Simulation and Density Functional Theory Investigation. *J Hazard Mater* **2020**, *395* (January), 122680. https://doi.org/10.1016/j.jhazmat.2020.122680.

(157) Pavinatto, A.; Mercante, L. A.; Facure, M. H. M.; Pena, R. B.; Sanfelice, R. C.; Mattoso, L. H. C.; Correa, D. S. Ultrasensitive Biosensor Based on Polyvinylpyrrolidone/Chitosan/Reduced Graphene Oxide Electrospun Nanofibers for 17α – Ethinylestradiol Electrochemical Detection. *Appl Surf Sci* **2018**, *458* (July), 431–437. https://doi.org/10.1016/j.apsusc.2018.07.035.

(158) Wang, F.; Gu, Z.; Lei, W.; Wang, W.; Xia, X.; Hao, Q. Graphene Quantum Dots as a Fluorescent Sensing Platform for Highly Efficient Detection of

Copper(II) Ions. *Sens Actuators B Chem* **2014**, *190*, 516–522. https://doi.org/10.1016/j.snb.2013.09.009.

(159) Kim, D.-Y.; Shinde, S.; Saratale, R.; Syed, A.; Ameen, F.; Ghodake, G. Spectrophotometric Determination of Fe(III) by Using Casein-Functionalized Gold Nanoparticles. *Microchimica Acta* **2017**, *184* (12), 4695–4704. https://doi.org/10.1007/s00604-017-2520-9.

(160) Pearson, R. G. Hard and Soft Acids and Bases. *J Am Chem Soc* **1963**, *85* (22), 3533–3539. https://doi.org/10.1021/ja00905a001.

(161) Hu, H.; He, H.; Zhang, J.; Hou, X.; Wu, P. Optical Sensing at the Nanobiointerface of Metal Ion-Optically-Active Nanocrystals. *Nanoscale*. Royal Society of Chemistry 2018, pp 5035–5046. https://doi.org/10.1039/c8nr00350e.

(162) Qian, Z. S.; Shan, X. Y.; Chai, L. J.; Chen, J. R.; Feng, H. A Fluorescent Nanosensor Based on Graphene Quantum Dots-Aptamer Probe and Graphene Oxide Platform for Detection of Lead (II) Ion. *Biosens Bioelectron* **2015**, *68,* 225–231. https://doi.org/10.1016/j.bios.2014.12.057.

(163) Wang, R.; Fan, H.; Jiang, W.; Ni, G.; Qu, S. Amino-Functionalized Graphene Quantum Dots Prepared Using High-Softening Point Asphalt and Their Application in Fe^{3+} Detection. *Appl Surf Sci* **2019**, *467–468* (June 2018), 446–455. https://doi.org/10.1016/j.apsusc.2018.10.104.

(164) Xu, F.; Shi, H.; He, X.; Wang, K.; He, D.; Yan, L.; Ye, X.; Tang, J.; Shangguan, J.; Luo, L. Masking Agent-Free and Channel-Switch-Mode Simultaneous Sensing of Fe^{3+} and Hg^{2+} Using Dual-Excitation Graphene Quantum Dots. *Analyst* **2015**, *140* (12), 3925–3928. https://doi.org/10.1039/c5an00468c.

(165) Ananthanarayanan, A.; Wang, X.; Routh, P.; Sana, B.; Lim, S.; Kim, D. H.; Lim, K. H.; Li, J.; Chen, P. Facile Synthesis of Graphene Quantum Dots from 3D Graphene and Their Application for Fe^{3+} Sensing. *Adv Funct Mater* **2014**, *24* (20), 3021–3026. https://doi.org/10.1002/adfm.201303441.

(166) Zhu, X.; Zhang, Z.; Xue, Z.; Huang, C.; Shan, Y.; Liu, C.; Qin, X.; Yang, W.; Chen, X.; Wang, T. Understanding the Selective Detection of Fe^{3+} Based on Graphene Quantum Dots as Fluorescent Probes: The Ksp of a Metal Hydroxide-Assisted Mechanism. *Anal Chem* **2017**, *89* (22), 12054–12058. https://doi.org/10.1021/acs.analchem.7b02499.

(167) Ju, J.; Chen, W. Synthesis of Highly Fluorescent Nitrogen-Doped Graphene Quantum Dots for Sensitive, Label-Free Detection of Fe (III) in Aqueous Media. *Biosens Bioelectron* **2014**, *58*, 219–225. https://doi.org/10.1016/j.bios.2014.02.061.

(168) Li, S.; Li, Y.; Cao, J.; Zhu, J.; Fan, L.; Li, X. Sulfur-Doped Graphene Quantum Dots as a Novel Fluorescent Probe for Highly Selective and Sensitive Detection of Fe^{3+}. *Anal Chem* **2014**, *86* (20), 10201–10207. https://doi.org/10.1021/ac503183y.

(169) Tam, T. Van; Trung, N. B.; Kim, H. R.; Chung, J. S.; Choi, W. M. One-Pot Synthesis of N-Doped Graphene Quantum Dots as a Fluorescent Sensing

Platform for Fe^{3+} Ions Detection. *Sens Actuators B Chem* **2014**, *202*, 568–573. https://doi.org/10.1016/j.snb.2014.05.045.

(170) Ding, S.; Gao, Y.; Ni, B.; Yang, X. Green Synthesis of Biomass-Derived Carbon Quantum Dots as Fluorescent Probe for Fe^{3+} Detection. *Inorg Chem Commun* **2021**, *130*, 108636. https://doi.org/10.1016/j.inoche.2021.108636.

(171) Dutta Chowdhury, A.; Doong, R. Highly Sensitive and Selective Detection of Nanomolar Ferric Ions Using Dopamine Functionalized Graphene Quantum Dots. *ACS Appl Mater Interfaces* **2016**, *8* (32), 21002–21010. https://doi.org/10.1021/acsami.6b06266.

(172) Zhang, Y.-L.; Wang, L.; Zhang, H.-C.; Liu, Y.; Wang, H.-Y.; Kang, Z.-H.; Lee, S.-T. Graphitic Carbon Quantum Dots as a Fluorescent Sensing Platform for Highly Efficient Detection of Fe^{3+} Ions. *RSC Adv* **2013**, *3* (11), 3733–3738. https://doi.org/10.1039/C3RA23410J.

(173) Gao, B.; Chen, D.; Gu, B.; Wang, T.; Wang, Z.; Xie, F.; Yang, Y.; Guo, Q.; Wang, G. Facile and Highly Effective Synthesis of Nitrogen-Doped Graphene Quantum Dots as a Fluorescent Sensing Probe for Cu^{2+} Detection. *Current Applied Physics* **2020**, *20* (4), 538–544. https://doi.org/10.1016/j.cap.2020.01.018.

(174) Sun, H.; Zhao, A.; Gao, N.; Li, K.; Ren, J.; Qu, X. Deciphering a Nanocarbon-Based Artificial Peroxidase: Chemical Identification of the Catalytically Active and Substrate-Binding Sites on Graphene Quantum Dots. *Angewandte Chemie International Edition* **2015**, *54* (24), 7176–7180. https://doi.org/10.1002/anie.201500626.

(175) Facure, M. H. M.; Matthews, K.; Wang, R.; Lord, R. W.; Correa, D. S.; Gogotsi, Y. Pillaring Effect of Nanodiamonds and Expanded Voltage Window of Ti$_3$C$_2$T$_x$ Supercapacitors in AlCl$_3$ Electrolyte. *Energy Storage Mater* **2023**, *61*, 102919. https://doi.org/10.1016/j.ensm.2023.102919.

(176) VahidMohammadi, A.; Rosen, J.; Gogotsi, Y. The World of Two-Dimensional Carbides and Nitrides (MXenes). *Science* **2021**, *372* (6547), eabf1581. https://doi.org/10.1126/science.abf1581.

(177) Zhu, Q.; Li, J.; Simon, P.; Xu, B. Two-Dimensional MXenes for Electrochemical Capacitor Applications: Progress, Challenges and Perspectives. *Energy Storage Mater* **2021**, *35*, 630–660. https://doi.org/10.1016/j.ensm.2020.11.035.

(178) Xie, X.; Zhao, M. Q.; Anasori, B.; Maleski, K.; Ren, C. E.; Li, J.; Byles, B. W.; Pomerantseva, E.; Wang, G.; Gogotsi, Y. Porous Heterostructured MXene/Carbon Nanotube Composite Paper with High Volumetric Capacity for Sodium-Based Energy Storage Devices. *Nano Energy* **2016**, *26*, 513–523. https://doi.org/10.1016/j.nanoen.2016.06.005.

(179) Fang, Y.; Yang, B.; He, D.; Li, H.; Zhu, K.; Wu, L.; Ye, K.; Cheng, K.; Yan, J.; Wang, G.; Cao, D. Porous and Free-Standing Ti$_3$C$_2$T$_x$-RGO Film with Ultrahigh Gravimetric Capacitance for Supercapacitors. *Chinese Chemical Letters* **2020**, *31* (4), 1004–1008. https://doi.org/10.1016/j.cclet.2019.08.043.

(180) Yan, J.; Ren, C. E.; Maleski, K.; Hatter, C. B.; Anasori, B.; Urbankowski, P.; Sarycheva, A.; Gogotsi, Y. Flexible MXene/Graphene Films for Ultrafast Supercapacitors with Outstanding Volumetric Capacitance. *Adv Funct Mater* **2017**, *27* (30), 1701264. https://doi.org/10.1002/adfm.201701264.

(181) Elemike, E. E.; Osafile, O. E.; Omugbe, E. New Perspectives 2Ds to 3Ds MXenes and Graphene Functionalized Systems as High Performance Energy Storage Materials. *J Energy Storage* **2021**, *42*. https://doi.org/10.1016/j.est.2021.102993.

(182) Liu, Y.; Yu, J.; Guo, D.; Li, Z.; Su, Y. $Ti_3C_2T_x$ MXene/Graphene Nanocomposites: Synthesis and Application in Electrochemical Energy Storage. *J Alloys Compd* **2020**, *815*. https://doi.org/10.1016/j.jallcom.2019.152403.

(183) Mochalin, V. N.; Shenderova, O.; Ho, D.; Gogotsi, Y. The Properties and Applications of Nanodiamonds. *Nat Nanotechnol* **2012**, *7* (1), 11–23. https://doi.org/10.1038/nnano.2011.209.

(184) Osswald, S.; Mochalin, V. N.; Havel, M.; Yushin, G.; Gogotsi, Y. Phonon Confinement Effects in the Raman Spectrum of Nanodiamond. *Phys Rev B* **2009**, *80* (7), 75419. https://doi.org/10.1103/PhysRevB.80.075419.

(185) Wang, G.; Zhang, L.; Zhang, J. A Review of Electrode Materials for Electrochemical Supercapacitors. *Chem Soc Rev* **2012**, *41* (2), 797–828. https://doi.org/10.1039/c1cs15060j.

(186) Lukatskaya, M. R.; Mashtalir, O.; Ren, C. E.; Dall'Agnese, Y.; Rozier, P.; Taberna, P. L.; Naguib, M.; Simon, P.; Barsoum, M. W.; Gogotsi, Y. Cation Intercalation and High Volumetric Capacitance of Two-Dimensional Titanium Carbide. *Science* **2013**, *341* (6153), 1502–1505. https://doi.org/10.1126/science.1241488.

(187) Xie, Y.; Dall'Agnese, Y.; Naguib, M.; Gogotsi, Y.; Barsoum, M. W.; Zhuang, H. L.; Kent, P. R. C. Prediction and Characterization of Mxene Nanosheet Anodes for Non-Lithium-Ion Batteries. *ACS Nano* **2014**, *8* (9), 9606–9615. https://doi.org/10.1021/nn503921j.

(188) Canepa, P.; Sai Gautam, G.; Hannah, D. C.; Malik, R.; Liu, M.; Gallagher, K. G.; Persson, K. A.; Ceder, G. Odyssey of Multivalent Cathode Materials: Open Questions and Future Challenges. *Chem Rev* **2017**, *117* (5), 4287–4341. https://doi.org/10.1021/acs.chemrev.6b00614.

(189) Li, S.; Shi, Q.; Li, Y.; Yang, J.; Chang, T.-H.; Jiang, J.; Chen, P.-Y. Intercalation of Metal Ions into $Ti_3C_2T_x$ MXene Electrodes for High-Areal-Capacitance Microsupercapacitors with Neutral Multivalent Electrolytes. *Adv Funct Mater* **2020**, *30* (40), 2003721. https://doi.org/10.1002/adfm.202003721.

(190) Gavriel, B.; Shpigel, N.; Malchik, F.; Bergman, G.; Turgeman, M.; Levi, M. D.; Aurbach, D. Enhanced Performance of $Ti_3C_2T_x$ (MXene) Electrodes in Concentrated ZnCl2 Solutions: A Combined Electrochemical and EQCM-D Study. *Energy Storage Mater* **2021**, *38*, 535–541. https://doi.org/10.1016/j.ensm.2021.03.027.

(191) VahidMohammadi, A.; Hadjikhani, A.; Shahbazmohamadi, S.; Beidaghi, M. Two-Dimensional Vanadium Carbide (MXene) as a High-Capacity Cathode Material for Rechargeable Aluminum Batteries. *ACS Nano* **2017**, *11* (11), 11135–11144. https://doi.org/10.1021/acsnano.7b05350.

(192) Wang, X.; Shen, X.; Gao, Y.; Wang, Z.; Yu, R.; Chen, L. Atomic-Scale Recognition of Surface Structure and Intercalation Mechanism of $Ti_3C_2T_x$. *J Am Chem Soc* **2015**, *137* (7), 2715–2721. https://doi.org/10.1021/ja512820k.

(193) Lipatov, A.; Alhabeb, M.; Lukatskaya, M. R.; Boson, A.; Gogotsi, Y.; Sinitskii, A. Effect of Synthesis on Quality, Electronic Properties and Environmental Stability of Individual Monolayer Ti_3C_2 MXene Flakes. *Adv Electron Mater* **2016**, *2* (12), 1600255. https://doi.org/10.1002/aelm.201600255.

(194) Xiao, J.; Li, J. L.; Liu, P.; Yang, G. W. A New Phase Transformation Path from Nanodiamond to New-Diamond via an Intermediate Carbon Onion. *Nanoscale* **2014**, *6* (24), 15098–15106. https://doi.org/10.1039/c4nr05246c.

(195) Petit, T.; Arnault, J. C.; Girard, H. A.; Sennour, M.; Bergonzo, P. Early Stages of Surface Graphitization on Nanodiamond Probed by X-Ray Photoelectron Spectroscopy. *Phys Rev B Condens Matter Mater Phys* **2011**, *84* (23), 1–5. https://doi.org/10.1103/PhysRevB.84.233407.

(196) Shekhirev, M.; Shuck, C. E.; Sarycheva, A.; Gogotsi, Y. Characterization of MXenes at Every Step, from Their Precursors to Single Flakes and Assembled Films. *Prog Mater Sci* **2021**, *120*. https://doi.org/10.1016/j.pmatsci.2020.100757.

(197) Kayali, E.; Vahidmohammadi, A.; Orangi, J.; Beidaghi, M. Controlling the Dimensions of 2D MXenes for Ultrahigh-Rate Pseudocapacitive Energy Storage. *ACS Appl Mater Interfaces* **2018**, *10* (31), 25949–25954. https://doi.org/10.1021/acsami.8b07397.

(198) Echols, I. J.; Yun, J.; Cao, H.; Thakur, R. M.; Sarmah, A.; Tan, Z.; Littleton, R.; Radovic, M.; Green, M. J.; Lutkenhaus, J. L. Conformal Layer-by-Layer Assembly of $Ti_3C_2T_z$ MXene-Only Thin Films for Optoelectronics and Energy Storage. *Chemistry of Materials* **2022**, *34* (11), 4884–4895. https://doi.org/10.1021/acs.chemmater.1c04394.

(199) Maleski, K.; Ren, C. E.; Zhao, M.-Q.; Anasori, B.; Gogotsi, Y. Size-Dependent Physical and Electrochemical Properties of Two-Dimensional MXene Flakes. *ACS Appl Mater Interfaces* **2018**, *10* (29), 24491–24498. https://doi.org/10.1021/acsami.8b04662.

(200) Shekhirev, M.; Ogawa, Y.; Shuck, C. E.; Anayee, M.; Torita, T.; Gogotsi, Y. Delamination of $Ti_3C_2T_x$ Nanosheets with NaCl and KCl for Improved Environmental Stability of MXene Films. *ACS Appl Nano Mater* **2022**. https://doi.org/10.1021/acsanm.2c03701.

(201) Gogotsi, Y.; Simon, P. True Performance Metrics in Electrochemical Energy Storage. *Science* **2011**, *334* (6058), 917–918. https://doi.org/10.1126/science.1213003.

Appendix A

Supporting Information of Chapter I

2^3 Factorial Design using C_{GO}, T, and pH as parameters:

$$QY = -5.70111 + 22.74444\, C_{GO} - 5.77778\, C_{GO}^2 - 0.61333\, pH - 0.07967\, T +$$
$$0.00733\, pH\, T \qquad\qquad\qquad\qquad\qquad\qquad\qquad\qquad\qquad \text{(Eq. A1)}$$

2^2 Factorial Design using T and pH as parameters:

$$QY = 8.21250 - 0.16240\, T - 2.78226\, T^2 - 0.64826\, pH + 0.45505\, pH\, T \quad \text{(Eq. A2)}$$

TABLE A1: Comparison of quantum yield (QY) of GQDs obtained by hydrothermal synthesis using GO as precursor.

Precursor pretreatment	Cutting reagent	QY (%)	Ref.
Thermal deoxidization and acidic oxidation	None	6.9	A1
Thermal reduction and acidic oxidation	None	7.5	A2
None	KO_2	8.9	A3
None	H_2O_2	4.6	A4
None	H_2O_2	6.99	A5
None	H_2O_2	5.3	A6
None	None	8.9	This Work

TABLE A2: Comparison of quantum yield (QY) of modified GQDs.

Synthesis Method	GQDs modification	QY (%)	Ref.
Hydrothermal	S-doping	51	A7
Hydrothermal	S-doping	53	A8
Hydrothermal	N-doping	49.8	A9
Solvothermal	N-doping	74	A10
Hydrothermal	B-doping	16.8	A11
Hydrothermal	Cl-doping	6.2	A12
Hydrothermal	S, N co-doping	71	A13
Solvothermal	B, N co-doping	36.5	A14

| Microwave treatment | F, S, N co-doping | 70 | A15 |
| Hydrothermal | Surface passivation by PEG | 28 | A16 |
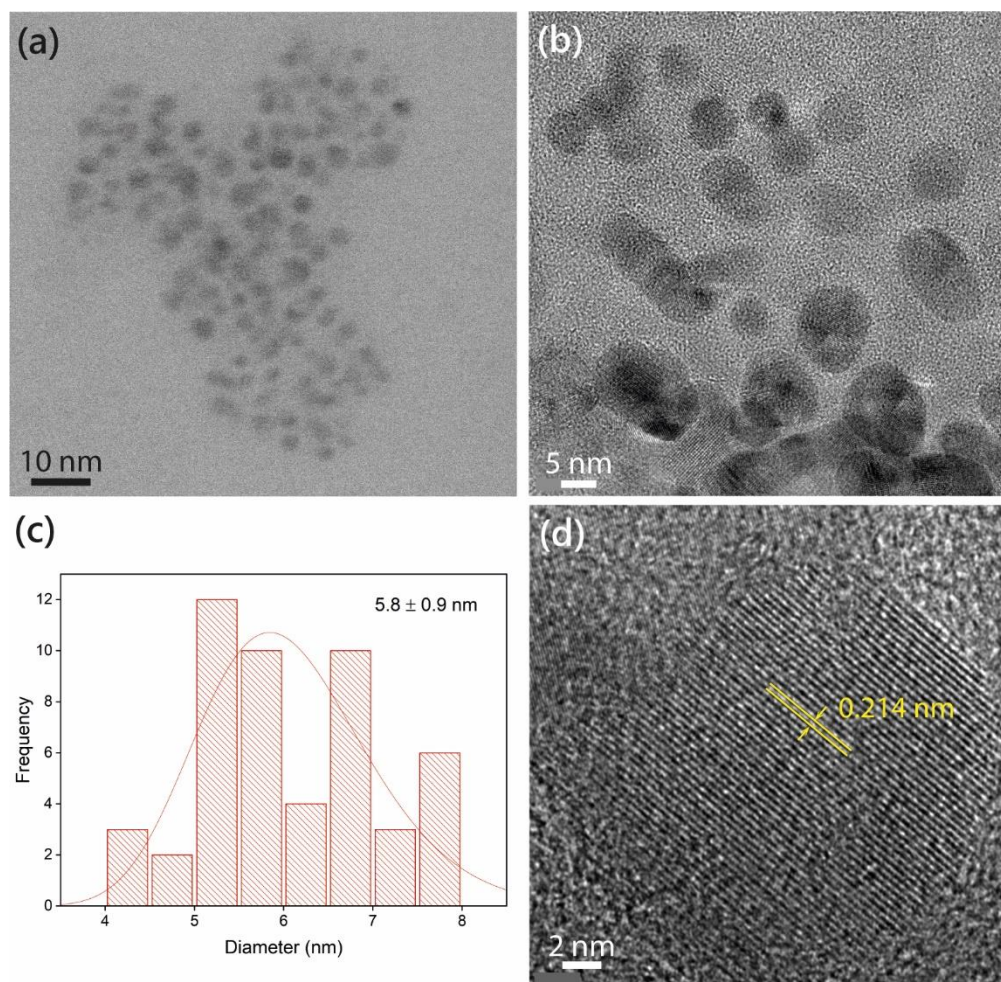
FIGURE A1: (a-b) TEM images, (c) histogram of the size distribution of GQDs, and (d) high-resolution TEM image of an individual GQD with the in-plane lattice spacing.

TABLE A3: XPS analysis of GQDs-1, GQDs-2, and GQDs-3.

Peak	GQDs-1		GQDs-2		GQDs-3	
	Binding Energy (eV)	Contribution (%)	Binding Energy (eV)	Contribution (%)	Binding Energy (eV)	Contribution (%)
C=C/C—C	283.8	47.57	283.8	47.77	284.0	48.56
C—O	284.8	29.11	284.8	33.59	284.9	29.02
C=O	287.3	23.32	287.2	18.64	287.6	22.41
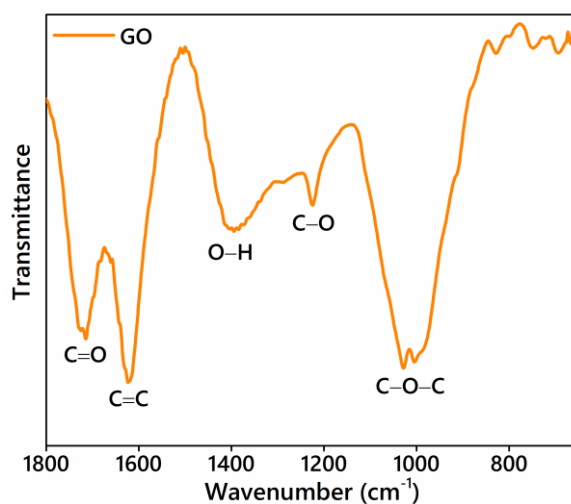
FIGURE A2: FTIR spectrum of GO.
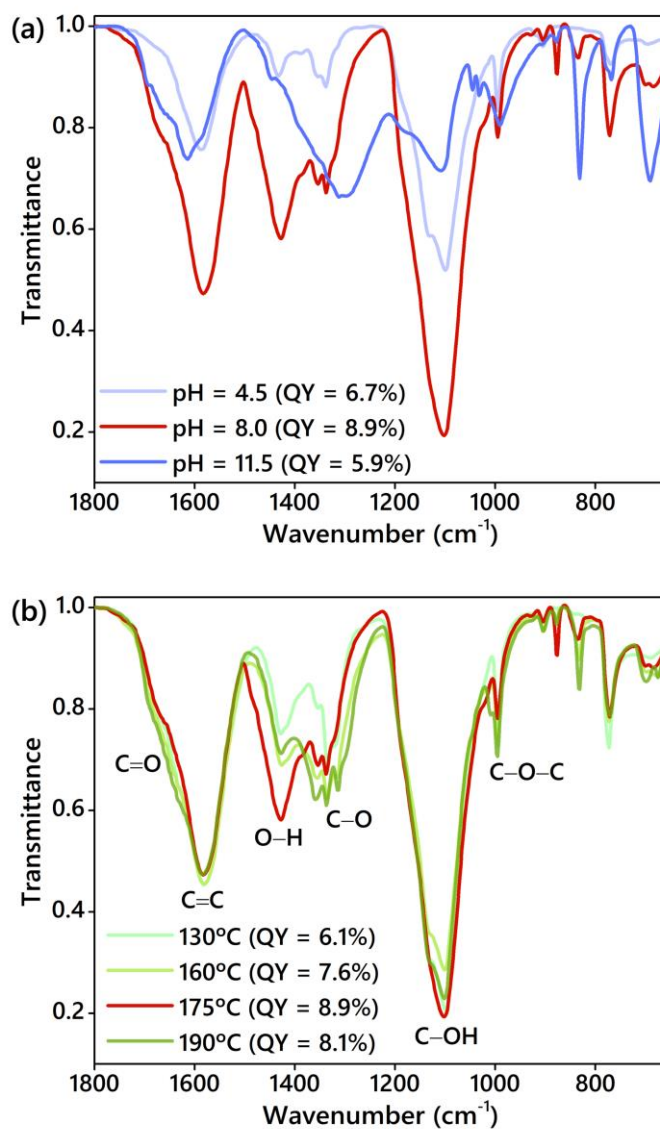
FIGURE A3: FTIR spectra of GQDs synthesized (a) varying the pH at a fixed temperature (175 °C) and (b) varying the T of the hydrothermal syntheses at pH = 8.
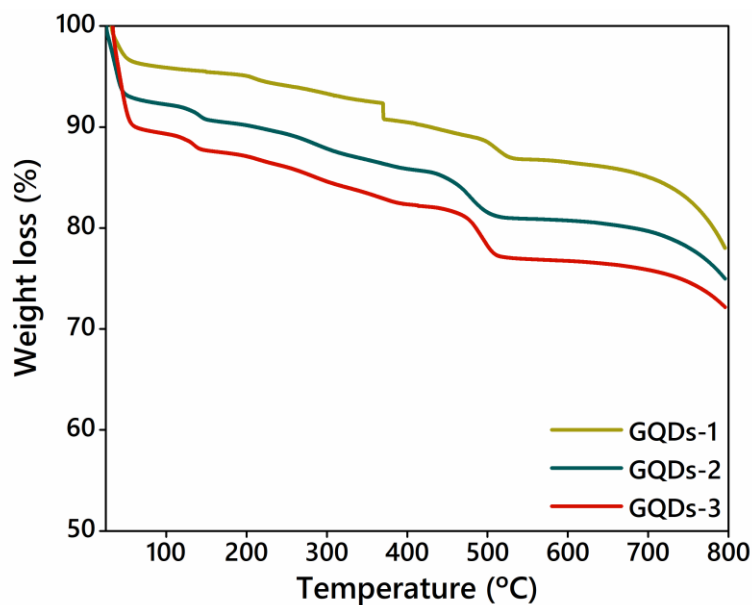
FIGURE A4: Thermogravimetric Analysis (TGA) curves of GQDs-1, GQDs-2, and GQDs-3.
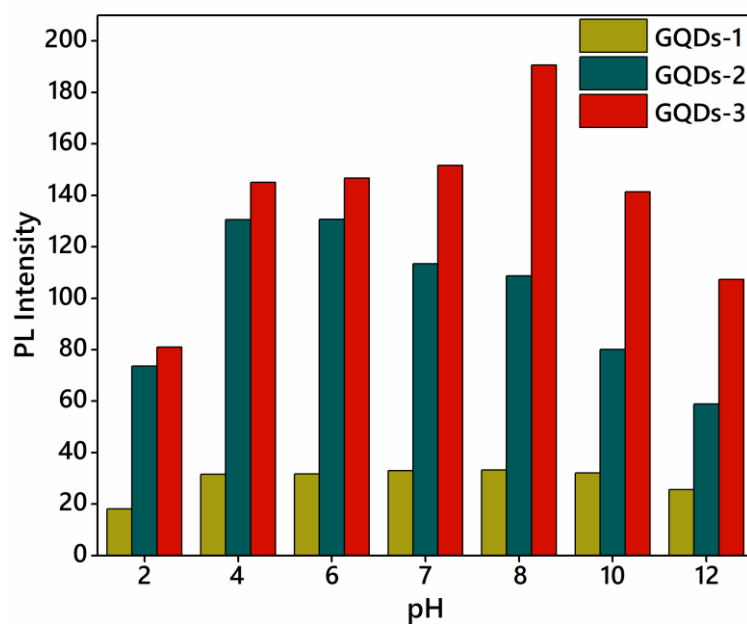
FIGURE A5: PL intensity emission of GQDs-1, GQDs-2, and GQDs-3 at different pH values.

References

(A1)   Pan, D.; Zhang, J.; Li, Z.; Wu, M. Hydrothermal Route for Cutting Graphene Sheets into Blue-Luminescent Graphene Quantum Dots. Advanced Materials 2010, 22 (6), 734–738. https://doi.org/10.1002/adma.200902825.

(A2)   Pan, D.; Guo, L.; Zhang, J.; Xi, C.; Xue, Q.; Huang, H.; Li, J.; Zhang, Z.; Yu, W.; Chen, Z.; Li, Z.; Wu, M. Cutting sp^2 Clusters in Graphene Sheets into Colloidal Graphene Quantum Dots with Strong Green Fluorescence. J Mater Chem 2012, 22 (8), 3314–3318. https://doi.org/10.1039/c2jm16005f.

(A3)   Zhao, Y.; Wu, X.; Sun, S.; Ma, L.; Zhang, L.; Lin, H. A Facile and High-Efficient Approach to Yellow Emissive Graphene Quantum Dots from Graphene Oxide. Carbon N Y 2017, 124, 342–347. https://doi.org/10.1016/j.carbon.2017.09.011.

(A4)   Halder, A.; Godoy-Gallardo, M.; Ashley, J.; Feng, X.; Zhou, T.; Hosta-Rigau, L.; Sun, Y. One-Pot Green Synthesis of Biocompatible Graphene Quantum Dots and Their Cell Uptake Studies. ACS Appl Bio Mater 2018, 1 (2), 452–461. https://doi.org/10.1021/acsabm.8b00170.

(A5)   Zhu, X.; Xiao, X.; Zuo, X.; Liang, Y.; Nan, J. Hydrothermal Preparation of Photoluminescent Graphene Quantum Dots Characterized Excitation-Independent Emission and Its Application as a Bioimaging Reagent. Particle & Particle Systems Characterization 2014, 31 (7), 801–809. https://doi.org/10.1002/ppsc.201300375.

(A6)   Tian, R.; Zhong, S.; Wu, J.; Jiang, W.; Wang, T. Facile Hydrothermal Method to Prepare Graphene Quantum Dots from Graphene Oxide with Different Photoluminescences. RSC Adv 2016, 6 (46), 40422–40426. https://doi.org/10.1039/C6RA00780E.

(A7)   Kharangarh, P. R.; Umapathy, S.; Singh, G. Thermal Effect of Sulfur Doping for Luminescent Graphene Quantum Dots. ECS Journal of Solid State Science and Technology 2018, 7 (3), M29–M34. https://doi.org/10.1149/2.0041803jss.

(A8)   Kharangarh, P. R.; Umapathy, S.; Singh, G. Investigation of Sulfur Related Defects in Graphene Quantum Dots for Tuning Photoluminescence and High Quantum Yield. Appl Surf Sci 2018, 449, 363–370. https://doi.org/10.1016/j.apsusc.2018.01.026.

(A9)   Kharangarh, P. R.; Umapathy, S.; Singh, G. Effect of Defects on Quantum Yield in Blue Emitting Photoluminescent Nitrogen Doped Graphene Quantum Dots. J Appl Phys 2017, 122 (14), 145107. https://doi.org/10.1063/1.4991693.

(A10)   Sun, J.; Yang, S.; Wang, Z.; Shen, H.; Xu, T.; Sun, L.; Li, H.; Chen, W.; Jiang, X.; Ding, G.; Kang, Z.; Xie, X.; Jiang, M. Ultra-High Quantum Yield of Graphene

Quantum Dots: Aromatic-Nitrogen Doping and Photoluminescence Mechanism. Particle and Particle Systems Characterization 2015, 32 (4), 434–440. https://doi.org/10.1002/ppsc.201400189.

(A11) Ge, S.; He, J.; Ma, C.; Liu, J.; Xi, F.; Dong, X. One-Step Synthesis of Boron-Doped Graphene Quantum Dots for Fluorescent Sensors and Biosensor. Talanta 2019, 199, 581–589. https://doi.org/10.1016/j.talanta.2019.02.098.

(A12) Wang, X.-F.; Wang, G.-G.; Li, J.-B.; Liu, Z.; Chen, Y.-X.; Liu, L.-F.; Han, J.-C. Direct White Emissive Cl-Doped Graphene Quantum Dots-Based Flexible Film as a Single Luminophore for Remote Tunable UV-WLEDs. Chemical Engineering Journal 2019, 361, 773–782. https://doi.org/10.1016/j.cej.2018.12.131.

(A13) Qu, D.; Zheng, M.; Du, P.; Zhou, Y.; Zhang, L.; Li, D.; Tan, H.; Zhao, Z.; Xie, Z.; Sun, Z. Highly Luminescent S, N Co-Doped Graphene Quantum Dots with Broad Visible Absorption Bands for Visible Light Photocatalysts. Nanoscale 2013, 5 (24), 12272–12277. https://doi.org/10.1039/c3nr04402e.

(14) Li, R. S.; Yuan, B.; Liu, J. H.; Liu, M. L.; Gao, P. F.; Li, Y. F.; Li, M.; Huang, C. Z. Boron and Nitrogen Co-Doped Single-Layered Graphene Quantum Dots: A High-Affinity Platform for Visualizing the Dynamic Invasion of HIV DNA into Living Cells through Fluorescence Resonance Energy Transfer. J Mater Chem B 2017, 5 (44), 8719–8724. https://doi.org/10.1039/C7TB02356A.

(A15) Kundu, S.; Yadav, R. M.; Narayanan, T. N.; Shelke, M. V; Vajtai, R.; Ajayan, P. M.; Pillai, V. K. Synthesis of N, F and S Co-Doped Graphene Quantum Dots. Nanoscale 2015, 7 (27), 11515–11519. https://doi.org/10.1039/C5NR02427G.

(A16) Shen, J.; Zhu, Y.; Yang, X.; Zong, J.; Zhang, J.; Li, C. One-Pot Hydrothermal Synthesis of Graphene Quantum Dots Surface-Passivated by Polyethylene Glycol and Their Photoelectric Conversion under near-Infrared Light. New Journal of Chemistry 2012, 36 (1), 97–101. https://doi.org/10.1039/c1nj20658c.

Appendix B

Supporting Information of Chapter II
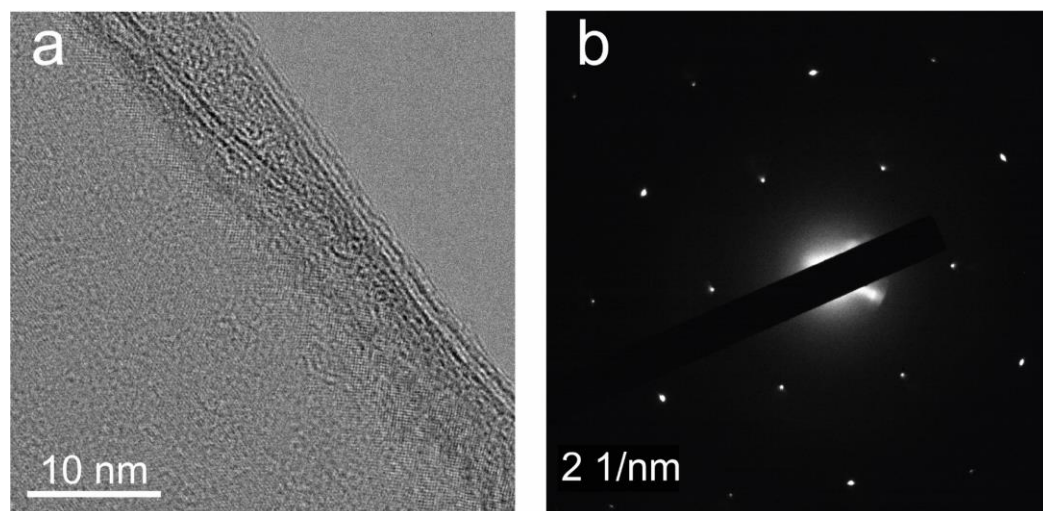
FIGURE B1. (a) High-resolution TEM image and (b) Selected Area Electron Diffraction (SAED) pattern of $Ti_3C_2T_x$.
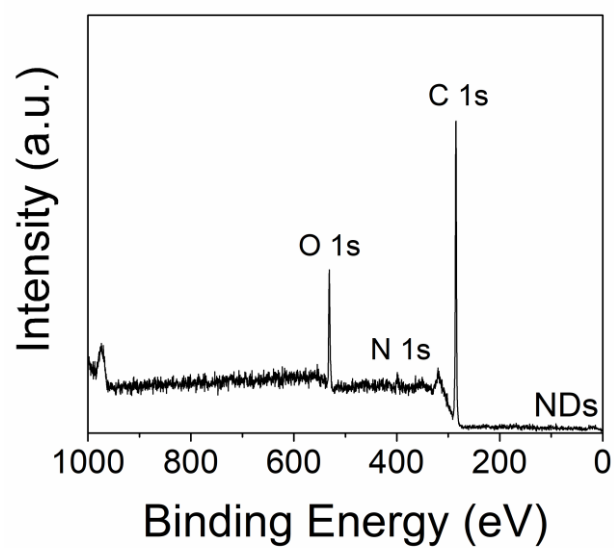
FIGURE B2. XPS survey spectra of the NDs powder.
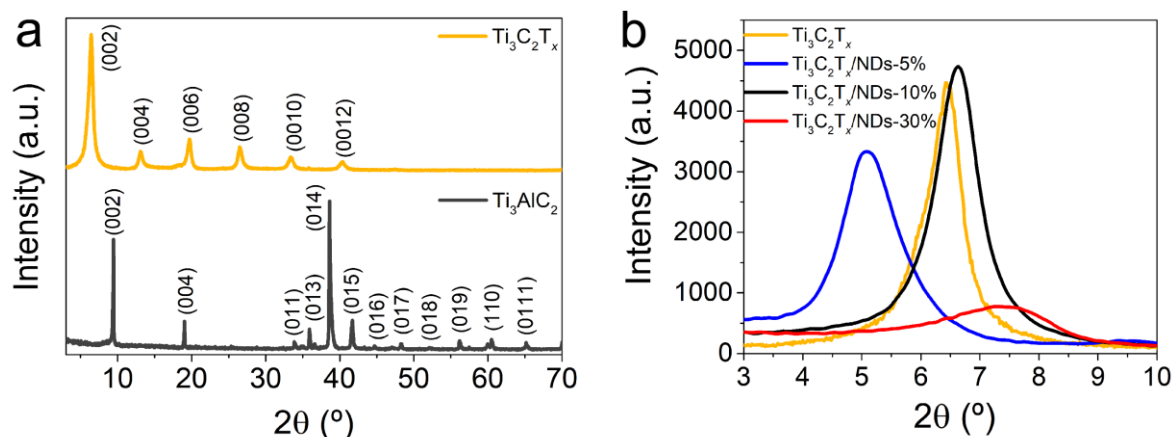
FIGURE B3. (a) XRD patterns for Ti₃AlC₂ MAX phase and Ti₃C₂Tₓ film. (e) *002* peak of the XRD patterns of Ti₃C₂Tₓ and Ti₃C₂Tₓ/NDs films.
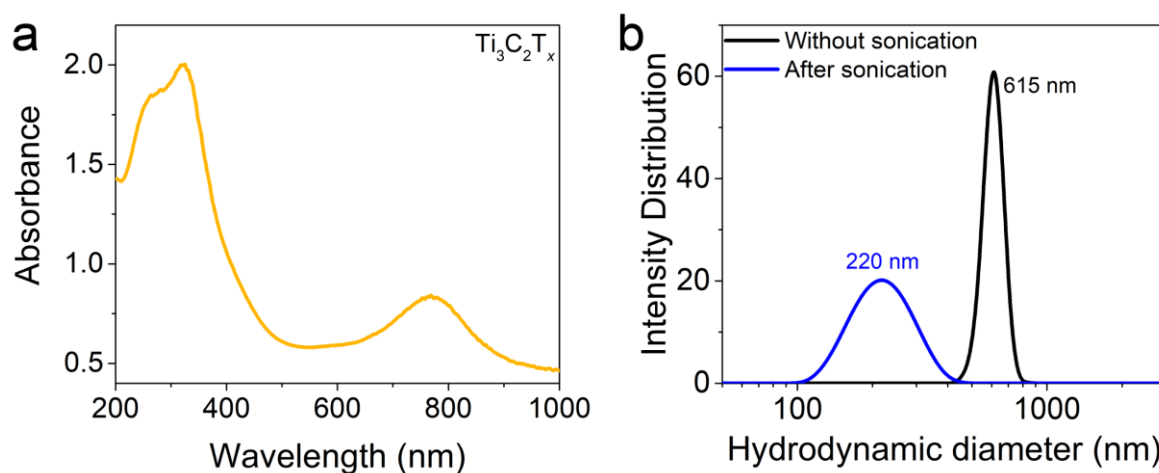
FIGURE B4. (a) UV-vis spectrum of Ti₃C₂Tₓ dispersion. (b) Dynamic Light Scattering (DLS) measurements showing the average flake size of the Ti₃C₂Tₓ before and after probe sonication for 10 min.
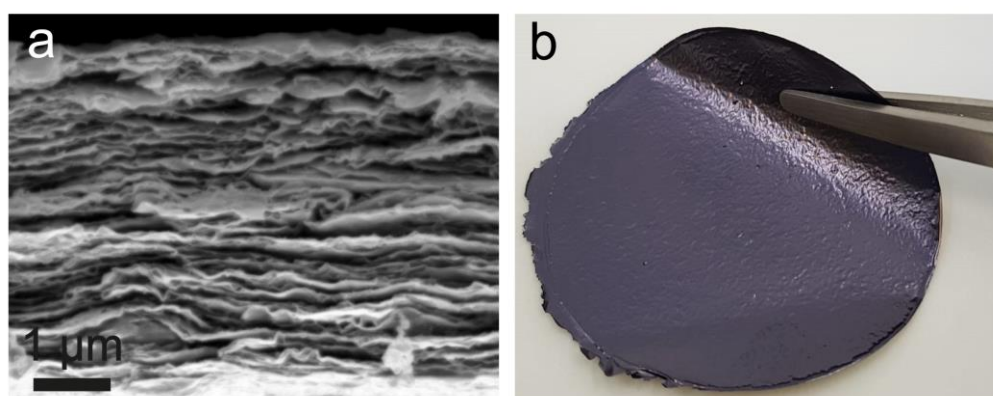
FIGURE B5. (a) Cross-sectional image of the Ti₃C₂Tₓ/NDs-10% film and (b) digital image of the free-standing flexible vacuum filtrated Ti₃C₂Tₓ/NDs-10% film. The film has a diameter of 4 cm.
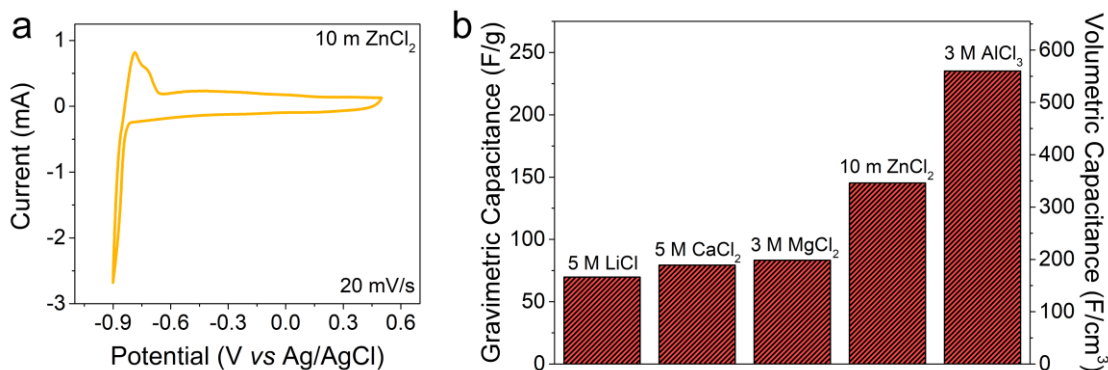
FIGURE B6. (a) Cyclic voltammogram for $Ti_3C_2T_x$/NDs-10% in 10 m $ZnCl_2$ showing the metal's plating at negative potentials. The CV was collected at 20 mV/s. (b) Comparison of the electrochemical performance (at 2 mV/s) of $Ti_3C_2T_x$/NDs-10% as a supercapacitor electrode in 5 M LiCl, 5 M $CaCl_2$, 3 M $MgCl_2$, 10 m $ZnCl_2$, and 3 M $AlCl_3$.
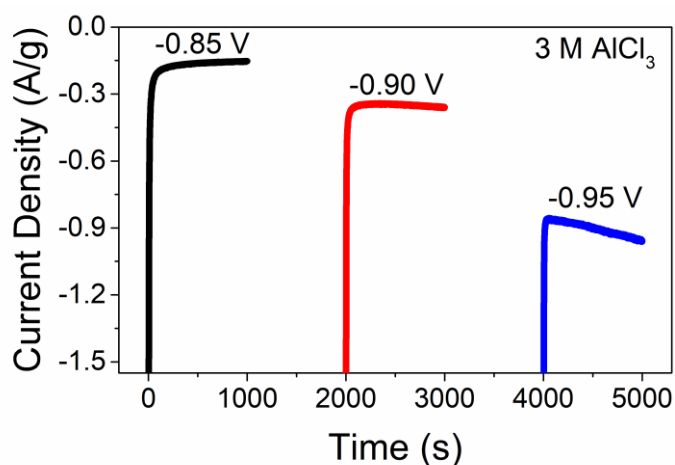
FIGURE B7. Chronoamperometry data collected at different potentials in 3 M $AlCl_3$, showing that -0.9 V is the maximum negative potential of the safe voltage window. The reference electrode used was Ag/AgCl.
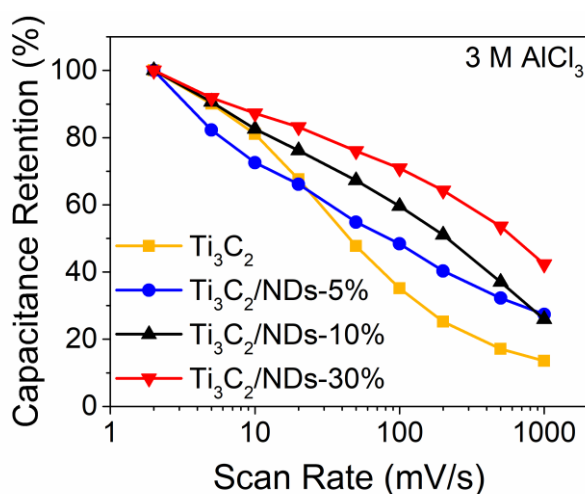
FIGURE B8. Capacitance retention at different scan rates for $Ti_3C_2T_x$ and $Ti_3C_2T_x$/NDs hybrid electrodes in 3 M $AlCl_3$.
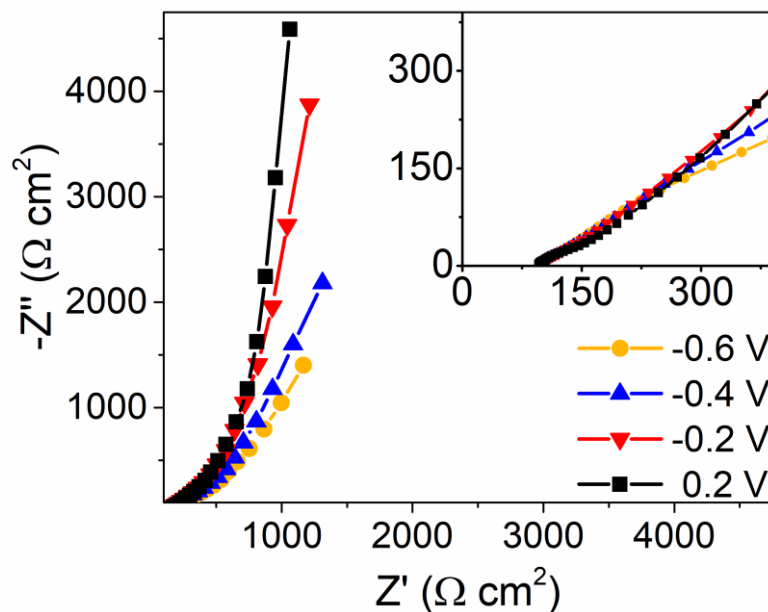
FIGURE B9. Electrochemical impedance spectra collected at different potentials for $Ti_3C_2T_x$/NDs-10% in 3 M $AlCl_3$. The inset shows the high-frequency range. The constant charge transfer resistance (R_{CT}) at all potentials indicates the presence of interfacial impedance at the current collector and the electrode interface.
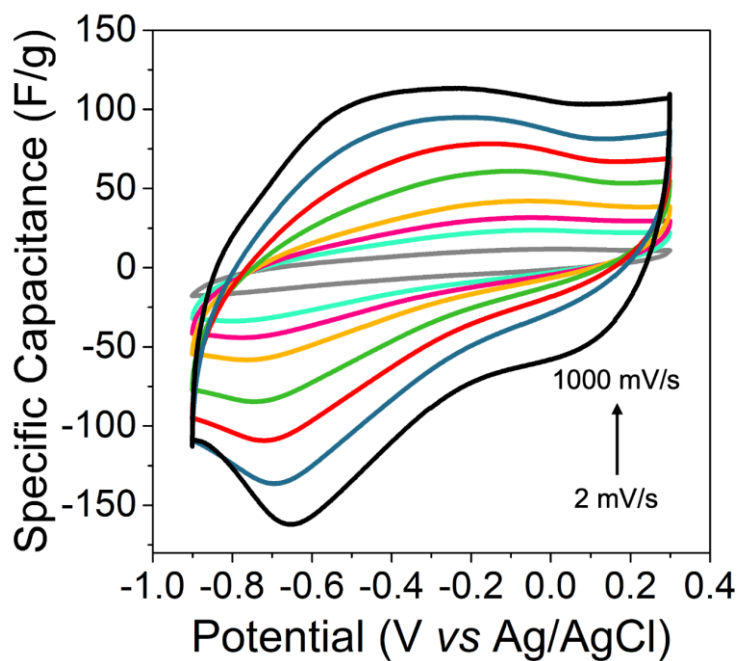
FIGURE B10. CVs for the 8.3 mg/cm^2 $Ti_3C_2T_x$/NDs-10% film in 3 M $AlCl_3$ at different scan rates (2, 5, 10, 20, 50, 100, 200, and 1000 mV/s).

Appendix C

Publication rights permission

Figure C1: Permission to use the article "Rational hydrothermal synthesis of graphene quantum dots with optimized luminescent properties for sensing applications".

Figure C2: Permission to use the article "Pillaring effect of nanodiamonds and expanded voltage window of $Ti_3C_2T_x$ supercapacitors in $AlCl_3$ electrolyte".

Thank you for your order.

This Agreement between Mr. Murilo Henrique Moreira Facure ("You") and John Wiley and Sons ("John Wiley and Sons") consists of your license details and the terms and conditions provided by John Wiley and Sons and Copyright Clearance Center.

Your confirmation email will contain your order number for future reference.

License Number	5627630669232		🖶 Printable Details
License date	Sep 14, 2023		

✅ Licensed Content   **📋 Order Details**

Licensed Content Publisher	John Wiley and Sons	**Type of use**	Dissertation/Thesis
Licensed Content Publication	Advanced Materials	**Requestor type**	University/Academic
Licensed Content Title	Hydrothermal Route for Cutting Graphene Sheets into Blue-Luminescent Graphene Quantum Dots	**Format**	Print and electronic
		Portion	Figure/table
		Number of figures/tables	1
Licensed Content Author	Minghong Wu, Zhen Li, Jingchun Zhang, et al	**Will you be translating?**	No
Licensed Content Date	Feb 4, 2010		
Licensed Content Volume	22		
Licensed Content Issue	6		
Licensed Content Pages	5		

Figure C3: Permission to use figures from the article "Hydrothermal Route for Cutting Graphene Sheets into Blue-Luminescent Graphene Quantum Dots".

MXenes: Two-Dimensional Building Blocks for Future Materials and Devices

ACS Publications
Most Trusted. Most Cited. Most Read.

Author: Yury Gogotsi, Qing Huang
Publication: ACS Nano
Publisher: American Chemical Society
Date: Apr 1, 2021

Copyright © 2021, American Chemical Society

PERMISSION/LICENSE IS GRANTED FOR YOUR ORDER AT NO CHARGE

This type of permission/license, instead of the standard Terms and Conditions, is sent to you because no fee is being charged for your order. Please note the following:

- Permission is granted for your request in both print and electronic formats, and translations.
- If figures and/or tables were requested, they may be adapted or used in part.
- Please print this page for your records and send a copy of it to your publisher/graduate school.
- Appropriate credit for the requested material should be given as follows: "Reprinted (adapted) with permission from {COMPLETE REFERENCE CITATION}. Copyright {YEAR} American Chemical Society." Insert appropriate information in place of the capitalized words.
- One-time permission is granted only for the use specified in your RightsLink request. No additional uses are granted (such as derivative works or other editions). For any uses, please submit a new request.

If credit is given to another source for the material you requested from RightsLink, permission must be obtained from that source.

BACK   **CLOSE WINDOW**

Figure C4: Permission to use figures from the article "MXenes: Two-Dimensional Building Blocks for Future Materials and Devices".

Two-Dimensional Transition Metal Carbides

Author: Michael Naguib, Olha Mashtalir, Joshua Carle, et al

Publication: ACS Nano

Publisher: American Chemical Society

Date: Feb 1, 2012

Copyright © 2012, American Chemical Society

Figure C5: Permission to use figures from the article "Two-Dimensional Transition Metal Carbides".